Monitoring Shallow Vadose Zone Moisture Dynamics using Electrical Resistivity Tomography and Electromagnetic Induction

by

Cameron William Toy

A thesis
presented to the University of Waterloo
in fulfillment of the
thesis requirement for the degree of
Master of Science
in
Earth Sciences

Waterloo, Ontario, Canada, 2015

AUTHOR'S DECLARATION

I hereby declare that I am the sole author of this thesis. This is a true copy of the thesis, including any required final revisions, as accepted by my examiners.

I understand that my thesis may be made electronically available to the public.

Abstract

This hydrogeophysical study examines the capacity of the surface electrical resistivity tomography (ERT) and electromagnetic induction (EMI) methods to monitor soil moisture dynamics in the shallow vadose zone over the range of conditions encountered during multiple annual cycles.

High-resolution ERT and EMI surveys were performed to monitor changes in shallow moisture conditions at a vineyard located in Vineland, Ontario, Canada. Twenty-five metre profile lines were established at five monitoring sites with soil textures ranging from silty clay to silt loam. ERT surveys were performed at each of these five sites whereas EMI data were acquired at only three of these monitoring sites due to the presence of wire trellises at the other sites. Geophysical surveys were performed approximately every two to four weeks. The geophysical data set is supplemented by precipitation and temperature observations, as well as historic soil temperature readings to 3 meters depth, taken at a nearby weather station and gravimetric water content measurements obtained at each monitoring site. The combination of the multi-year monitoring period, dense temporal sampling interval and concurrent use of both the ERT and EMI methods, as well as the supplemental weather and gravimetric information make this a very unique hydrogeophysical data set.

A wide range of soil moisture conditions were encountered at the monitoring sites including wet spring and fall, dry summer, and frozen winter periods, as well as contrasting conditions between the two annual cycles (e.g., relatively wetter versus drier summer conditions). Temporal variations observed in both the ERT and EMI data qualitatively agrees well with shallow soil moisture conditions (i.e., the upper most 0.50 meter) inferred from the gravimetric measurements and weather data. In addition, ERT results for the subsurface below 1 meter appear to follow the historical pattern of soil temperature. In addition, there is very good qualitative agreement between the ERT and EMI data set in terms of their temporal and spatial variability. However, a quantitative analysis of the relationships between gravimetric data, soil temperature and geophysical data reveals that additional work is needed to understand the nature of these relationships. Further, a basic quantitative comparison of the ERT and EMI results reveals divergences that require more investigation.

Acknowledgements

First of all, I would like to thank my supervisor Dr. Anthony Endres for providing me with the opportunity to work on this project. Tony's exceptional hydrogeophysical know-how, excitement for the Vineland study, and dedication to staying well-caffeinated were all instrumental components to this smoothly-running study.

I also must give a special thanks to Dr. Colby Steelman for showing me the ropes when I began working in Tony’s research group as an undergraduate student and for his contributions to the early-goings of the Vineland study.

I would like to thank my committee members Drs. Peeter Pehme and Jan van der Kruk for taking the time to attend the committee meeting and the defence and for the insightful conversations that have been had along the way. I would also like to thank Dr. David Rudolph who joined my committee for the defence.

Given the extensive field work required for this investigation, I am extremely appreciative of everyone who helped lighten my load by spending a long day with me out in the vineyard. I must specifically single out Alicia Beynon whose hard work and always-pleasant attitude ensured that the work got done and that all the trips in the van and days in the vineyard were enjoyable. Other helpful hands were those of Phil Van-Lane, John Lee, and John Mosquera.

I would like to thank John Jansen and Brian Piott from the Rittenhouse Grape Research Station who generously accommodated us by working around our schedule.

I would like to thank all of the individuals who have passed through the geophysics lab and left behind solid advice and good cheer. Most notably I would like to thank Daniel Altdorff, Melissa Bunn, Cameron McNaughton, and Achim Mester.

I would like to express my gratitude to my family for their dependable encouragement. I would also like to extend my gratitude to Laura Bell and all my friends who were present for any of the countless good times during this period of my life. Finally, I would like to thank the City of Kitchener for being a fitting home for the past three-or-so years.

Cheers to you all.

Dedication

This thesis is dedicated to my grandparents:

Audrey Toy
&
Russell and Jacqueline Dorland

Table of Contents

List of Figures

List of Tables

Chapter 1 INTRODUCTION

The ability to monitor soil moisture content in the vadose zone impacts the many disciplines that involve near-surface hydrological processes (Vereecken et al., 2008). Water resource managers require knowledge about this parameter for its implications on watershed investigations (Robinson et al., 2008), estimating surface runoff (Köhne et al., 2011), quantifying groundwater recharge (Healy, 2010) and formulating ecohydrological management strategies (Newman et al., 2006). Since soil moisture is a constraining variable on evapotranspiration and storage estimates, a reliable measurement of this parameter is important for weather forecasting, as well as the calibration and validation of climate change models (Seneviratne et al., 2010). Modelers of fluid transport through the vadose zone also require this important variable for predicting the spread of contaminants through a subsurface (Appelo and Postma, 2010). Soil moisture measurements can be used to derive soil texture and morphology (Wilson et al., 2003) and can be used in the prediction of other important hydrogeological variables such as unsaturated hydraulic conductivity (e.g., van Genuchten, 1980). Practitioners tackling the challenge of agricultural sustainability through precision farming require moisture measurements in the unsaturated zone at the highest resolution possible (Mondal and Tewari 2007).

1.1 Use of Geoelectrical Methods in Hydrogeophysics

Hydrogeophysics is a multi-disciplinary field that connects geophysical techniques with important hydrogeological applications such as determining subsurface hydrogeological properties, defining subsurface features that may influence the movement of water or monitoring important groundwater processes (Binley et al., 2010). It is widely believed that the integration of such techniques to hydrogeological investigations will greatly improve the understanding of dynamic hydrological processes (Robinson et al., 2008).

Traditional techniques for measuring soil moisture (i.e., gravimetric analysis on collected soil samples, neutron probing and time-domain reflectometry) are inadequate to deal with the needs of today’s field and watershed scale hydrogeological investigations. These methods provide only point-source information about the subsurface and can be costly or unfeasible to scale up to the degree of spatial coverage required for a more detailed analysis of soil moisture dynamics. Further, traditional methods are generally invasive and can result in the inability to perform the repeated measurements necessary for the temporal monitoring of dynamic processes. On the other hand, due to their larger sampling volumes, mobility and non-invasive nature, modern geophysical methods are ideally suited to provide the information necessary to analyze and monitor hydrogeological processes.

Many geophysical techniques have been used for hydrological applications. The task and the setting determine the most suitable techniques for a given application. Delineating subsurface features that may be important to hydrological processes can be accomplished by techniques that measure one of many physical properties in the subsurface (e.g., seismic methods that measure elastic moduli or gravity methods which respond to density contrasts). For higher-order tasks such as determining the location, movement or condition of water, geophysical techniques that measure physical properties with stronger associations to hydrological properties are advantageous (Binley et al., 2010). Geoelectrical techniques have been widely used in hydrogeophysical applications since the presence of water strongly affects electrical conductivity. Electromagnetic induction (EMI) and low-frequency resistivity methods are two types of geoelectrical techniques**.** Since the initial use of resistivity and EMI as hydrogeophysical techniques in the early 1990's, much work has been done on the use of these methods for monitoring the distribution, storage and movement of subsurface moisture.

Electrical resistivity tomography (ERT) is a low-frequency resistivity method that measures the electrical resistivity of the subsurface by making measurements at the surface. Early studies such as Kean et al. (1987) and Goyal et al. (1996) began looking at the capabilities and limitations of surface resistivity methods for assessing soil moisture conditions. Goyal et al. (1996) concluded that the surface resistivity method had a strong potential as a tool for delineating wetting fronts, providing data that may have been missed with a conventional point-source approach in a heterogeneous environment. More recent studies have applied the ERT technique to increasingly heterogeneous environments (Pellicer et al., 2012) for quantifying moisture content at the field scale (Schwartz et al. 2008), in precision agriculture (Kelly et al., 2011) and for moisture-climate interactions (Seneviratne et al., 2010). Systems such as the MuCEP (MultiContinous Electrical Profiling) device (Cousin et al., 2009; Besson et al., 2010) have enabled the resistivity method to acquire vadose zone data in a continuous manner at the field scale.

Kachanoski et al. (1990) and Sheets and Hendrickx (1995) are early studies that investigated the use of EMI for vadose zone moisture analysis. Kachanoski et al. were looking for a quick method for determining relative differences in moisture content at various field locations or on different days. The goals of Sheet and Hendrickx were similar, but with the added objective of quantifying soil moisture content from electrical conductivity data collected. Both studies concluded that the EMI method had ample potential for soil moisture mapping while providing fast, accurate and easily-obtained results. These traits have made the EMI method valuable to practitioners of precision agriculture – the discipline related to observing and responding to intra-field variations in agricultural fields (Lück et al., 2009). Within the field of precision agriculture, the EMI method has been widely used to determine field-scale variations in soil moisture content (Corwin and Plant, 2005), particularly in the root-zone (e.g. Hossain et al., 2010), as well as to determine dynamics of complex systems (e.g., agroforestry (Huth and Poulton, 2007) and drainage tiles (Dadfar et al., 2011)). Outside of precision agriculture, the EMI technique has been used to monitor soil moisture in settings such as wetlands (e.g., Moffett et al., 2010) and golf courses (e.g., Allred et al., 2005).

While a significant collection of ERT and EMI studies have currently been published that have advanced the understanding of the geoelectrical response to soil moisture dynamics, there still exists a further need for investigation. This thesis looks at a high-resolution geophysical response to a wide-range of soil moisture occurring in a natural setting during two cycles of annual seasonal conditions experienced in a temperate climate. Previous studies have failed to tackle each of these elements within a single investigation. The use of naturally occurring precipitation events rather than controlled irrigation examines these methods under real-world conditions; however, controlled irrigation experiments have been popular in the literature (e.g. Cassiani et al., 2006; Deiana et al., 2009). Previous studies have not fully investigated climates with substantial seasonal variations, most significantly winters involving freeze-thaw processes, due to the previous locations of survey sites (e.g., Texas (Reedy and Scanlon, 2003; Amidu and Dunbar, 2007), New Mexico (Sheets and Hendrickx, 1995)). The understanding of soil moisture dynamics throughout seasonal variations, especially winter, and how these phenomena affect geophysical techniques that are governed by electrical properties of the subsurface is of significant importance to practitioners in Canada and locations with similar climates.

Additionally, this thesis contains a large time-lapse component. Hydrogeophysical investigations are only recently beginning to fully embrace the advantages of time-lapse studies (i.e., the analysis of repeated measurements over time). Time-lapse methods are instrumental in resolving whether a geophysical response is due to a static or dynamic feature. Binley et al. (2010) stated in their review of the state of hydrogeophysics that our current knowledge in this field can be maximized by placing an increased emphasis on time-lapse investigations. Previous studies have used a time-lapse EMI method for applications such as generating and validating a site-specific model for estimating soil moisture from measured electrical conductivity (Sheets and Hendrickx, 1995; Reedy and Scanlon 2003) or monitoring dynamic subsurface moisture processes (Robinson et al., 2009). Miller et al. (2008) discusses how time-lapse geophysical studies are particularly beneficial for ERT surveys, as an increased number of data sets improves the inversion process and, ultimately, the interpretations made. Previous studies applying time-lapse ERT include the monitoring of seasonal infiltration (e.g., French and Binley, 2004), the monitoring of annual wetting and drying cycles (e.g. Amidu and Dunbar, 2007) and investigating hydraulic connectivity (e.g. Cassiani et al., 2006; Pellicer et al., 2012).

While there exists past studies that have incorporated time-lapse components, this thesis is distinctive in terms of the combination of total length of data acquisition and the frequency of acquisition data. Many previous EMI or ERT studies monitoring annual subsurface moisture dynamics have drawn conclusions from one year of data acquisition (e.g. Amidu and Dunbar, 2007; Pellicer et al., 2012), whereas in this thesis data was acquired for two full annual cycles. A multi-year data set not only allowed for the examination of the geophysical response to the seasonal phenomena (i.e., infiltration, drainage and freeze-thaw processes), but also variation between contrasting annual cycles (e.g., wet versus dry summer conditions). While Reedy and Scanlon (2003) acquired three years of EMI data, their study used a sampling interval of one month (a common sampling interval for studies investigating soil moisture on the annual scale). In contrast, this thesis uses an average sampling interval of two weeks. This higher sampling frequency increases the ability to observe peak and transitional field conditions and monitor dynamics processes. Many studies have used smaller acquisition intervals than this study, however only when looking at short duration injection studies or single-season transitions (e.g., French and Binley, 2004; Cassiani et al., 2006; Robinson et al., 2009).

Studies have proposed that data analysis can be significantly improved by a joint implementation of resistivity and EMI methods (e.g., Bala and Pieta, 2010; Ong et al., 2010; André et al., 2012). While both ERT and EMI methods are dependent on the electrical conductivity structure of the subsurface, recent work has raised a number of questions about the quantitative relationship between these two methods. Lavoué et al. (2010) suggests using ERT data to ensure EMI surveys provide results which are quantitatively comparable. The magnitude of ERT and EMI data collected during various seasonal conditions in this thesis is exactly what is required to examine this issue.

1.2 Study Objectives

The objective of this study is to acquire a densely-sampled time-series of concurrent EMI and ERT data sets covering two annual cycles of near-surface soil moisture conditions. The comparison of the results of the two data sets with one another and with temporal soil moisture, soil texture and weather data from the field site will allow for an examination of the capacity of these two hydrogeophysical techniques to characterize moisture dynamics in the shallow subsurface in this study environment. This hydrogeophysical data set is unique due to the combination of a multi-year monitoring period, dense temporal sampling interval and concurrent use of both the ERT and EMI methods, as well as the supplemental weather and gravimetric information; it will be of great value to further research beyond the scope of the present thesis.

It will be seen in this thesis that temporal variations in the geoelectrical data from both methods qualitatively coincide with seasonal changes in soil moisture content in the upper 0.50 meters inferred from the gravimetric sampling and weather data. As well, it will be found that there is very good qualitative spatial and temporal agreement between the ERT and EMI data set. However, a quantitative analysis will show that more work is necessary to understand the relationships between gravimetric and geoelectrical data. Further, a basic quantitative comparison of the ERT and EMI results reveals potential fundamental differences that require more examination.

Chapter 2 GEOPHYSICAL BACKGROUND

2.1 Electrical Properties of Soils

A review of soil properties affecting geoelectrical studies is presented by Friedman (2005). A summary of these properties is presented in this section. Geoelectrical methods respond to the electrical resistivity or electrical conductivity of the subsurface. Electrical resistivity is the quantification of how well a material opposes the flow of an electrical current. Conversely, electrical conductivity is the quantification of the ability of a medium to permit the flow of an electrical current. Mathematically, the reciprocal of electrical resistivity (ρ) is electrical conductivity (σ):

$$\rho = \frac{1}{\sigma} \tag{2.1}$$

Electrical current flows in the subsurface by three main processes: electronic conduction, electrolytic conduction and interfacial conduction. Electronic conduction refers to current flow via free electrons, such as in metals. Electrolytic conduction is when current flows via the movement of dissolved ions in groundwater. Interfacial conduction refers to current flow through the diffuse double layer that forms along the grain-fluid interface of clay particles in the subsurface material. In typical hydrogeophysical surveys, current flow is dependent on electrolytic conduction and – when clay is present in sufficient quantities – interfacial conduction.

The electrical resistivity of a soil is strongly dependent on its level of water content. Calamita et al. (2012) includes a summary of the mathematical relationships between electrical resistivity and subsurface moisture content implemented in numerous scientific studies covering a wide range of soil textures and survey conditions. It is clear from their summary that a power law type relationship has often been used. Archie’s Equation (Archie, 1942) is a commonly-used power type relationship that provides a relation between electrical resistivity and degree of saturation. Archie’s Equation is given by

$$\rho = a\phi^{-m}S^{-n}\rho_w \tag{2.2}$$

where ρ is the bulk electrical resistivity of a porous solid, ϕ is the porosity, S is the water saturation, ρ_w is the resistivity of the pore water, m is a term called the cementation exponent ($1.3 \leq m \leq 2.6$), n is a term called the saturation exponent and a is an empirical constant ($0.5 \leq a \leq 2.5$) (Schön, 2011). Although Archie's Equation is not strictly valid for soils containing clay, it can still be used to examine the potential ranges in resistivity values expected from moisture content fluctuations. Using Archie's Equation with a range of n from 1.5 – 2 and a range of saturation from 0.10 – 0.70, it can be calculated that electrical resistivity may be 18 to 49 times larger during the driest conditions than during the wettest conditions.

In addition to the materials present, electrical resistivity is also dependent on temperature (Daily et al., 2005). Many researchers have attempted to account for variations in temperature during time-lapse electrical geophysical surveying. Researchers who have done so use empirically-derived equations that attempt to convert electrical conductivity values at acquisition temperatures to equivalent values at 25^{o}C. The two main forms of temperature conversion models currently employed are either exponential-form or polynomial-form equations (Ma et al., 2011). Due to the empirical nature of the models, individual models have temperature ranges over which they are effective. Comparisons of current models by Ma et al. (2011) showed that the Sheets and Hendrickx (1995) model corrected by Corwin and Lesch (2005) was the best of the models tested and was useful for readings acquired between 3 and 50ºC. These equations are an ongoing area of development, with researchers in the field still noting that ample real-world testing of equations using wide-ranges of subsoil conditions is required (Besson et al., 2008).

Regardless of the model (Ma et al., 2011), a value of approximately 2% change in electrical resistivity per change in degree centigrade is often accepted for temperatures between 0 and 35ºC (Campbell et al., 1948). Using this value as a guideline and a range of 20ºC as a typical range of vadose zone temperature for this study (see Section 3.4), it can be expected that temperature fluctuations could cause electrical resistivity variations of up to a factor of 1.5 for the temperatures that could be expected during an annual cycle at this site.

Assuming the geology and groundwater chemistry of the research site remain constant over the two-year study period, then time-lapse geoelectrical study will detect electrical resistivity variations due to changes in moisture content and temperature. As the review in this section suggests, it is likely that moisture variations will have a far greater influence on electrical resistivity than temperature variations under the natural conditions experienced at this research site, which provides the basis of why time-lapse geoelectrical techniques are valuable hydrogeophysical methods.

2.2 Electrical Resistivity Method

Surface electrical resistivity methods are used to determine the distribution of subsurface resistivity by making measurements along the ground surface. Resistivity methods are galvanic techniques that involve monitoring an electrical current that is injected directly into a subsurface using electrodes. An overview of the theory that governs the DC resistivity method is presented in brief in this section; it is thoroughly explained in many sources such as Zonge et al. (2005) and Revil et al. (2012).

Applying an electrical potential difference to a material will result in the flow of an electrical current. The fundamental physical law that governs current flow in a material is known as Ohm's Law. The equation for Ohm's Law for this application is

$$\vec{E} = \rho\vec{j} \tag{2.3}$$

where $\vec{j}$ is the current density at a given point in a material (in Amperes per square metre, A/m^2), $\vec{E}$ is the electrical field at that point (in Volts per metre, V/m) and ρ is the electrical resistivity of the material (in Ohm metres, Ω·m). $\vec{E}$ is related to the electrical potential gradient ∇V at a point in the subsurface using

$$-\nabla V = \vec{E} \tag{2.4}$$

Hence, Ohm's Law can be expressed in terms of electrical potential as follows

$$\nabla V = -\rho\vec{j} \tag{2.5}$$

Electrical resistivity measurements are made using sets of four electrodes: two electrodes to act as the source and sink of the electrical current (called the current electrodes and often designated A and B for the source and sink, respectively), and two electrodes at the points where the electrical potential is to be measured (designated as M and N). The configuration of these four electrodes on the surface is called the array. There are a number of arrays that can be used in resistivity surveys, with each array type possessing strengths and weaknesses that make them more or less suitable for particular situations. Common tradeoffs between array types include signal-to-noise ratio, sensitivity variation with depth and sensitivity to horizontal or vertical structures (Samouëlian et al., 2005). A common array with the four electrodes evenly spaced along the ground surface with the two current electrodes located at the ends of the array is known as a Wenner array (Figure 2.1).

With electrical resistivity surveys, compromise must be made when selecting the minimum electrode separation to use for a study. Increasing electrode separation improves sensitivity at greater depths at the cost of resolution (Furman et al., 2003). Surveys with smaller electrode separations also require an increased number of electrodes to cover a transect of comparable length to larger electrode separations, often resulting in performing roll-along style surveys which are more time intensive.

In practice, a realistic subsurface is an inhomogeneous environment with materials having different electrical resistivity values. Hence, the value measured in the field gives the apparent electrical resistivity that is equal to the electrical resistivity of a homogenous half-space that would produce the same change in electrical potential for the given input current and electrode spacing. For a Wenner array, the apparent resistivity ρ_a can be calculated from a measurement of change in electrical potential ΔV_{MN} with a known current *I* and electrode spacing *a* by the equation

$$\rho_{a_{Wenner}} = \frac{2\pi a}{I} \Delta V_{MN} \tag{2.6}$$

Apparent resistivity measurements allow for the estimation of the resistivity structure of the subsurface. Traditionally, electrical resistivity surveys were performed as profiles or as soundings. Profiling techniques involve traversing an array with fixed electrode separation across a subsurface to detect lateral variations in resistivity at a consistent depth of investigation. Soundings are performed by making multiple measurements with increasing electrode separations (increasing the *a* parameter in Figure 2.1) over a fixed location to detect vertical variations in resistivity.

Combining the two techniques allows two-dimensional characterization along a transect. Modern technology allows for rapid data collection through a multi-electrode system. The results of data collection can easily be represented on a cross-section that positions data points based on their survey location and pseudodepth. The survey location is designated as the midpoint of the electrodes. The pseudodepth is a depth associated with each data point which is a generalization that is necessary due to the complexity of analyzing this property in an inhomogeneous subsurface. Barker (1989) established that the pseudodepth for a Wenner array is $0.17L$, where L is the lateral distance between the two current electrodes used to acquire a specific data point. The cross-section resulting from data points plotted at their survey locations and pseudodepths is called a pseudosection (Figure 2.2). A pseudosection gives preliminary insight into apparent electrical resistivity variation in the subsurface but not the actual resistivity structure.

Mathematical inversion of the data is performed to obtain possible models of the subsurface resistivity structure that are consistent with the measured data (Loke, 2011). Inversion is an iterative process in which a model is obtained by iteratively attempting to fit the acquired data (Sasaki, 1992). Inversion parameters such as number of model blocks, model block size and inversion smoothness will influence the resulting inversion and must be chosen to best suit the survey type.

2.3 Electromagnetic Induction Method

Electromagnetic induction surveys are performed to characterize subsurface electrical conductivity. The EMI technique involves generating an electromagnetic (EM) field that induces a secondary EM field whose properties can be analyzed to determine characteristics about the subsurface. Unlike galvanic electrical techniques such as electrical resistivity tomography, the EMI technique does not require direct coupling with the subsurface. A summary of EMI techniques can be found in Keller and Freschknecht (1966) and Fitterman and Labson (2005). A general overview is given in this section.

The foundation of the EMI technique is explainable through a number of fundamental physical laws (Keller and Frischknecht, 1966). The first is Ampère’s Law, which states that a magnetic field H is produced by the presence of an electric current I and that the strength of associated H and I are proportional. Faraday’s Law states that an electric field E is produced by a time-varying magnetic field, and that the strength of E is proportional to the rate of change of the associated H with respect to time. Therefore, a voltage V will be induced in any medium subjected to a time-varying magnetic field, thus producing a flow of eddy currents. The current in the circuit will obey Ohm’s Law, as given in Equation 2.3.

The EMI technique consists of two coils: a transmitter and a receiver. Consider the coils positioned on a homogeneous Earth's surface in a given orientation and separated by a known distance s (Figure 2.3). As per the phenomena discussed above, an alternating current I generated in the transmitter coil will cause the production of a magnetic field H called the primary field (Figure 2.4a). The Earth acts as a closed circuit that interacts with H. Eddy currents I' begin to flow in the Earth circuit as it interacts with the primary field (Figure 2.4b). The flow of current in the Earth circuit is governed by Ohm's Law and, therefore, is affected by the electrical resistivity of the Earth ρ. The existence of I' produces a magnetic field H' called the secondary field (Figure 2.4c). A current begins to flow in the receiver coil as it senses the secondary field. The voltage of the electrical current flowing through the receiver coil can be measured. As required by Ampère's and Faraday's Laws, the strength of each induced magnetic field, electric field and electrical current involved in this network is proportional in strength to the original alternating current in the transmitter coil. Thus, the resulting secondary field is a function of few variables: the alternating current's frequency f, the separation distance of the coils and the conductivity of the Earth σ (= ρ^{-1}).

In practice, a realistic subsurface is an inhomogeneous environment which will result in a primary field interacting with materials of many different electrical conductivity values. Hence, the value measured by a standard EMI device called a ground conductivity meter (GCM) is the apparent electrical conductivity. In one-dimension, an inhomogeneous subsurface can be represented as a horizontally-layered system. The apparent electrical conductivity of this system measured by the GCM is a depth-weighted average of the conductivities present in the subsurface layers. The manner in which the various subsurface conductivity values are weighted is dependent on the orientation of the primary field relative to the Earth. GCM are manufactured so that they can be easily operated with the central axis of the primary field either perpendicular to or parallel with the ground surface. Figure 2.5 illustrates the two orientations used by the devices employed in this work. A quantity called normalized depth z' is related to the actual depth z by the equation

$$z' = \frac{z}{s} \tag{2.7}$$

Equation 2.7 is useful for the discussion of GCM response as the response of a GCM with respect to z is consistent between instruments of different coil separations. The response functions defining the relative contribution to the apparent electrical conductivity of electrical conductivities present in a one-dimensional subsurface at z' are given by the equations

$$\phi_v(z') = \frac{4z'}{(4z'^2+1)^{\frac{3}{2}}} \tag{2.8A}$$

$$\phi_h(z') = 2 - \frac{4z'}{(4z'^2+1)^{\frac{1}{2}}} \tag{2.8B}$$

where $\phi(z')$ is the relative contribution at normalized depth z' and subscript v and h denote the equations for the vertical and horizontal dipole orientations, respectively (Keller and Frischknecht, 1966). These equations have been plotted in Figure 2.6. It is apparent from this figure that the horizontal dipole is more sensitive than the vertical dipole to the shallow subsurface. In fact, directly at the ground surface the response in the vertical dipole orientation is zero. The vertical dipole orientation however offers significant sensitivity to greater depths.

Therefore, if $\sigma(z')$ describes how electrical conductivity varies in a one-dimensional subsurface, then the apparent electrical conductivity of the subsurface σ_a can be defined by the equation

$$\sigma_a = \int_0^\infty \phi\,(z')\sigma(z')\,dz' \tag{2.9}$$

where $\phi(z')$ is the response function for a given coil arrangement.

In a one-dimensional subsurface with N layers, subsurface apparent electrical conductivity can be defined by the equation

$$\begin{aligned}\sigma_a = \sigma_1[1-R(z')] + \sigma_2[R(z'_1)-R(z'_2)] + \sigma_3[R(z'_2)-R(z'_3)] \\ + \cdots + \sigma_{N-1}[R(z'_{N-2})-R(z'_{N-1})] + \sigma_N[R(z'_{N-1})]\end{aligned} \tag{2.10}$$

where σ_n is the electrical conductivity of layer n and $R(z')$ is the cumulative response of the GCM given by the equations

$$R_v(z') = (4z'^2 + 1)^{-\frac{1}{2}} \tag{2.11A}$$

$$R_h(z') = \left(4z'^2 + 1\right)^{\frac{1}{2}} - 2z' \tag{2.11B}$$

for the vertical and horizontal dipole orientations, respectively.

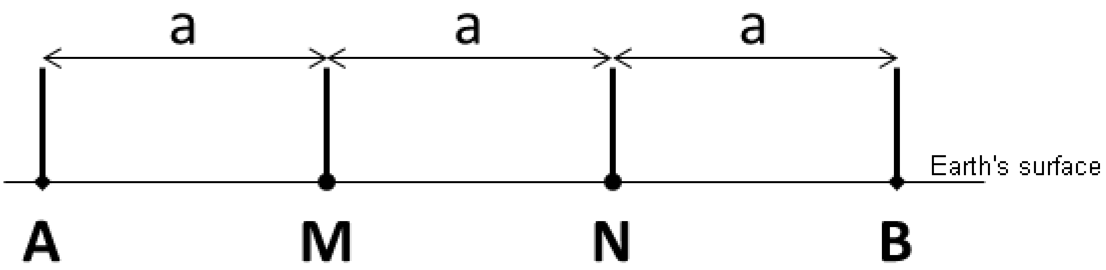

Figure 2.1 – The electrode positions for a Wenner array. The source electrode (A), sink electrode (B) and two potential electrodes (M and N) are uniformly spaced in the order shown.

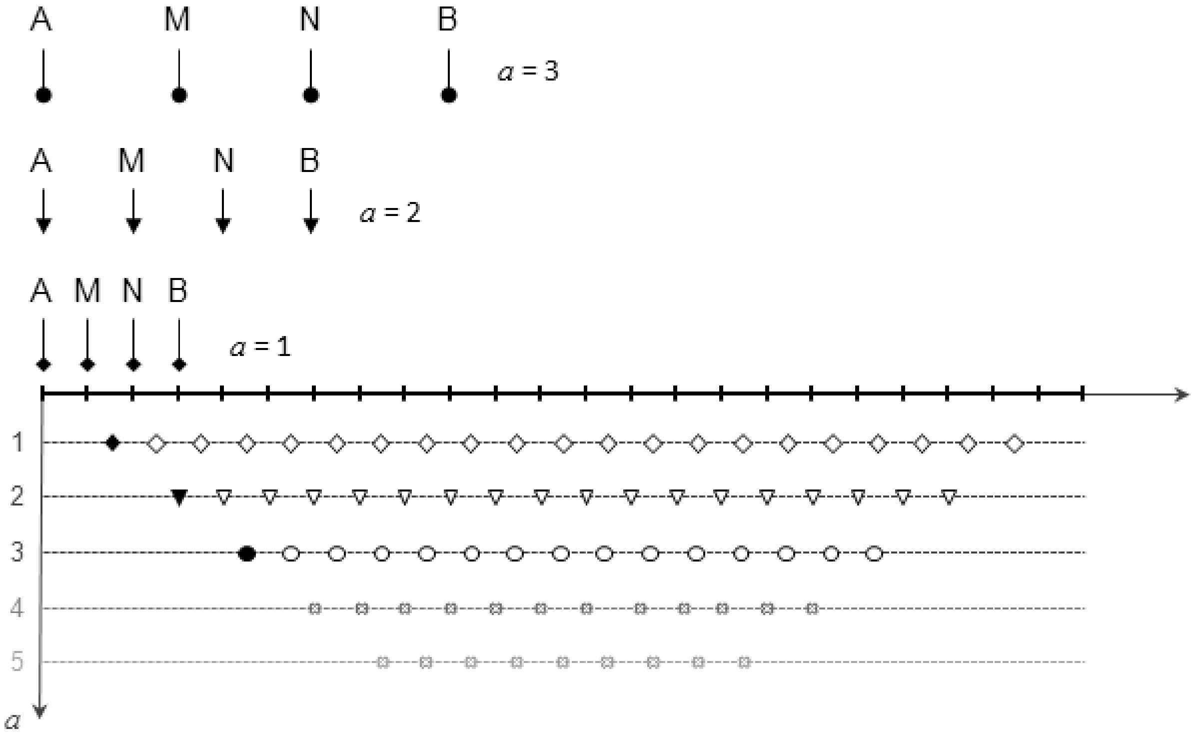

Figure 2.2 – A schematic for the construction of a pseudosection of apparent resistivity data collected in the Wenner array. The array midpoint is plotted against depth level (denoted by array parameter *a*).

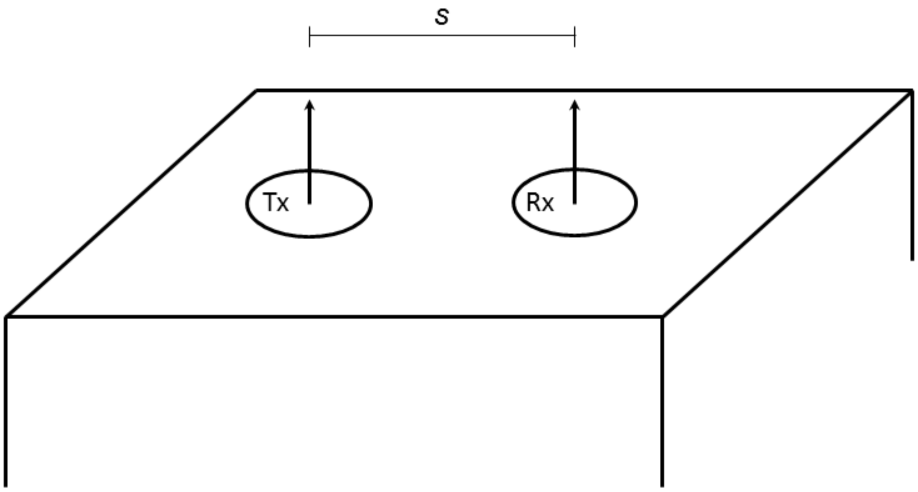

Figure 2.3 – Transmitter (Tx) and receiver (Rx) coils on a homogeneous Earth. Coils are a distance apart *s* and are in the same orientation.

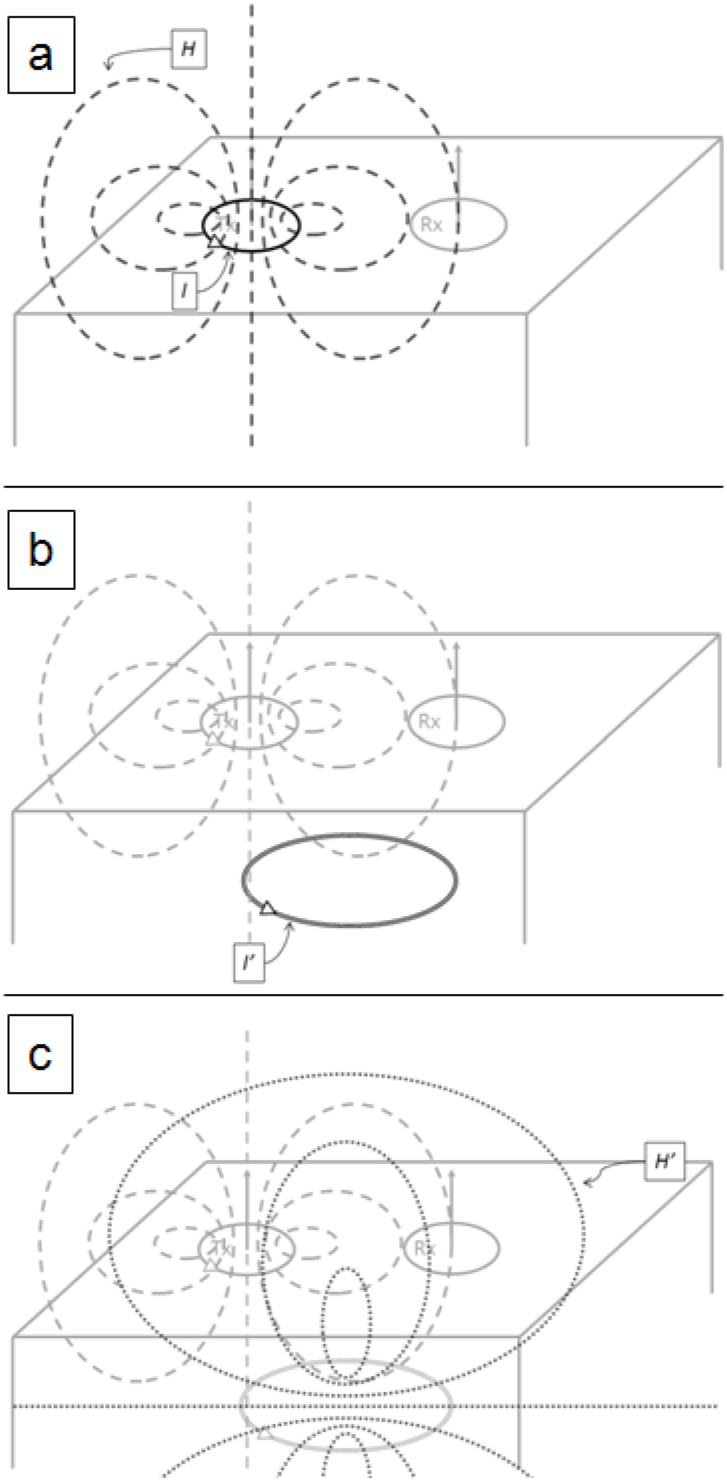

Figure 2.4 – A schematic of the electromagnetic induction process. a) An alternating current *I* flowing in the transmitter coil induces the primary field *H* b) The Earth circuit interacts with *H*, generating the flow of eddy currents *I´*. c) *I´* induces the secondary field *H´* which is sensed by the receiver coil.

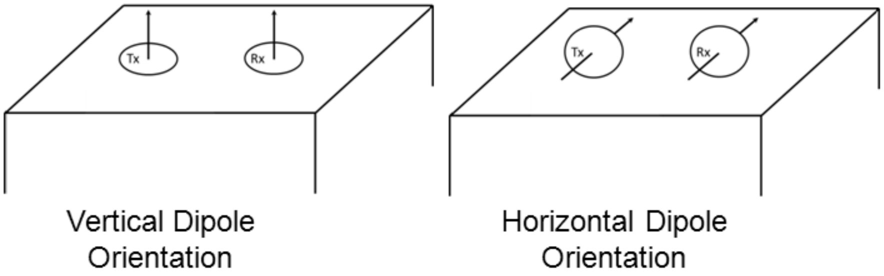

Figure 2.5 – A diagram of the vertical and horizontal dipole orientations.

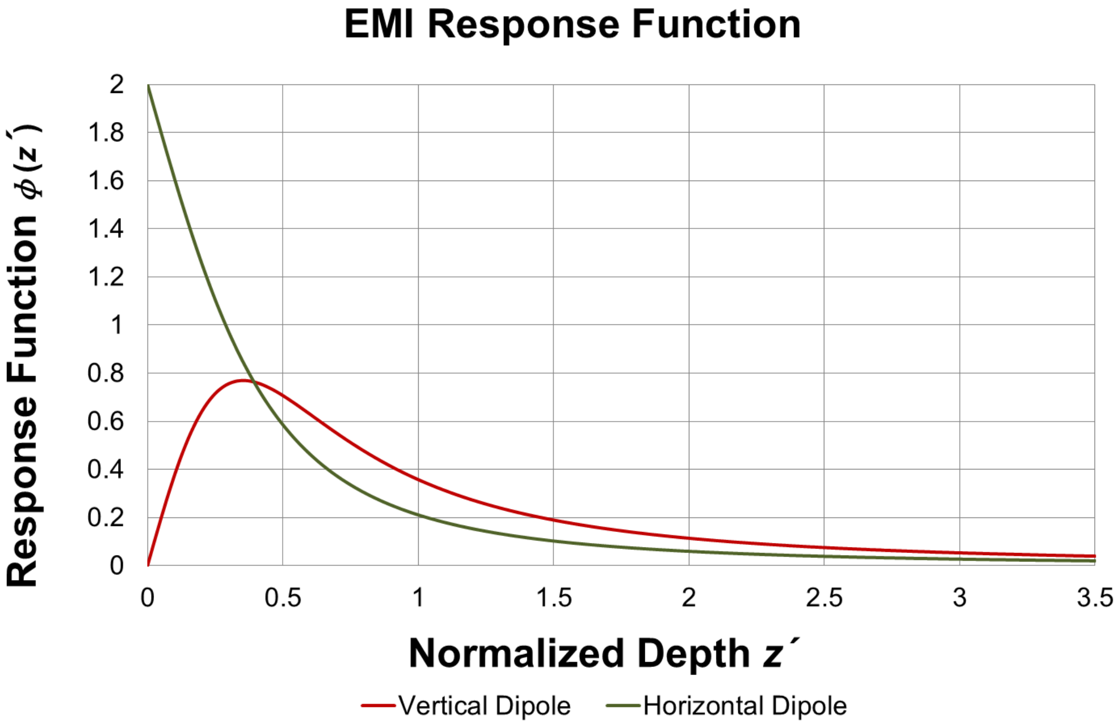

Figure 2.6 – Relative contributions to the total apparent electrical conductivity of subsurface features located at normalized depths between 0 and 3.5.

Chapter 3 VINELAND FIELD SITE

3.1 Introduction

The Rittenhouse Grape Research Station (RGRS) is an experimental vineyard operated by the University of Guelph in the village of Vineland, Ontario (43º 09’ 56” N, 79º 24’ 53” W) (Figure 3.1). The RGRS has an area of 14 ha and is located on the Niagara Peninsula approximately 3.5 km south of Lake Ontario, 32 km north of Lake Erie and 1 km north of the Niagara Escarpment. The elevation of the property is 96 metres above sea level and 22 metres above Lake Ontario. The vineyard grows an assortment of grapes for use in various viticultural studies, thus is subjected to typical vineyard agricultural practices during the growing months.

3.2 Test Site Layout

The study was performed at five sites within the RGRS. Figure 3.2 shows the locations of these five sites superimposed on a satellite image of the station. Each site consists of a 25-metre survey profile. Wooden stakes were placed at both line ends at each site prior to the first acquisition day to ensure that a non-metallic measuring tape would be set-up in the same position during each survey. Each site is oriented in an approximately east-west direction with the 0-metre mark located on the eastern-most end. The trellises at the RGRS trend north-south, resulting in the trellis pattern and the survey lines intersecting perpendicularly. However, only the survey lines at Sites 1 and 2 actually intersect with trellises, as the survey lines at Sites 3, 4 and 5 are located in an open area between trellis sections (Figure 3.3). The spacing between trellises differs slightly between monitoring sites. At Sites 1 and 2, the trellises are separated by approximately 3 metres; whereas at Sites 3, 4 and 5, they are separated by approximately 2.5 metres. Sites 1 and 2 are both missing trellises near the centre of the survey line due to the presence of access lanes. Table 3.1 lists the locations on each survey line of actual and projected intersections between trellises and survey lines. Drainage tiles are necessary at the research site due to the clay composition of the subsurface. The drainage tiles run parallel to the trellises at the midpoint between each trellis set.

Sites 1, 3, 4 and 5 have no significant topography variations. Site 2 is located on the slope of a knoll. A minor elevation change occurs gradually along the profile line at Site 2 with the 0-metre mark at the uphill end.

3.3 Non-Geophysical Data Acquired

3.3.1 Weather Data

An automated weather station maintained by the Ontario Ministry of Agriculture, Food and Rural Affairs located at the Vineland Research Station provided weather data throughout the two-year study period. This weather station is located 2 km northeast of the RGRS. Daily values of ambient temperature (maximum, minimum and mean) and precipitation (total rain, total snow, total precipitation and depth of snow on ground) are publicly available for download online. The weather station at the Vineland Research Station did not report precipitation data for 37 dates during the two-year study period. For 28 of these dates, data from surrounding weather stations indicate there was likely no precipitation. For the remaining 9 dates, data from the Grimsby Mountain weather station located 15 kilometres west of the Vineland Research Station was used to estimate the missing information.

Figure 3.4 gives the daily and cumulative precipitation recorded over the two-year study period. Figure 3.5 displays the daily mean ambient air temperature for the same period. The data shows temperatures and precipitation patterns that are typical of areas with temperate continental climates. Spring (March – May) and autumn (August – November) months are considerably more wet than summer (June and July) and winter (December – February) months. Both data sets also depict variations in the intensity of the seasons between the two annual cycles studied. In the spring months, the first annual cycle of monitoring observed 365.7 mL of precipitation compared to 112.4 mL recorded for the same period of the following year. The winter season of 2010 – 2011 contained 90 days where mean ambient air temperature was below 0ºC compared to 40 days of freezing temperatures during the 2011 – 2012 winter season. The data also shows the summer of 2012 was drier and hotter than the summer of 2011. Days within the June – August interval in 2011 had an average daily mean ambient temperature of 21.7ºC and total precipitation of 178.1 mL compared to an average daily mean ambient temperature of 22.5ºC and total precipitation of 120.4 mL for the same interval of 2012.

Historical soil temperature data from the Vineland Research Station weather station was obtained for seven depths between 0.05 and 3.00 metres as a monthly average from observations spanning 30 years (1971 – 2010) (Environment Canada, 2014). This data has been reproduced in Table 3.2. This soil temperature data gives an estimate of how temperature varies within the subsurface at the RGRS to the depths of interest in this study.

3.3.2 Soil Texture

A soil-map published by Agriculture Canada (Edwards, 1989) provides a general guide to the soil textures present in the area of the RGRS. The map is low resolution compared to the size of the RGRS, but does delineate a difference in soil texture between Site 2 and the other four monitoring sites. The soil at Site 2 is described as very fine sandy loam of lacustrine origin, whereas the rest of the RGRS is noted to be covered with 0.15 – 0.40 metres of loam over 1 metre of reddish-hued silty clay loam over Queenston shale bedrock (Edwards, 1989).

Particle-size analyses were performed on samples collected at each of the five monitoring sites to further characterize the soil textures. A hand auger was used to collect soil at two intervals: i) 0 – 0.15 m and ii) 0.45 – 0.60 m. The samples were collected approximately 2 metres away from the midpoint of each monitoring site's survey line. Hydrometer analysis was required to determine particle size distributions as all samples were able to pass through a sieve of mesh size 230 (approximately 0.063 mm).

Table 3.3 displays the results of the hydrometer analysis. The results from Sites 3, 4 and 5 conform to the USDA classification for silty clay at both depths. Sites 4 and 5 showed no significant change in texture between the two depths analyzed while a slight increase in the clay component was observed at the 0.45 – 0.60 m depth interval at Site 3. Site 1 is composed of an upper silty clay material similar to Sites 3, 4 and 5 overlying a siltier material that fits the USDA classification for silty clay loam. The textural change at Site 1 between the two measurement intervals agrees with field observations made with a soil probe identifying an abrupt soil texture change at a depth of 0.35 metres. The soil at Site 2 consists of significantly less clay and more silt than the other sites, conforming to a USDA classification of silt loam. Overall, the results of the particle-size analysis are in reasonable agreement with the published soil-map.

3.3.3 Soil Moisture

Soil samples were collected for moisture content analysis on all acquisition days between 19 April 2011 and 24 September 2012 with the exception of 04 September 2012, totalling thirty-four sampling dates. At each of the five monitoring sites, a soil probe was used to collect soil samples for three depth intervals: i) 0 – 0.25 m, ii) 0.25 – 0.50 m, iii) 0.50 – 0.75 m. Samples were collected at each site in an area approximately 2 metres away from the 12-metre mark on the survey profile. Freezing in the winter and clay-hardening in drier conditions impeded sampling from the deeper intervals at all sites. When possible, a fourth sample interval (0.75 – 1.00 m) was collected at Site 2. Each sample consisted of approximately 50 – 100 grams of soil. The soil was weighed before and after being placed in an oven at 105°C for 24 hours to determine gravimetric moisture content.

To determine volumetric moisture content values from these gravimetric calculations, the bulk density of the material must be known. Bulk density values were measured for each soil texture present. The measurement was performed by drying then weighing a known volume of undisturbed soil collected from pits dug near survey profile locations. In total, 15 soil samples were collected from the three soil textures identified. Table 3.4 gives the resulting bulk density values.

Figure 3.6 displays the results of gravimetric analyses on the collected soil samples. The measurements show periods of wetting and drying that qualitatively fit with the seasonal conditions experienced at this location (i.e., wet spring and autumn periods, dry summer periods). The results display distinct differences in the behaviour of subsurface moisture at Site 2 compared to Sites 1, 3, 4 and 5. At Site 2, all intervals appear to display similar soil moisture values and levels of seasonal soil moisture fluctuation. At Sites 1, 3, 4 and 5, there is a consistent trend of decreasing moisture content with depth during wet periods that is not present during the dry summer periods. Also, the magnitude of fluctuation in seasonal soil moisture decreases with depth.

Figure 3.7 allows for a comparison of volumetric moisture content between monitoring sites using the 0 – 0.50 m interval at each site. It is evident that Sites 4 and 5 consistently experience the driest conditions throughout the study period.

As soil conditions grew increasingly drier, desiccation cracking was easily observable at Sites 1, 3, 4 and 5 (i.e., the clay-rich sites). Figure 3.8 shows a desiccation crack along with one of the survey lines. Crack depths were measured during multiple dry acquisition days. Typical crack depth ranged from 0.05 – 0.15 metres. Cracks observable from the surface appeared to completely close after seasonal wetting had occurred.

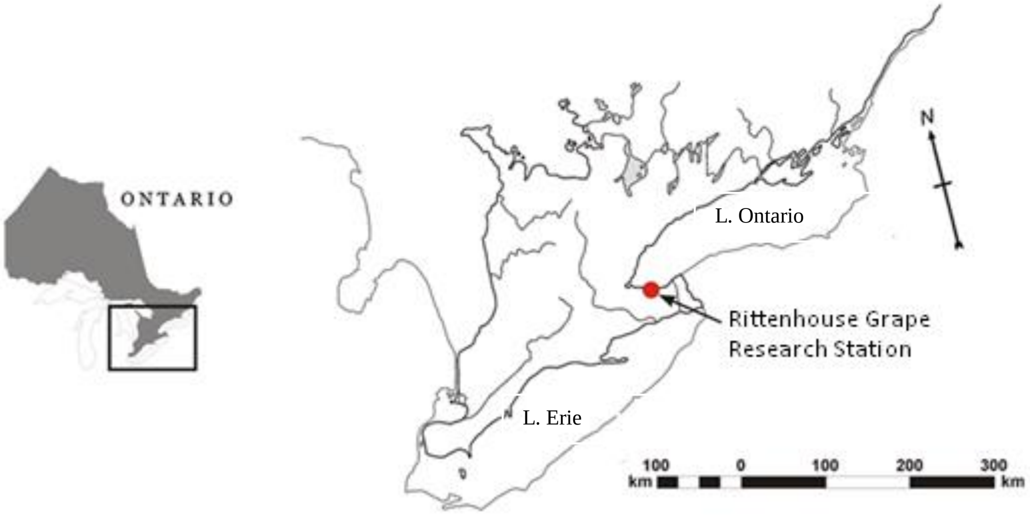

Figure 3.1 - The location of the Rittenhouse Grape Research Station.

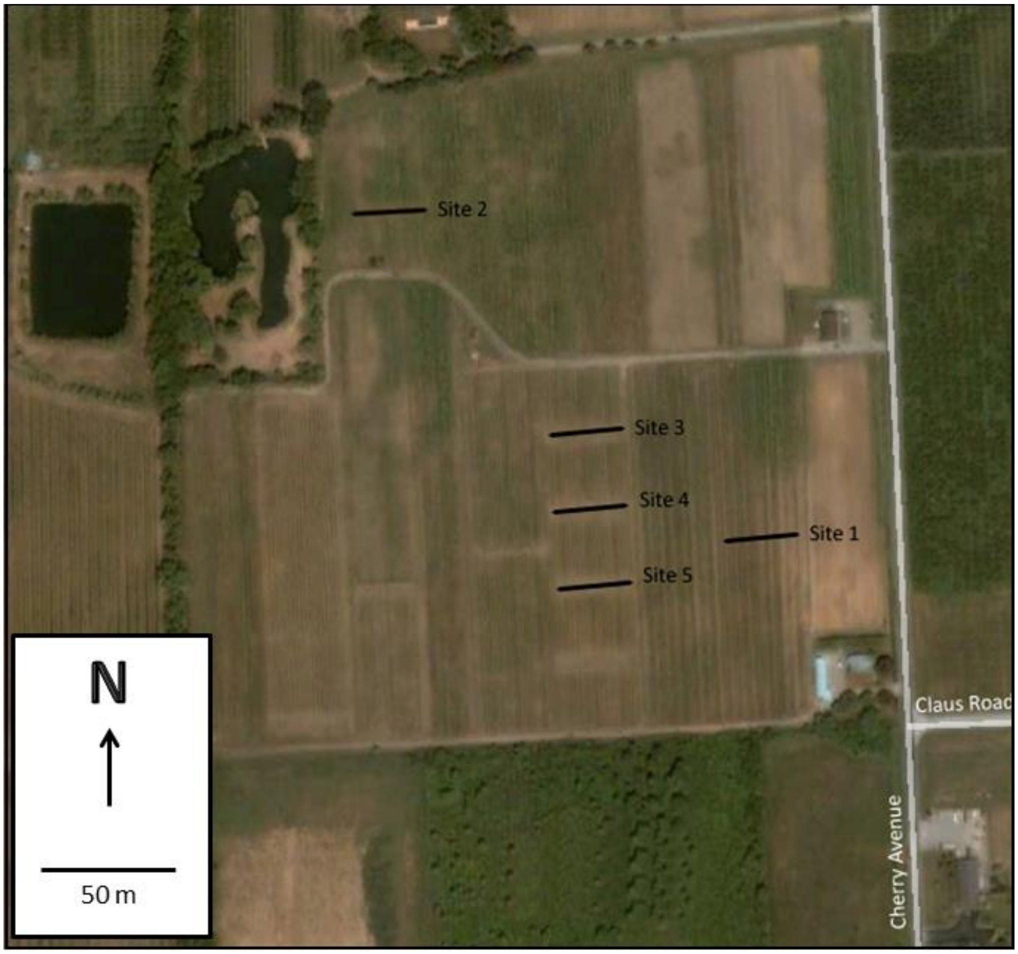

Figure 3.2 – The locations of the five monitoring sites at the RGRS. Map data © 2011 DigitalGlobe.

Figure 3.3 – Examples of the two types of survey line layout. a) The survey lines at Sites 3, 4 and 5 exist in open areas where trellises are not continuous. Shown here is Site 3. b) The survey lines at Site 1 and 2 intersect the trellises. Shown here is a portion of Site 2. Table 3.1 lists the locations on each survey line of actual and projected intersections between trellises and survey lines.

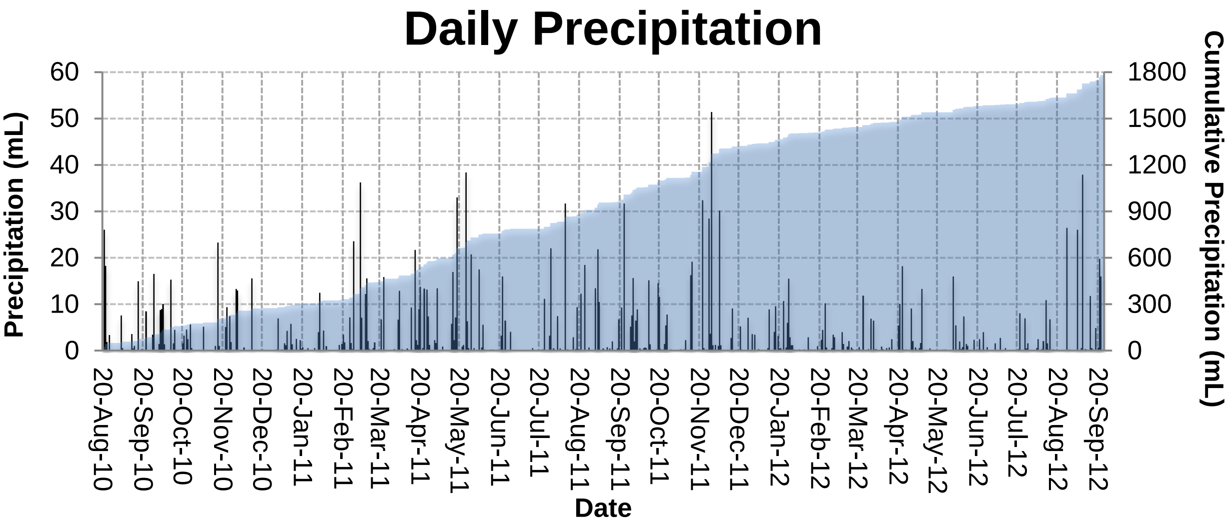

Figure 3.4 – Daily and cumulative precipitation recorded at the Vineland Research Station during the two-year study period.

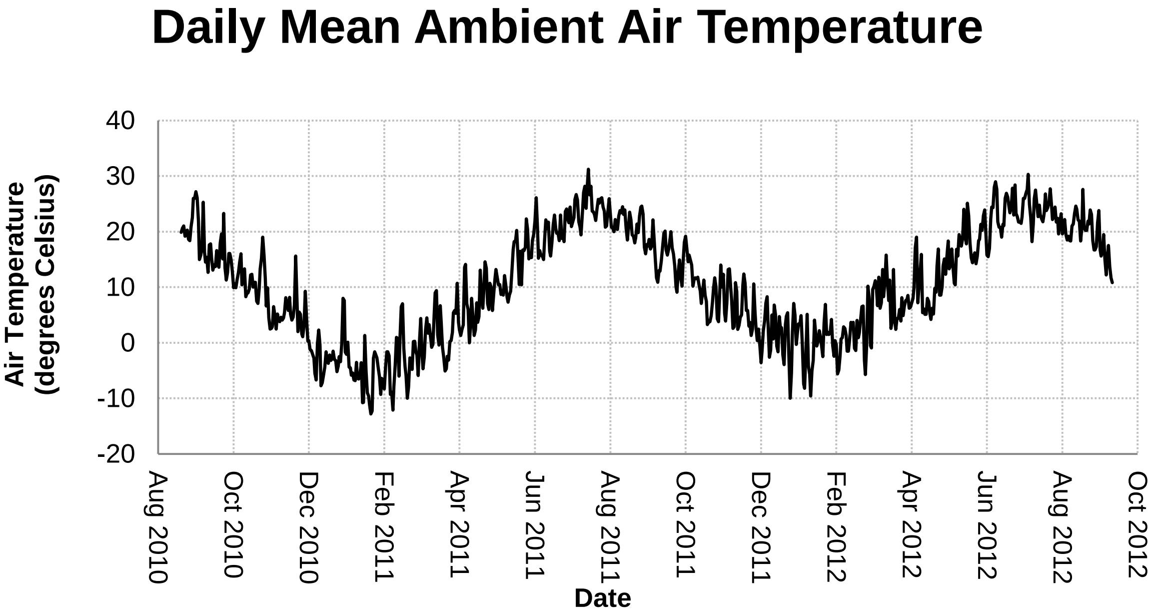

Figure 3.5 – Daily mean ambient air temperature recorded at the Vineland Research Station during the two-year study.

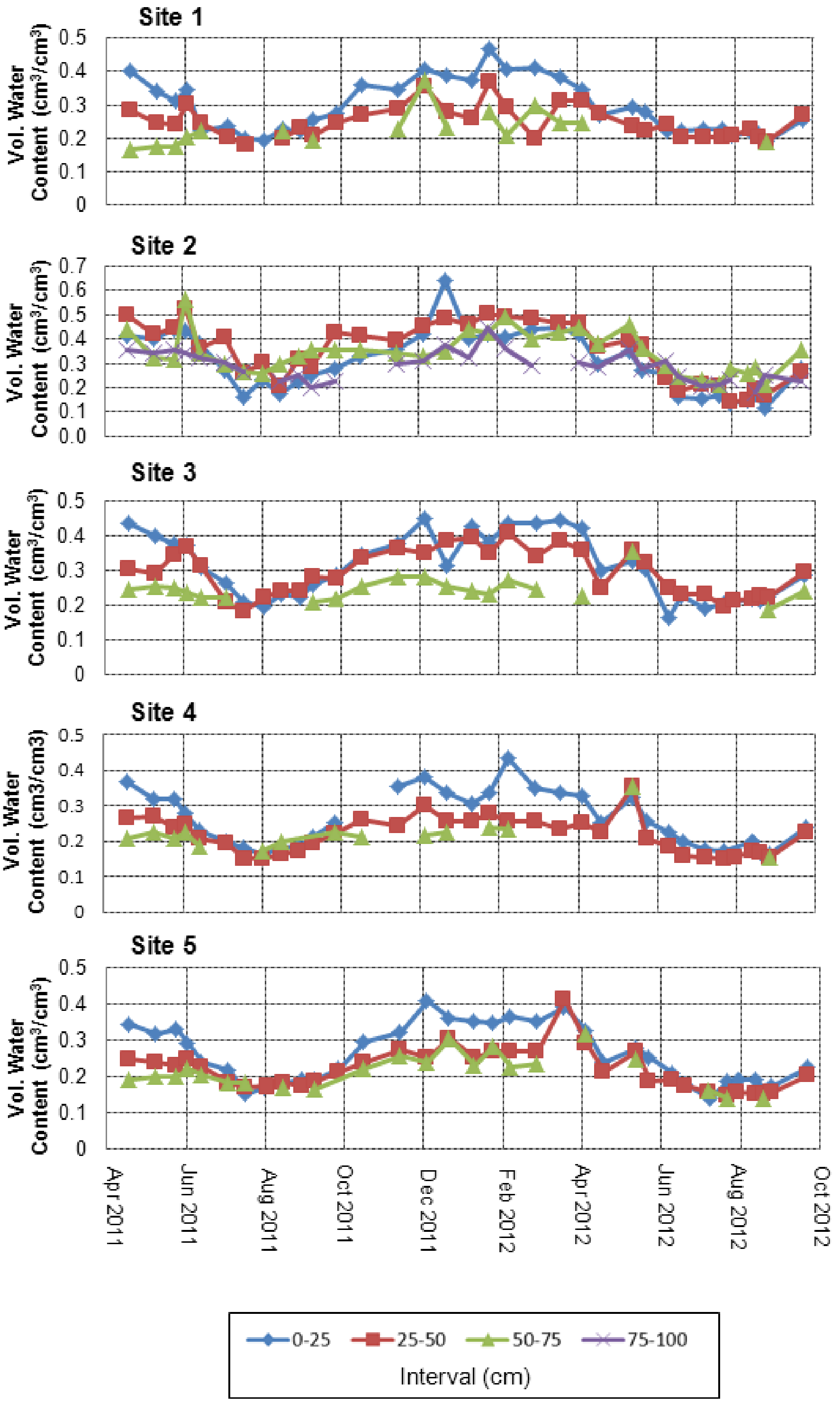

Figure 3.6 – Results of gravimetric moisture sampling at each of the five monitoring sites converted to volumetric water content values. Gravimetric samples were collected each acquisition day between 19 April 2011 and 24 September 2012 except for 04 September 2012 at Sites 1, 2, 4 and 5.

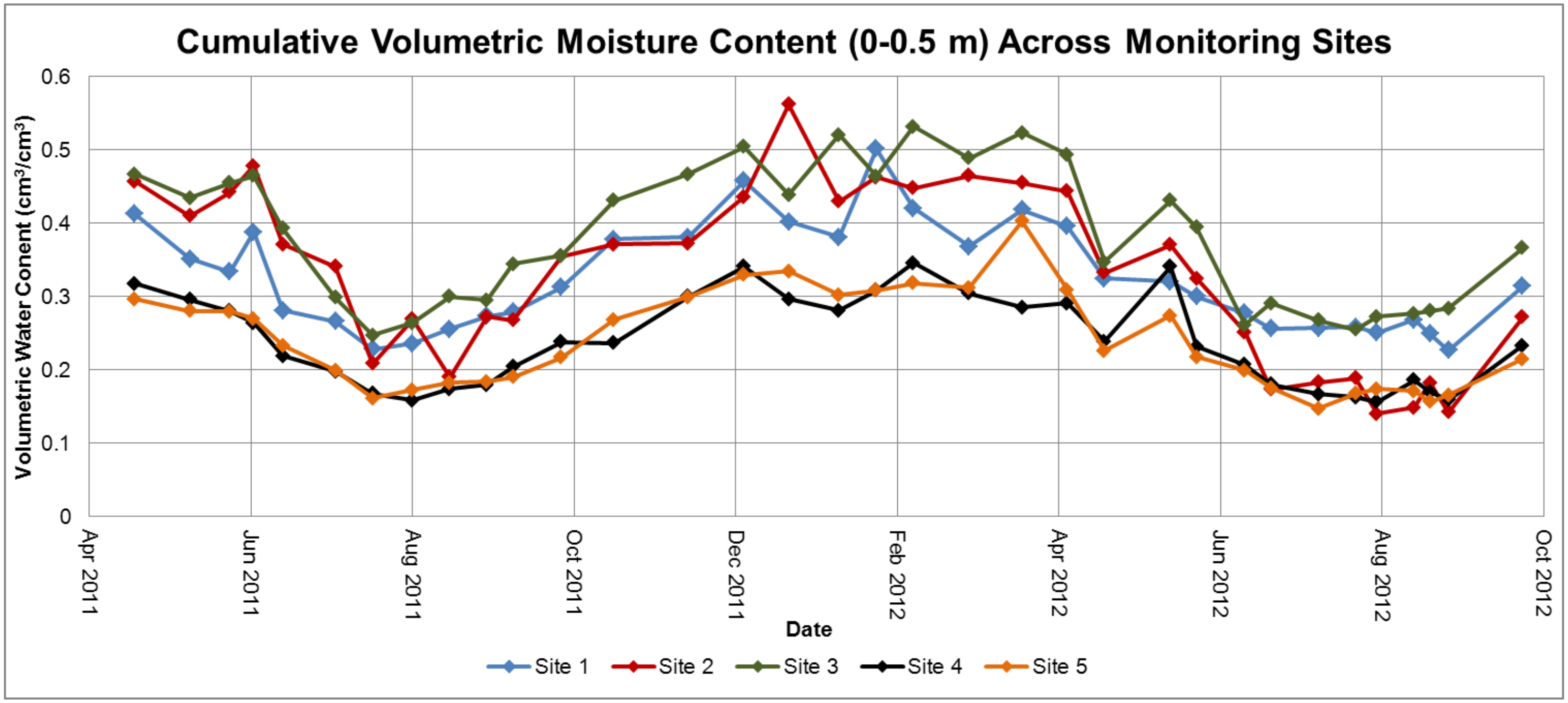

Figure 3.7 – Comparison of volumetric moisture content results for the interval 0 – 0.50 m at each monitoring site.

Figure 3.8 – Desiccation cracks typical of those that form in the area of Sites 1, 3, 4 and 5 during dry conditions. The measuring tape units are inches.

Table 3.1 – List of intersection points between trellises and survey lines. Points for Sites 3, 4 and 5 are projections between trellises adjacent to open areas.

Intersection Points (metres on survey line)
Line 1
0.0, 3.1, 6.1, 9.3, 16.9, 20.0, 23.5, 26.4
Line 2
0.1, 3.5, 6.8, 13.6, 17.0, 20.3, 23.6
Line 3
0.2, 2.6, 5.1, 7.6, 10.1, 12.6, 15.1, 17.5, 20.1, 22.7
Line 4
0.1, 2.7, 5.2, 7.7, 10.2, 12.7, 15.2, 17.8, 20.3, 22.7
Line 5
0.0, 2.8, 5.3, 7.8, 10.3, 12.8, 15.3, 17.9, 20.4, 22.6, 25.2

Projected

Table 3.2 – Average monthly soil temperatures (degrees Celsius) for depths down to 3 metres from 30 years of observations (1971 – 2000) collected at the Vineland Research Station weather station (Environment Canada, 2014).

	Depth (m)						
Month	**0.05**	**0.10**	**0.20**	**0.50**	**1.00**	**1.50**	**3.00**
Jan	0.5	0.8	1.5	3	4.6	6.2	8.4
Feb	0.1	0.3	0.8	2.1	3.3	4.7	6.8
Mar	1.2	1.3	1.6	2.4	3.1	4.1	5.9
Apr	6.0	6.1	6.3	5.8	5.4	5.2	5.9
May	12.0	12.1	12.0	10.8	9.5	8.4	7.6
Jun	17.4	17.4	17.2	15.6	13.6	11.9	10.1
Jul	20.6	20.7	20.5	18.9	16.9	15	12.6
Aug	20.4	20.7	20.7	19.8	18.3	16.8	14.6
Sep	17.2	17.7	18	18.2	17.7	16.9	15.4
Oct	11.8	12.2	13.0	14.1	14.8	15.0	14.7
Nov	6.9	7.4	8.1	9.7	11.0	12.1	13.0
Dec	2.7	3.1	3.8	5.6	7.2	8.8	10.7
Year	*9.7*	*10.0*	*10.3*	*10.5*	*10.5*	*10.4*	*10.5*

Table 3.3 – Results of hydrometer analysis performed to determine clay percentage at each site. Each value is the average result of three trials. The particle diameters for each category are as follows: Coarse Silt: 0.04 – 0.063 mm, Fine Silt: 0.002 – 0.04 mm, Clay: <0.002 mm.

	Interval 1: 0 – 0.15 m			**Interval 2: 0.45 – 0.60 m**		
Site 1	**Coarse Silt (%)**	**Fine Silt (%)**	**Clay (%)**	**Coarse Silt (%)**	**Fine Silt (%)**	**Clay (%)**
	15	32	53	14	47	39
	USDA Class.: silty clay			**USDA Class.:** silty clay loam		
Site 2	**Coarse Silt (%)**	**Fine Silt (%)**	**Clay (%)**	**Coarse Silt (%)**	**Fine Silt (%)**	**Clay (%)**
	28	57	15	27	54	19
	USDA Class.: silt loam			**USDA Class.:** silt loam		
Site 3	**Coarse Silt (%)**	**Fine Silt (%)**	**Clay (%)**	**Coarse Silt (%)**	**Fine Silt (%)**	**Clay (%)**
	20	30	50	4	39	57
	USDA Class.: silty clay			**USDA Class.:** silty clay		
Site 4	**Coarse Silt (%)**	**Fine Silt (%)**	**Clay (%)**	**Coarse Silt (%)**	**Fine Silt (%)**	**Clay (%)**
	17	37	46	2	55	43
	USDA Class.: silty clay			**USDA Class.:** silty clay		
Site 5	**Coarse Silt (%)**	**Fine Silt (%)**	**Clay (%)**	**Coarse Silt (%)**	**Fine Silt (%)**	**Clay (%)**
	13	42	45	3	49	48
	USDA Class.: silty clay			**USDA Class.:** silty clay		

Table 3.4 – Bulk density values obtained from undisturbed soil samples for each soil texture present at the monitoring sites.

Soil Texture	Bulk Density
silty clay	1.2 g/cm^3
silty clay loam	1.3 g/cm^3
silt loam	1.4 g/cm^3

Chapter 4 MONITORING SOIL MOISTURE DYNAMICS BY ELECTRICAL RESISTIVITY TOMOGRAPHY

4.1 Introduction

High-resolution electrical resistivity tomography (ERT) surveys were performed at the five monitoring sites over two annual cycles for the purpose of monitoring subsurface electrical resistivity evolution due to soil moisture dynamics. In total, there were forty-four ERT acquisition days between 15 September 2010 and 24 September 2012. Each acquisition date includes ERT surveys from all five sites except for acquisition dates between 15 December 2010 and 18 March 2011 when surveys were not performed at Sites 4 and 5 and 04 September 2012 when data was only acquired at Site 3. The monitoring schedule is summarized in Table 4.1.

4.2 ERT Data Acquisition

The data was collected in the field using a Syscal Junior Switch-48 (Iris Instruments; Orléans, France) which is a 48-electrode resistivity imaging system. The Wenner array was chosen due its good signal-to-noise ratio and imaging resolution in the near-surface (Samouëlian et al., 2005). A half-metre electrode spacing was chosen as it offered a good compromise between high-resolution imaging of the near surface and sufficient depth of investigation.

The field system follows a sequence file to determine which electrode configurations are to be used. The sequence file was built and uploaded onto the field system using Electre II version 2.00 (Iris Instruments; Orléans, France). The sequence consists of a Wenner array with electrode separations (values of *a*) at all half-metre intervals from 0.5 to 6.0 metres. This sequence generates a 24-metre survey transect with a total of 342 measurements using 12 electrode spacings resulting in an approximate depth of investigation of 3 metres (Barker, 1989).

At the start of each survey, the electrodes were inserted into the ground to a depth of approximately half of their length (i.e., to a depth of 0.15 metres). When inserting the electrodes into the ground, care was taken to ensure good contact was established between the electrodes and the soil. Ensuring proper contact is especially important during drier conditions when holes formed by the electrodes may not have naturally healed between acquisition days. An RS-check was performed prior to any data acquisition to ensure the system was properly connected and to monitor the level of contact resistance in the survey setup. Data was collected with a current-injection period of 1000 ms and a minimum of 4 stacks.

4.3 Management and Inversion of ERT Data

Following data acquisition, resistivity data were downloaded from the field system to a desktop computer using the software program Prosys II version 3.02 (Iris Instruments; Orléans, France). Quality control was performed to ensure the data was properly acquired and transferred.

Inversion of the data was performed using the software package RES2DINV version 3.58 (Geotomo Software; Penang, Malaysia). The program generates a two-dimensional model of subsurface resistivity by minimizing the root-mean-square (RMS) difference between the predicted apparent electrical resistivity from an inversion model and the values measured in the field. The model is composed of layers of rectangular model blocks each possessing an electrical resistivity value. Inversions were performed using the robust inversion method. This method was chosen over the rapid least-squares inversion method as it allows for abrupt changes between resistivity in neighbouring model blocks (Geotomo, 2010).

The model block width was set to 0.25 metres (half the distance of the smallest electrode separation) as recommended in the program manual for data sets with the potential for high resistivity variations in the near surface (Geotomo, 2010). Model block thickness was chosen to increase with depth. Twenty-six layers of model blocks were chosen with the shallowest model block's thickness set to 0.03125 metres and each consecutively deeper layer of model blocks increasing in thickness by 10%. The fine spatial discretization allows the inversion process to better handle the rapid lateral and vertical variations in electrical resistivity that could occur in the shallow near surface due to changes in soil moisture. The resulting number of model blocks is 1860. Figure 4.1 shows the distribution of these model blocks relative to the 342 acquired data points. The location of the acquired data points is based on their pseudodepth as explained in Section 2.2.

RES2DINV's time-lapse inversion technique was used as opposed to inverting each data set independently. Time-lapse inversion allows for the inversion process to begin with previous inversion results as a reference model that assists in constraining later time-lapse data sets (Loke, 1999). In the style of time-lapse employed here, the inversion of a data set for any given date uses the inversion result from the preceding date as the reference model with constraining accomplished using a least-squares smoothness technique (Geotomo, 2010). Data sets are inverted "simultaneously", meaning all data sets complete the same round of inversion iteration before starting subsequent iterations. Miller et al. (2008) concluded that simultaneous time-lapse inversion yielded less noisy results compared to other common time-lapse inversion techniques. The ultimate result of the time-lapse inversion method is a more reliable inverted image of the subsurface that not only has minimized the difference between observed and calculated resistivity values but also preserves the consistency of subsurface features with time.

An initial damping factor of 0.15 and minimum damping factor of 0.02 were used as it is recommended in the manual for data sets with low to moderate noise (Geotomo, 2010). RES2DINV parameters that increase accuracy at the cost of inversion time and computer memory (such as mesh coarseness, number of nodes between adjacent electrodes and frequency of line search computations) were all set to the highest accuracy setting. Table 4.2 summarizes all the inversion parameters used.

Inversions were run for a minimum of seven iterations. Inversion RMS values levelled-out between the sixth and subsequent iterations indicating model convergence. It was decided that the sixth iteration of each inversion would be accepted as the resulting resistivity model. Table 4.3 displays the RMS error associated with the resulting inversion for each acquisition date. Error values exhibited minor increases during the driest subsurface conditions, but were otherwise relatively consistent between acquisition dates. The average RMS error value across all dates and all sites was 0.96%.

4.4 Results and Analysis

4.4.1 Apparent Resistivity Results

Selected pseudosections of acquired resistivity are displayed in Figures 4.2 – 4.6 for Sites 1 – 5, respectively. The complete data set is available in Appendix A. The dates selected display good examples of the variation in resistivity values observed at each monitoring site with changing seasonal conditions over the annual cycle. Winter, wet spring, very-dry late summer and autumn wetting conditions correspond to 28 February 2012, 14 May 2012, 14 August 2012 and 24 September 2012 pseudosections, respectively. The 19 April 2012 and 21 June 2012 pseudosections show mid-spring and mid-summer transitional soil moisture conditions, respectively. At each monitoring site, the least resistive conditions occur during periods of wet subsurface conditions. Overall apparent resistivity is observed to significantly increase during drier conditions and increase to a lesser degree during frozen conditions.

Similar subsurface electrical resistivity trends are observed in the apparent resistivity pseudosections at Sites 1, 3, 4 and 5. During the wetter autumn through spring period, the least resistive measurements are found at the shallowest pseudodepths with increasingly resistive measurements occurring at larger pseudodepths. The exception to this pattern is observed during drier summer conditions (e.g., 14 August 2012) when apparent resistivity measurements are highly resistive at the shallowest pseudodepth. It is less resistive than this surface layer for pseudodepths between 0.5 and 1.0 metres followed by an increase in resistivity at greater pseudodepths. Each of these monitoring sites displays significant lateral variation in apparent resistivity for the upper metre of pseudodepth values. Site 5 is notably more resistive than Sites 1, 3 and 4 throughout all seasonal conditions.

The apparent resistivity values and distribution at Site 2 are distinct from the other monitoring sites. Apparent resistivity values are much higher at Site 2 compared to the other four monitoring sites. At Site 2, the shallowest pseudodepth consistently observes the highest apparent resistivity values throughout the annual cycle with values decreasing with increased pseudodepths. Gradual lateral variation in apparent resistivity that persist throughout all seasonal conditions are present at Site 2 for the shallow pseudodepths.

4.4.2 Inverted Resistivity Results

4.4.2.1 Inversion Tomograms

Selected ERT inversion tomograms are displayed in Figures 4.7 – 4.11 for Sites 1 – 5, respectively. The dates selected are the same as those chosen for Figures 4.2 – 4.6. Complete inversion results for all acquisition dates at all sites are available in Appendix A.

The inversion results displayed by the tomograms from Sites 1, 3, 4 and 5 can be viewed as a two-layer over a half-space model. The shallowest layer exists from the ground surface to an approximate depth of 0.25 m. Dry summer and frozen winter periods produce higher resistivity conditions, whereas lower resistivity values for this layer are found during the wet spring and autumn conditions.

The second layer can be seen in the tomograms at Sites 1, 3, 4 and 5 located approximately between 0.25 and 1.50 metres depth below the ground surface. In general, this layer is less resistive than the overlaying shallow layer with significant contrast between the two layers notable during dry subsurface conditions. During wet conditions, only minor contrast may exist between this layer and the shallow layer.

The half-space layer is visible in each of Site 1, 3, 4 and 5’s inversion tomograms at depths below approximately 1.50 metres. The half-spaces at these monitoring sites are consistently more resistive than the second layer. During wet seasonal conditions the half-space layer is observed to be the most resistive of the three layers present in the inversions.

Notably different tomograms are obtained at Site 2 compared to the other monitoring sites. Firstly, the resistivity values of the inversion model for Site 2 are much larger than those obtained at the other monitoring sites. Secondly, these tomograms can be viewed as a single layer overlaying the half-space layer. As noted in Section 3.2, Site 2 is located on the side of a knoll and there is a gentle downward slope along the profile line with the highest point of elevation at the 0-metre mark. The sloped nature of the shallow layer may be explained as a minor distortion due the data not being corrected for the minor slope. The half-space layer at Site 2 is encountered at an approximate depth of 1.25 metres. Unlike the half-space at other monitoring sites, the half-space at Site 2 is more conductive than its overlaying material.

The larger resistivity values at Site 2 compared to the other monitoring sites are consistent with the coarser-grained soils present at Site 2. Table 3.2 indicates that the clayey component of the subsurface at Site 2 is much smaller than at the other four monitoring sites. The presence of less clay could increase electrical resistance of the subsurface material due to a lower contribution by the interfacial conduction (discussed in Section 2.1).

4.4.2.2 Inversion Time-Profile Slices

Figures 4.12 – 4.16 are time-profile slices for each of the five monitoring sites at four depths selected from the tomograms. These figures depict inverted resistivity values for specific model depths for all acquisition dates (along the x-axis) and at all profile positions (along the y-axis). It is evident in the inversion tomograms and these time-profile slices that the lateral variability of the resistivity observed in the shallow subsurface at each of the monitoring sites contains a regularly-spaced pattern of increasing and decreasing resistivity along the length of the survey profiles (i.e., horizontal striping on these figures). This cyclic component is stronger at the shallow three depths displayed in the time-profile slices. Subdued cyclicity is observable in the 0.82 m time-profile slices.

Fast Fourier Transform (FFT) analysis was performed on profile resistivity data at the depth of 0.33 metres to determine the variation in the frequency of cyclic components in data between monitoring sites and acquisition dates. This depth was chosen because of the strong cyclic nature in the resistivity distribution observed in the time-profile slice for the depth without the overprinting of the highly dynamic resistivity variations occurring at shallower depths. Prior to performing the FFT computation, a 5th-order best-fit polynomial was removed from each data profile. The removal of the 5th-order trend across the profile enhanced the residual cyclic signature by minimizing the response of the DC and low-frequency components in the resulting amplitude spectra. FFT computation was performed on the residual profile using the Excel 2010 Analysis ToolPak, (Microsoft; Redmond, USA). Data was zero-padded for a total of 4096 data points to create a highly discretized frequency spectrum.

The FFT results are displayed in Figures 4.17 – 4.21 for Sites 1 – 5, respectively. Results vary by monitoring site. Analysis of the amplitude spectra at Site 3 (Figure 4.19) shows a well-defined and re-occurring frequency component at 0.4 m^{-1} (spatial wavelength of 2.5 m). This distinct maximum at this frequency exists through all data sets except 15 September 2010, 18 July 2011 to 02 August 2011 and 09 July 2012 to 04 September 2012. These dates correspond to high-resistivity summer conditions. Visual inspection of the tomograms and time-profile slices for these dates display a weaker cyclic nature than during the other seasonal periods.

Similar FFT results were obtained at Sites 4 (Figure 4.20) and 5 (Figure 4.21) with a somewhat diminished 0.4 m^{-1} component at Site 5. Resulting FFT amplitude spectra for Sites 1 (Figure 4.17) and 2 (Figure 4.18) are notably different. The frequency spectrum for Site 1 displays a cyclic component at 0.35 m^{-1} (spatial wavelength of 2.9 m). It is of small amplitude compared to what is observed at Sites 3 – 5; however, it follows a similar progression in magnitude throughout seasonal conditions. Site 2 does not exhibit any one dominant cyclic frequency component.

4.4.3 Mean Resistivity Depth Profiles

To more clearly show the temporal evolution of the subsurface resistivity structure obtained from the inversion results, a mean resistivity depth profile for each data set was generated. These depth profiles were produced by averaging the resistivity values at each depth level in the inversion model to obtain a mean value for the depth in the resulting profile. This averaging process uses values over the lateral interval between 9.00 and 15.00 metres along the survey line as this portion of the inversion model possesses values for all depth levels. These average resistivity depth profile are presented as time series for the complete two year monitoring period in Figures 4.22 for Sites 1, 3, 4 and 5 and Figure 4.23 for Site 2.

The two-layer over a half-space scenario at Sites 1, 3, 4 and 5 described in the previous section is also evident in the mean results. It can be observed from the fluctuations in resistivity visible in

Figure 4.22 that the mean values from the shallowest layer possess the greatest variation in resistivity values over the annual cycles monitored. It can clearly be seen that more resistivity values occur during the dry summer and frozen winter periods while less resistive conditions happen during the wetter spring and autumn seasons. As observed from the tomograms, the second layer is generally less resistive than the upper layer with its resistivity values varying over a narrower range compared to the shallow layer. The underlying half-space layer is the least dynamic over the course of the two annual cycles and is more resistive than the second layer.

Likewise, the mean resistivity depth profiles of Site 2 (Figure 4.18) agree with the individual tomogram observations of a single layer over a half-space. The half-space layer is consistently less resistive than the overlying material. Over the course of the two-year acquisition period the single layer experiences much greater fluctuations in resistivity than the half-space layer.

4.4.4 Temporal Resistivity Variations

As discussed in Section 2.1, the electrical resistivity of a subsurface is dependent on subsurface geological composition, temperature and moisture content. Over the course of the two-year monitoring period the only subsurface parameters influencing electrical resistivity that change at the monitoring sites are temperature and moisture content. This section examines the relationships between resistivity values obtained from the inversion process and these other temporally-varying parameters.

Figures 4.24 – 4.28 are summary figures displaying the mean resistivity depth profiles alongside precipitation, air temperature, historical soil temperature and volumetric soil moisture content data for Sites 1 – 5, respectively. Qualitative temporal relationships between these parameters at each monitoring site can be observed from Figures 4.24 – 4.28. Volumetric moisture content increases with increased precipitation and mean resistivity values in the upper metre are lowest during periods of high volumetric moisture content. Temporal variations in mean resistivity below 2 metres appear to be responding to soil temperature variations at that depth.

It can be observed from the two annual cycles of data displayed in Figure 4.24 – 4.28 that the differences in geophysical response during matching seasons of the two years conforms with the documented annual variation in precipitation and temperature (Section 3.3). The drier and warmer conditions experienced in 2012 are most notable in the summer and winter resistivity data sets. Significantly higher resistivity conditions are experienced in the upper 0.5 metres at all monitoring sites during the drier 2012 summer. At monitoring sites with data for two winter periods (Sites 1, 2 and 3) it can be observed that more resistive conditions occur during the 2010 – 2011 winter period when more days below freezing were experienced than the following winter

4.4.4.1 Dependence between Resistivity and Temperature

To quantitatively examine the potential relationship between subsurface temperature fluctuations and inverted resistivity results, the Pearson product-moment correlation coefficient r was calculated between historic soil temperature data (Table 3.3) and the resistivity value for each layer of the mean resistivity depth profile. The Pearson r provides a quantification of the linear dependence of two parameters with results ranging from -1, meaning a completely negative linear dependence of the variables, to 1, meaning a completely positive linear dependence, with 0 meaning no linear dependence is present. If resistivity values were being driven primarily by temperature fluctuations, then a linear relationship of decreasing resistivity with increasing temperature would exist (Campbell et al., 1948) as represented by an r-value close to -1.

The results of the r calculation for each model depth level at every monitoring site are displayed in Figure 4.29. At depths associated with the shallowest layer (upper 0.25 metres) at all monitoring sites, the major observation is a small, positive r-value indicating what resistivity fluctuation is present operates opposite of what is expected for temperature dependence. At this depth, the r-values calculated support the hypothesis in Section 2.1 that observed resistivity variations are primarily driven by variations in moisture content due to its range of fluctuation compared to that of subsurface temperature. Figure 4.29 shows that r-values evolve differently below the surface layer at the various monitoring sites. At Sites 2, 3 and 5 the r-values progressively change to large, negative values with increasing depth. The relatively consistent r-values found at depth at these sites indicate that temperature variations have become the primary variable driving resistivity in the underlying half-space layer.

At Sites 1 and 4, the relationship between r and depth is more complex. Like the other sites, these two sites show a small and positive r-value between temperature and model resistivity in the surface layer. At Site 1, r-values stop growing increasingly negative at a depth of 1.2 metres and gradually decrease in magnitude with increasing depth. At Site 4, r-value magnitude plateaus between 0.5 and 1.0 metres before quickly decreasing and subsequently increasing while remaining negative. At this point, there is no explanation for the deeper r-value results at Sites 1 and 4.

4.4.4.2 Dependence between Resistivity and Moisture Content

How well resistivity variations observed in inversion results track moisture variations in the subsurface can be investigated by comparing mean resistivity data to the gravimetrically-acquired volumetric moisture content data (Figure 3.7).

As stated in Section 2.1, Calamita et al. (2012) have summarized the mathematical relationships between electrical resistivity and subsurface moisture content used in past studies. These studies have predominantly used a power law relationship between the two parameters for studies with wide-ranging moisture contents in various geological settings (Calamita et al., 2012).

The data from this thesis was examined using log-log cross-plots with a regression based on the commonly used power-type relationship. The results from cross-plotting these parameters are displayed in Figures 4.30 – 4.34. Each figure contains three panels that display the results from using data from three different subsurface intervals. Panel A compares volumetric moisture content data collected from the 0 – 0.25 metre interval with mean resistivity values averaged for model blocks within the same interval for the corresponding acquisition date. Similarly, Panel B compares data from the 0.25 – 0.50 metre interval. Panel C compares averaged volumetric moisture content data for the entire 0 – 0.50 metre interval with mean resistivity values averaged for model blocks within the upper 0.50 metres.

The data from Sites 1, 3, 4 and 5 do not conform well to the expected power-type relationship. R^2-values for the study intervals at Sites 1, 3, 4 and 5 range from 0.0360 to 0.6259. At each of these four monitoring sites, the R^2-values are larger for the 0 – 0.25 m interval (R^2 range: 0.2672 and 0.6259) than the 0.25 – 0.50 m interval (R^2 range: 0.0360 to 0.4370). A power-type relationship is visible within the data at Site 2. The R^2-value is largest for data limited to the 0.25 – 0.50 metre interval (0.6306) compared to the shallower interval (0.5854). Site 2 is coarser-grained than the other four monitoring sites (Table 3.3). The appearance of a power-type relationship at Site 2 may be due to the smaller clay component that exists at the site since less clay present means the subsurface conforms better to the assumptions of Archie’s Equation.

4.5 Conclusions

Temporal variations in the inversion tomograms and the associated mean resistivity depth profiles show very good qualitative agreement with the soil moisture conditions in the upper 0.25 – 0.50 metres inferred from the gravimetric sampling and weather data. In particular, lower resistivity values occurred in this region during wet spring and fall conditions while higher resistivity values were found during the dry summer and frozen winter periods. Differences in moisture conditions between contrasting annual cycles are also reflected in the ERT data. The drier, warmer summer of 2012 produced much higher resistivity values than the corresponding summer of 2011. In addition, more resistive conditions occurred during the colder 2010 – 2011 winter in comparison to the milder 2011 – 2012 winter season.

In contrast to these findings, the relatively low correlation coefficient values obtained from the analysis performed in this study indicate that more work is needed to better understand the quantitative nature of the relationship between the resistivity values obtained from the inversion of ERT data and soil moisture content derived from gravimetric sampling. While Archie's equation has been widely applied to many soil textures including some with appreciable clay content, its validity in this case is questionable. Also, the resistivity values have an uncertainty range due to the nature of the inversion process (e.g., non-uniqueness) and resistivity measurement (e.g., sampling volume and sensitivity function of the electrode array). Further, the decision to neglect a compensation for temperature effects could have impacted the results.

Temporal variations in the ERT results for the subsurface below 1 metre depth appear to be qualitatively consistent with seasonal pattern of the historical subsurface temperature data. The correlation coefficient values from another analysis performed in this study on the relationship between the resistivity values obtained from the inversion of ERT data and historic soil temperature information provide good support for this observation. However, there were some anomalous results in this analysis at two of the sites that require further study.

A particular feature of ERT data was the occurrence of a cyclic component in the lateral variation of resistivity values along the survey lines with a spatial wavelength of 2.50 metres at Sites 3, 4 and 5. The amplitude of this cyclic component appears to be a function of soil moisture conditions with the higher amplitude occurring during wet soil periods and becoming significantly smaller during dry period. Potential sources of this cyclic component will be discussed in Chapter 6.

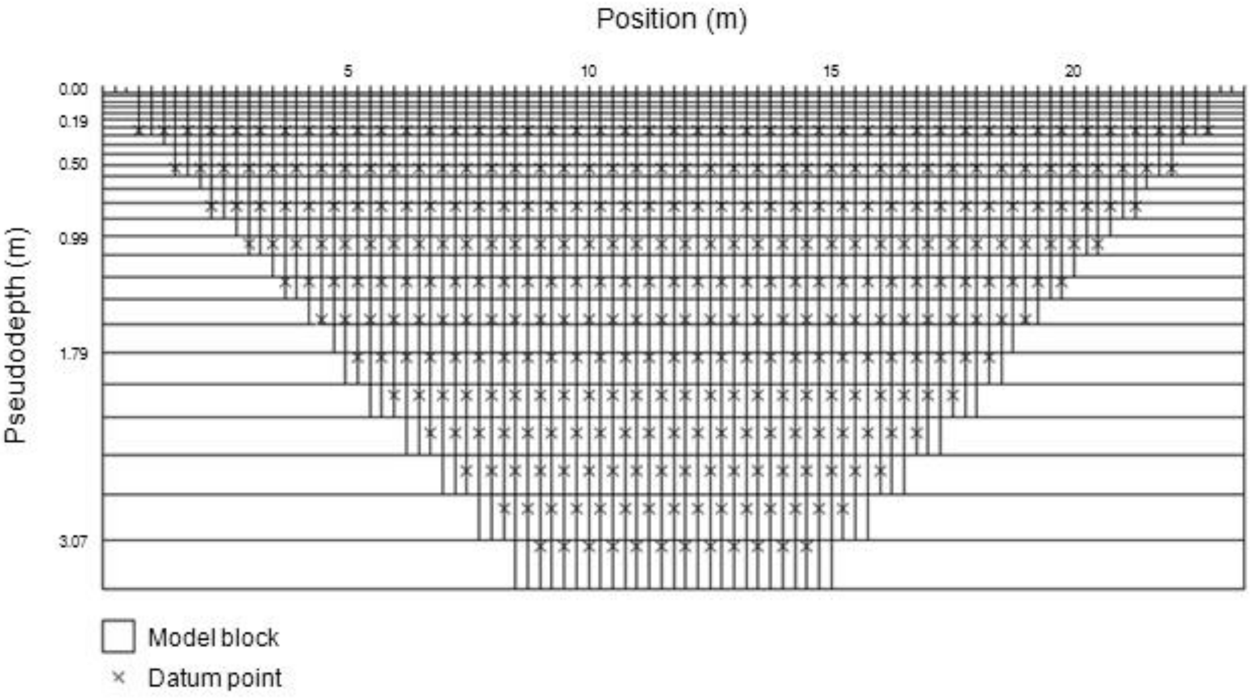

Figure 4.1 – Diagram showing the inferred relationship between inversion model blocks and data points.

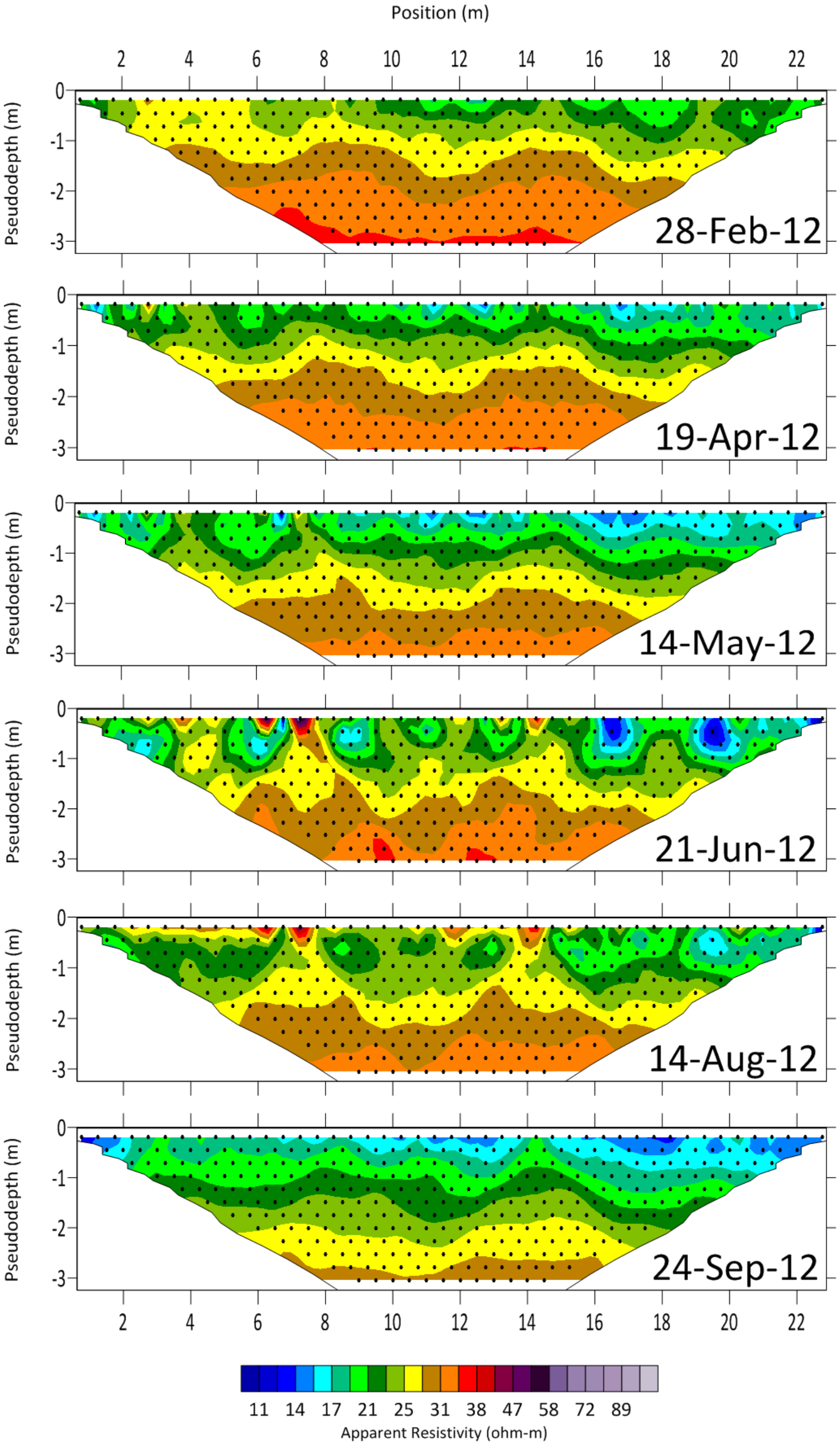

Figure 4.2 – Selected pseudosections from Site 1 displaying the seasonal variability in the acquired subsurface resistivity. A complete collection of pseudosections for Site 1 are available in Appendix A. Black dots represent the position associated with each data point within the pseudosection.

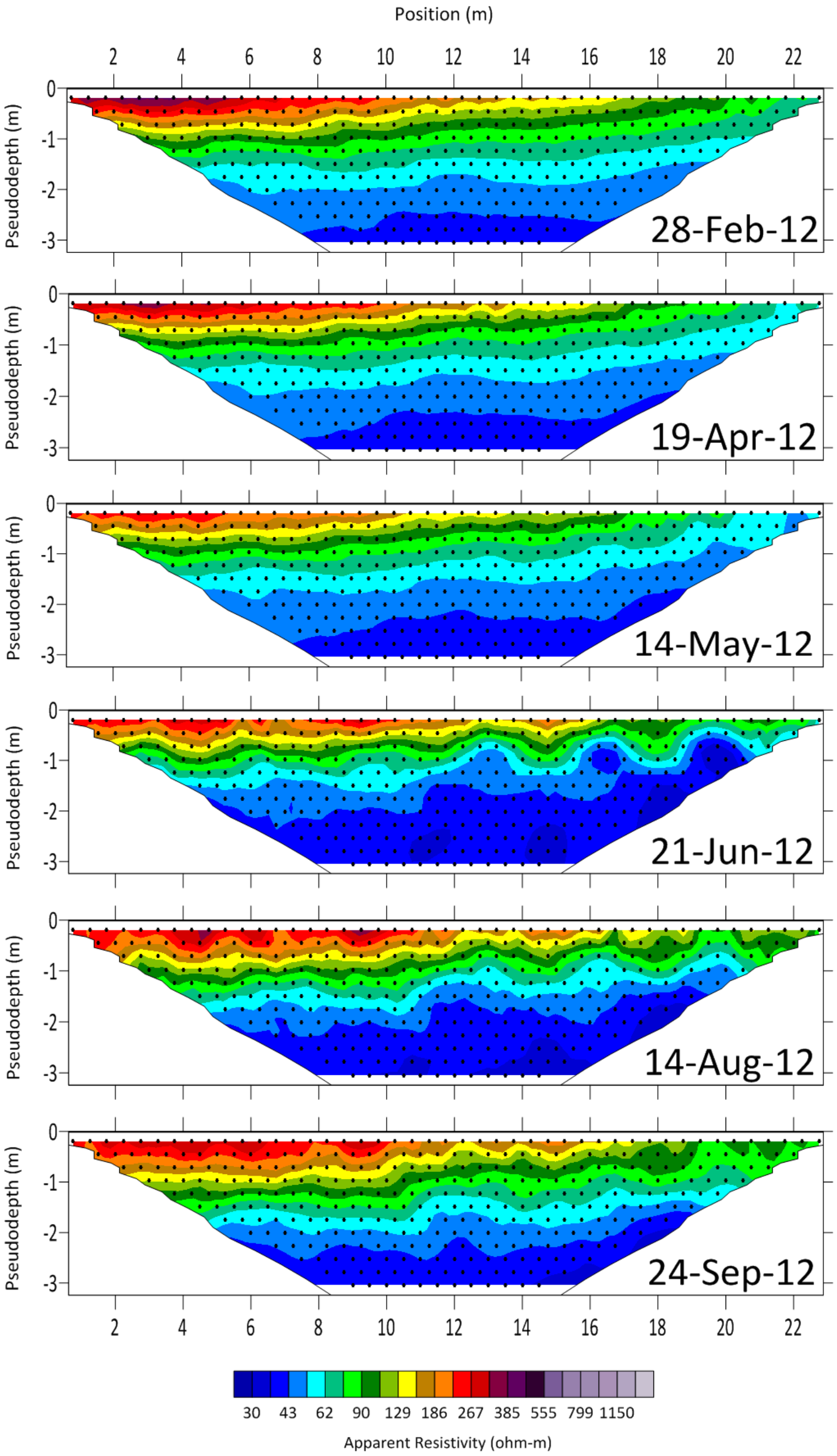

Figure 4.3 – Selected pseudosections from Site 2 displaying the seasonal variability in the acquired subsurface resistivity. A complete collection of pseudosections for Site 2 are available in Appendix A. Black dots represent the position associated with each data point within the pseudosection.

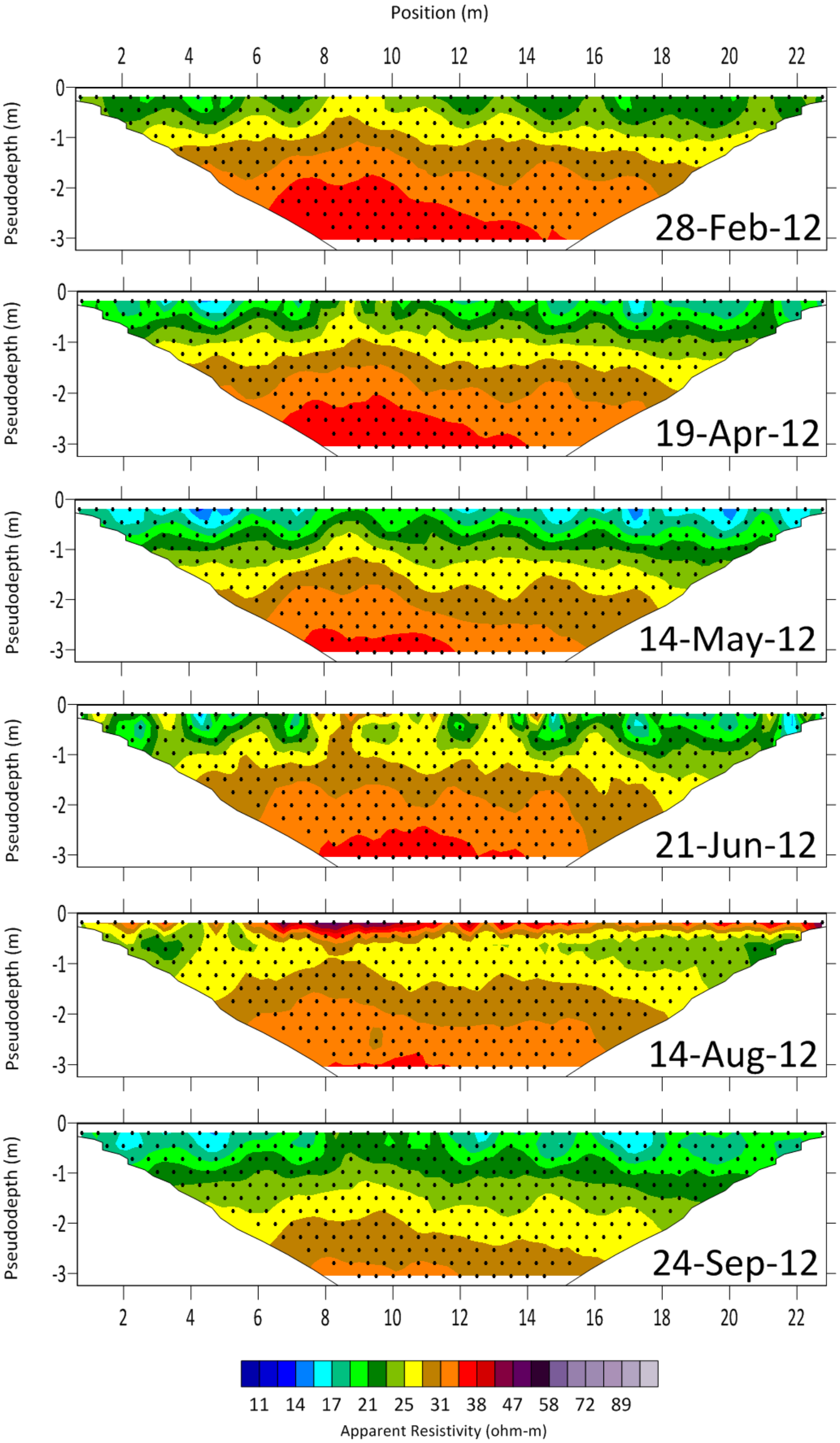

Figure 4.4 – Selected pseudosections from Site 3 displaying the seasonal variability in the acquired subsurface resistivity. A complete collection of pseudosections for Site 3 are available in Appendix A. Black dots represent the position associated with each data point within the pseudosection.

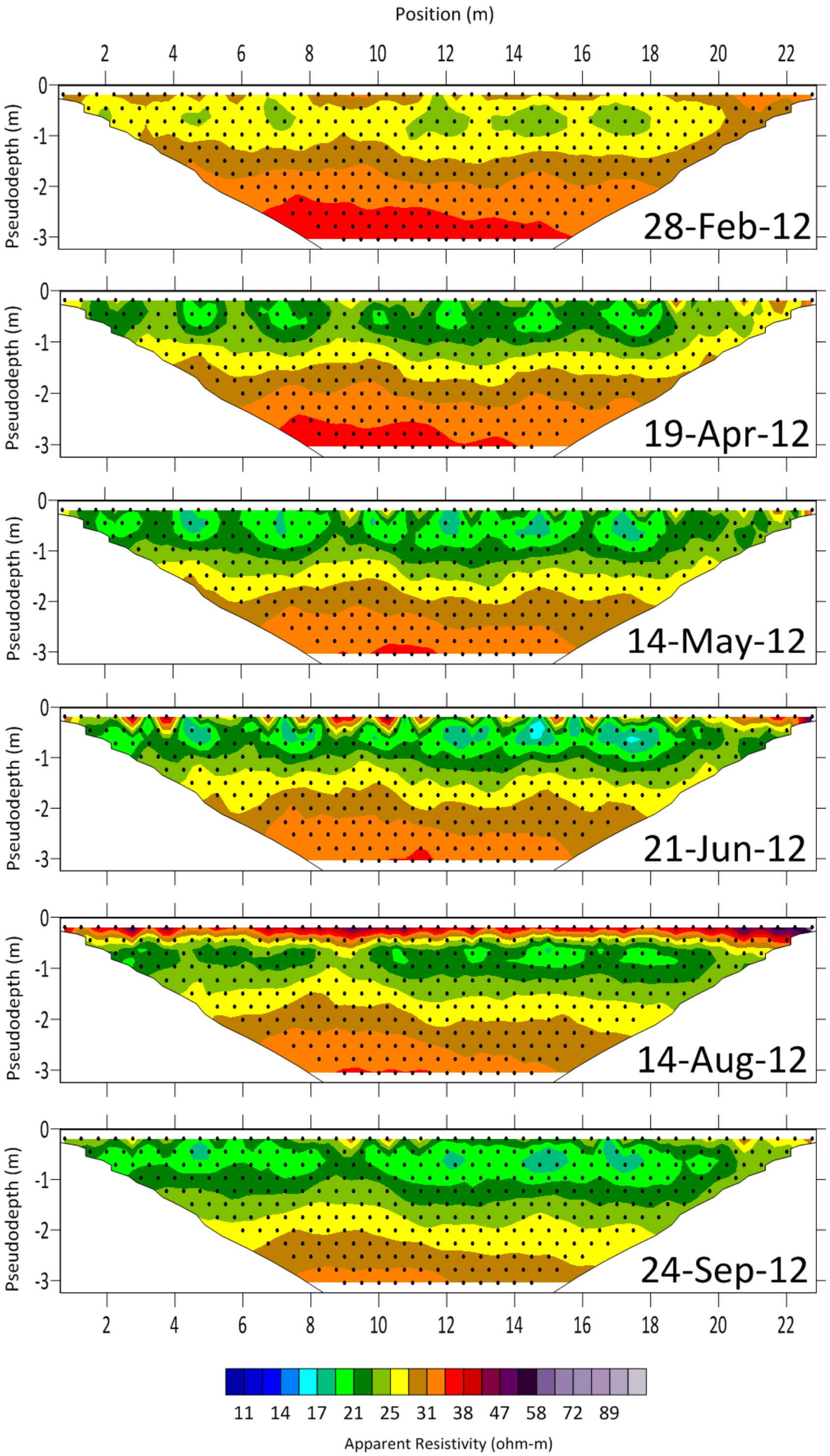

Figure 4.5 – Selected pseudosections from Site 4 displaying the seasonal variability in the acquired subsurface resistivity. A complete collection of pseudosections for Site 4 are available in Appendix A. Black dots represent the position associated with each data point within the pseudosection.

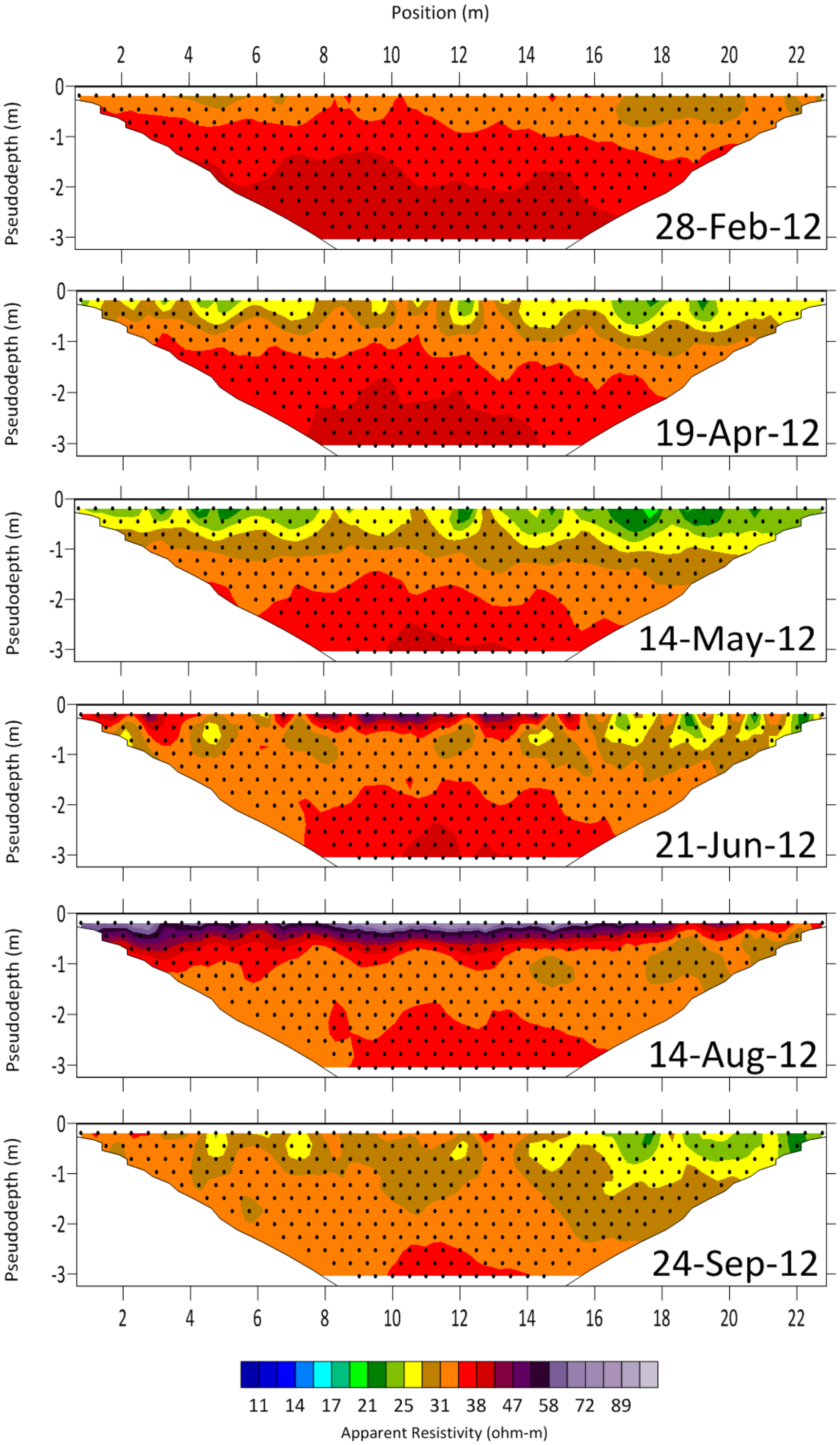

Figure 4.6 – Selected pseudosections from Site 5 displaying the seasonal variability in the acquired subsurface resistivity. A complete collection of pseudosections for Site 5 are available in Appendix A. Black dots represent the position associated with each data point within the pseudosection.

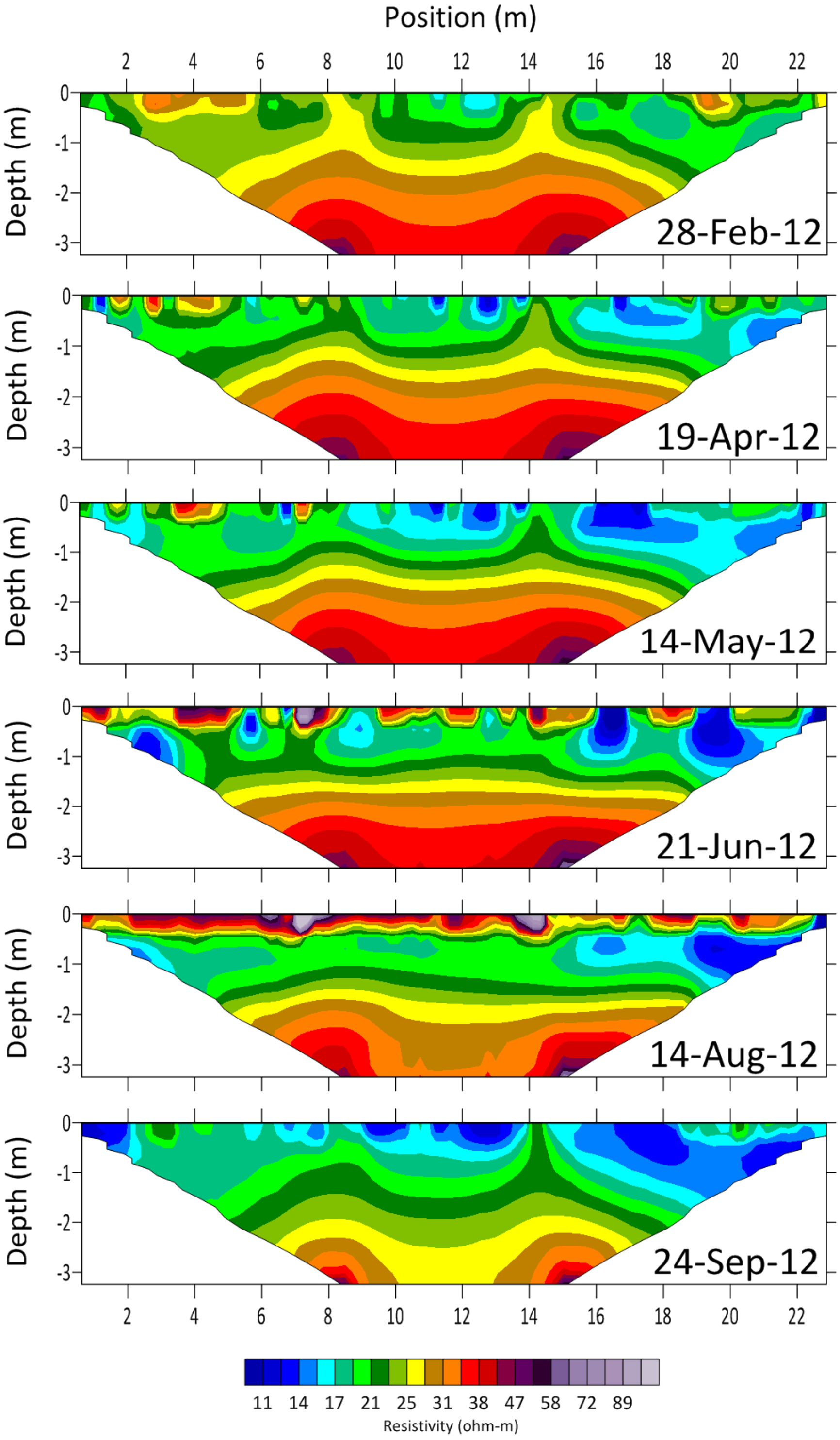

Figure 4.7 – Selected tomograms from Site 1 to display seasonal variability of subsurface resistivity obtained from the inversion results. A complete collection of inversion tomograms for Site 1 are available in Appendix A.

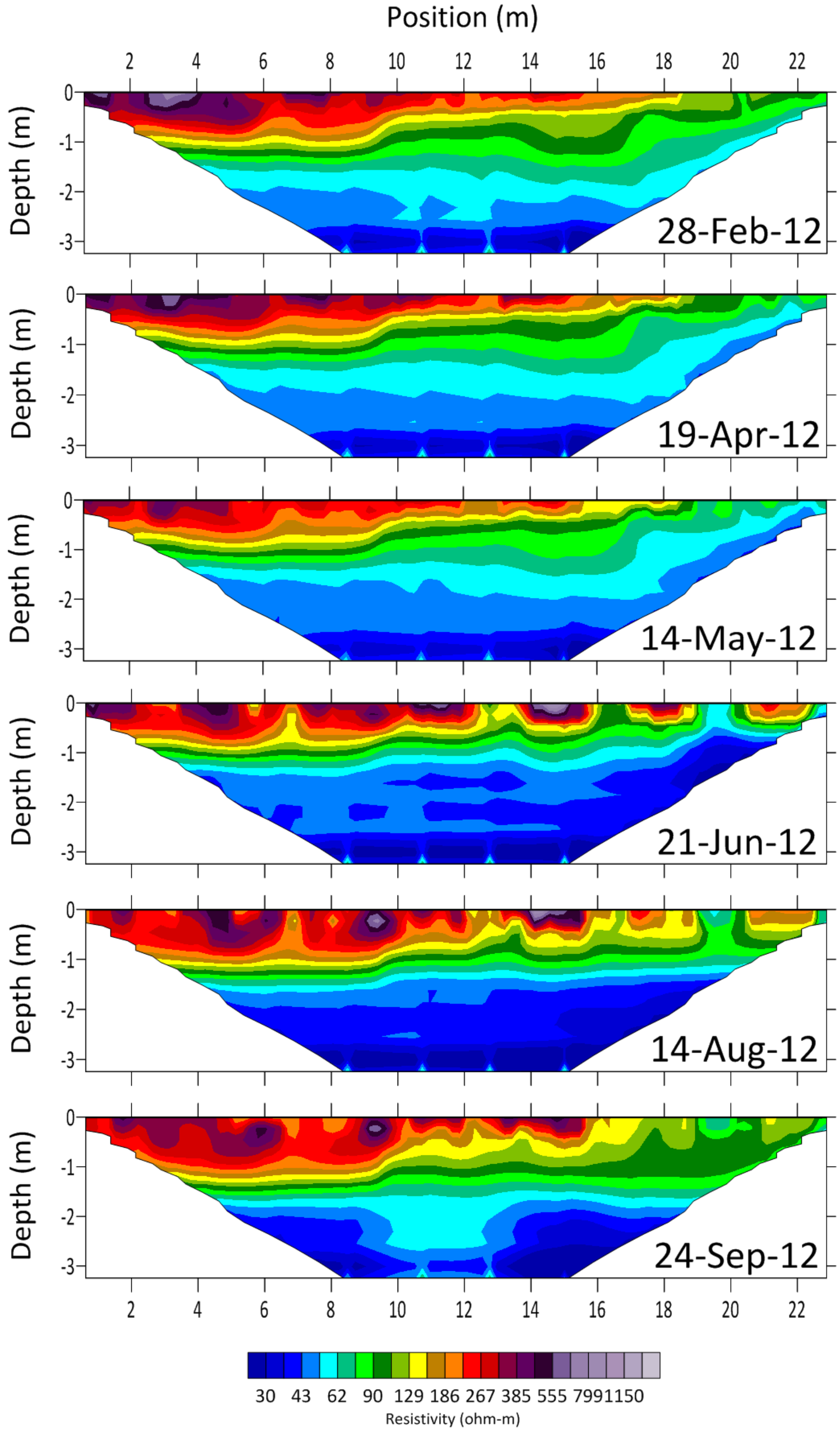

Figure 4.8 – Selected tomograms from Site 2 to display seasonal variability of subsurface resistivity obtained from the inversion results. A complete collection of inversion tomograms for Site 2 are available in Appendix A.

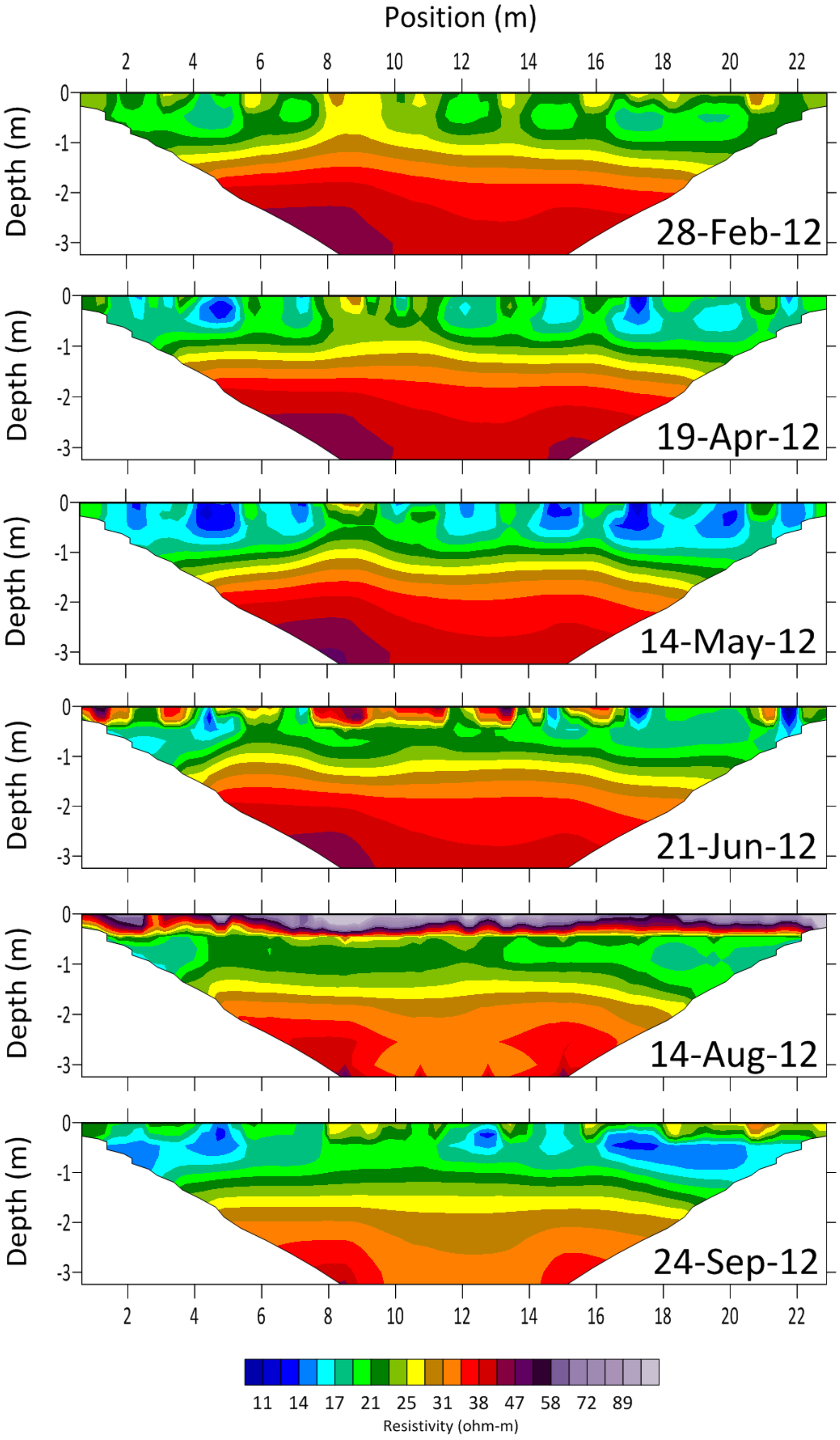

Figure 4.9 – Selected tomograms from Site 3 to display seasonal variability of subsurface resistivity obtained from the inversion results. A complete collection of inversion tomograms for Site 3 are available in Appendix A.

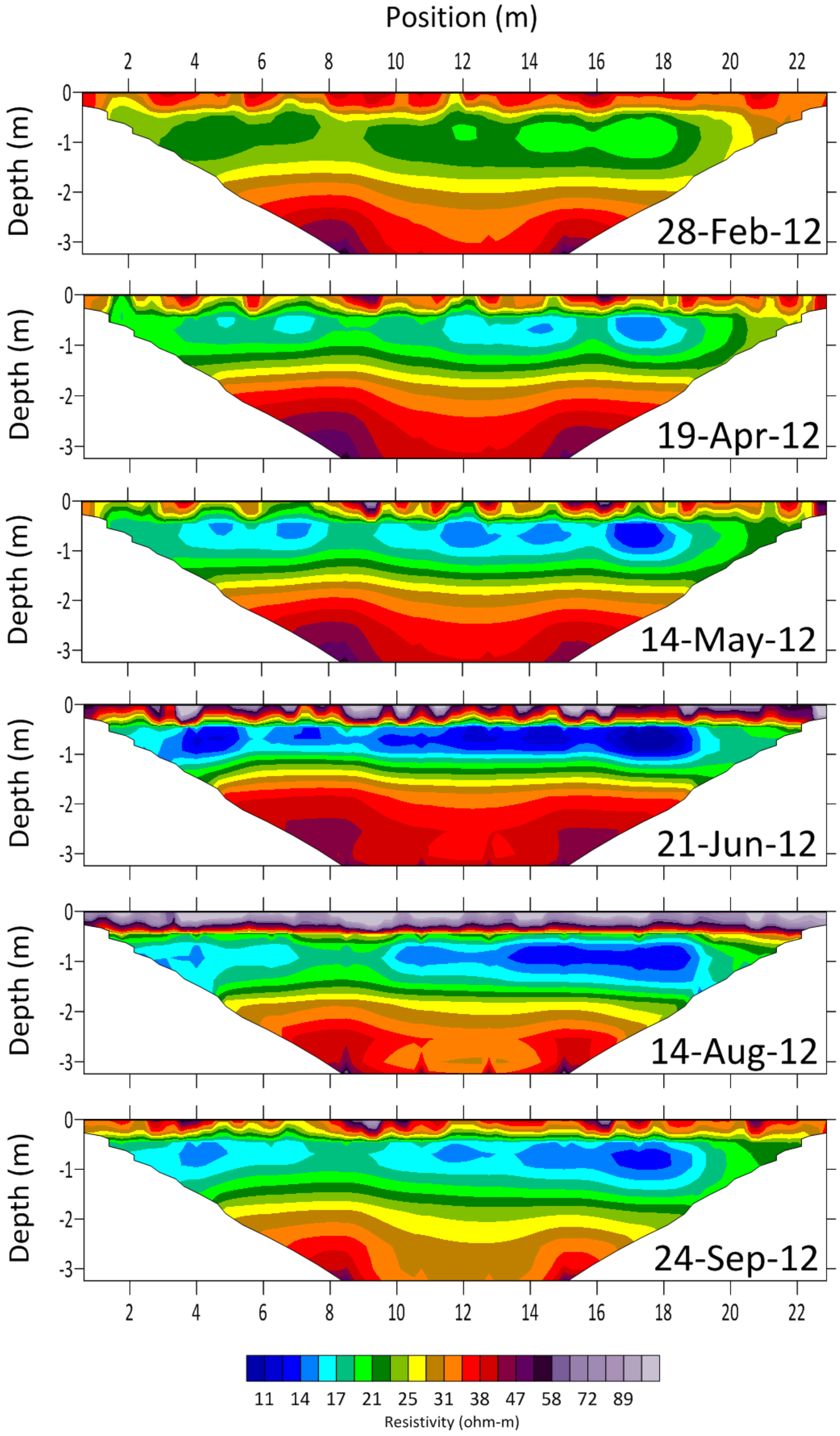

Figure 4.10 – Selected tomograms from Site 4 to display seasonal variability of subsurface resistivity obtained from the inversion results. A complete collection of inversion tomograms for Site 4 are available in Appendix A.

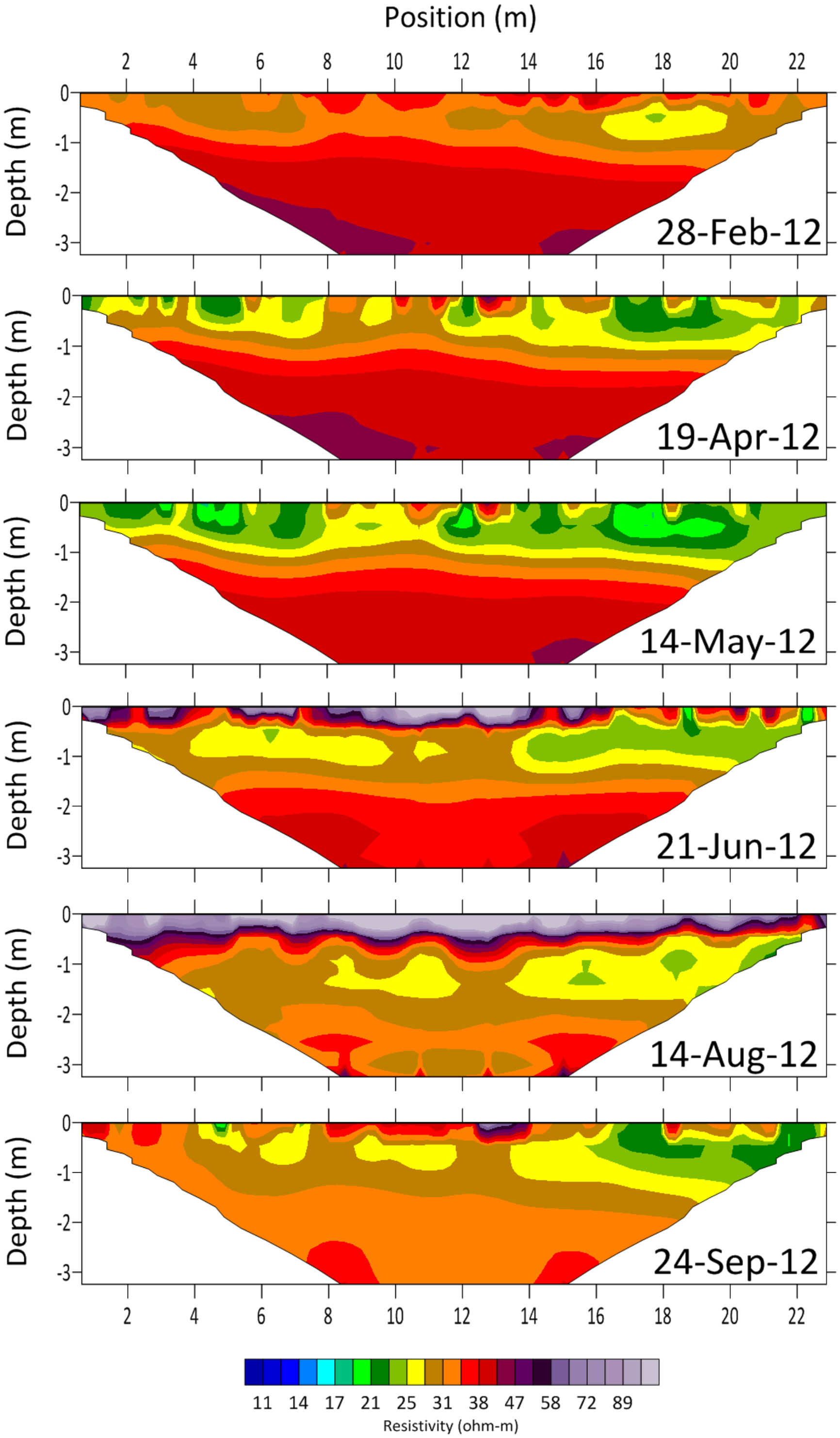

Figure 4.11 – Selected tomograms from Site 5 to display seasonal variability of subsurface resistivity obtained from the inversion results. A complete collection of inversion tomograms for Site 5 are available in Appendix A.

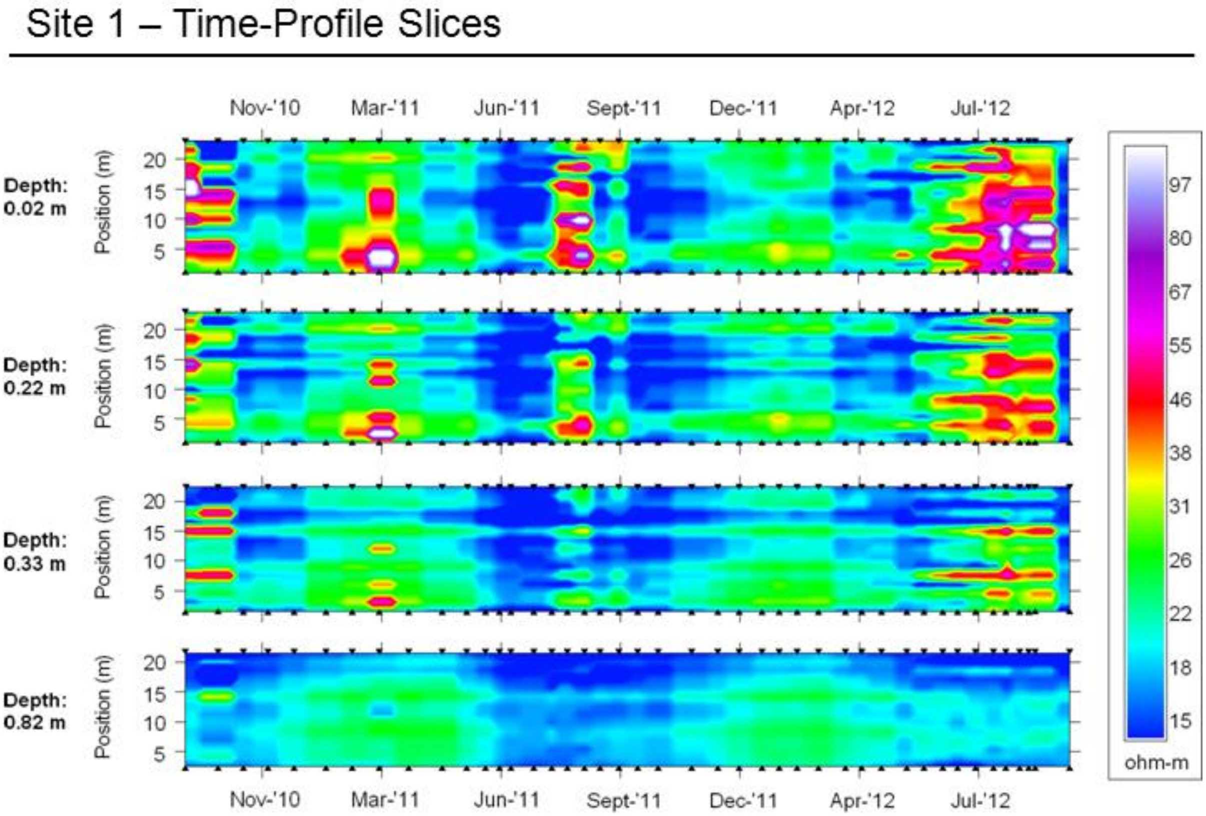

Figure 4.12 – ERT inversion time-profile slices for four depths at Site 1. The cyclic nature of the spatial resistivity distribution across the profile is strongly evident in the shallower slices (i.e., horizontal striping). The black triangles represent the location of acquisition dates along the time-axis.

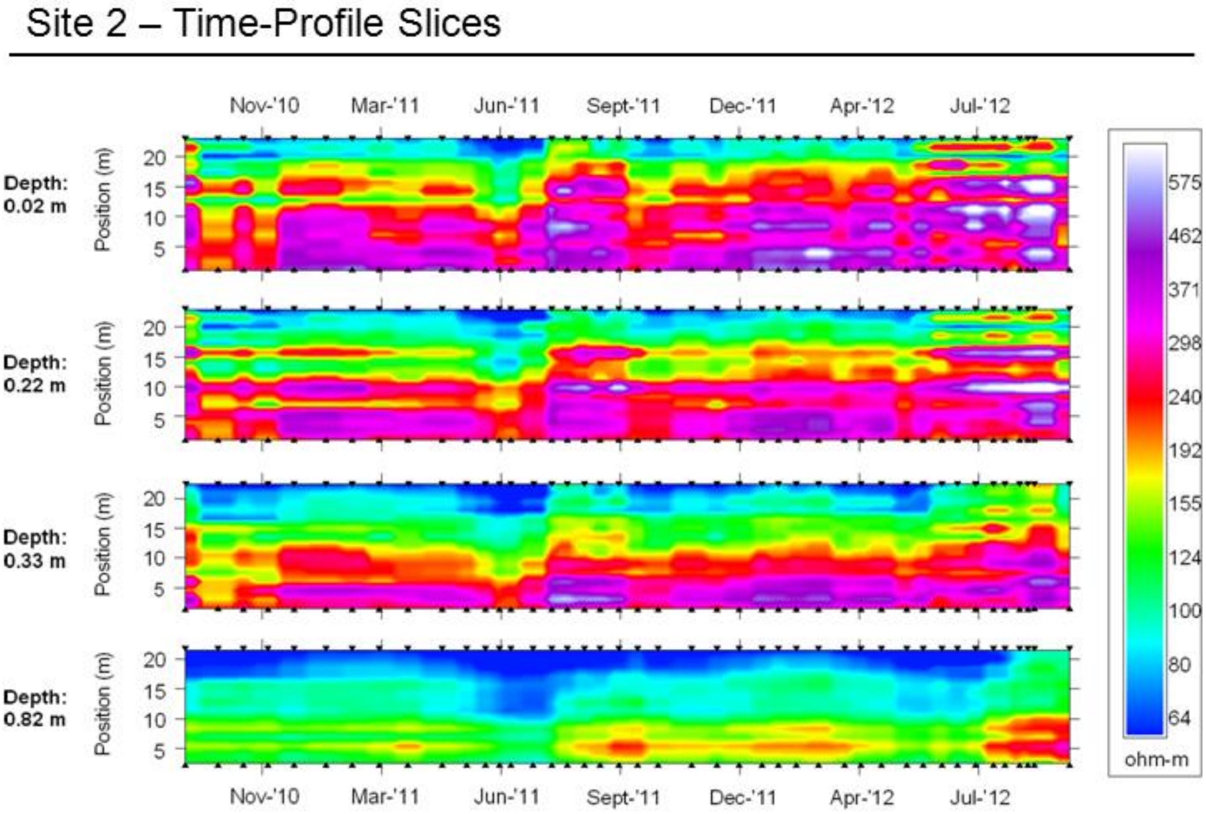

Figure 4.13 – ERT inversion time-profile slices for four depths at Site 2. The cyclic nature of the spatial resistivity distribution across the profile is strongly evident in the shallower slices (i.e., horizontal striping). The black triangles represent the location of acquisition dates along the time-axis.

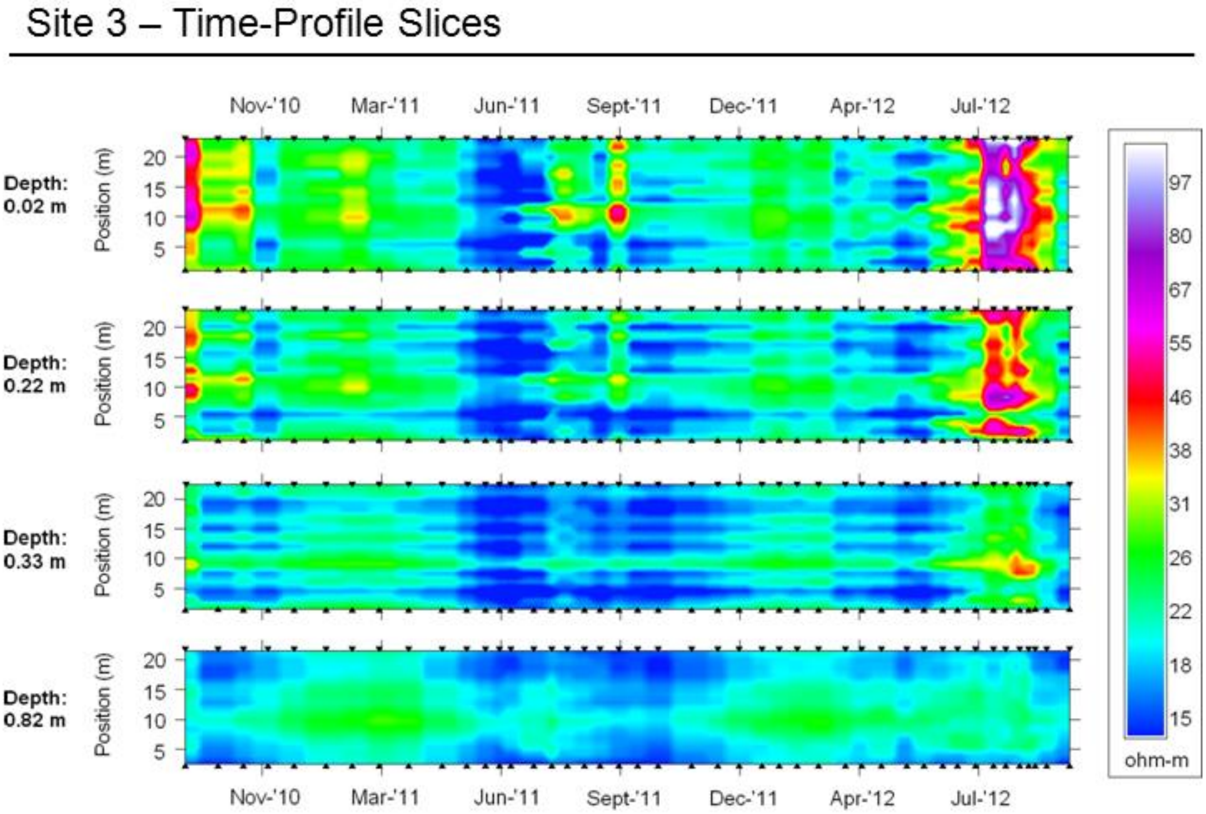

Figure 4.14 – ERT inversion time-profile slices for four depths at Site 3. The cyclic nature of the spatial resistivity distribution across the profile is strongly evident in the shallower slices (i.e., horizontal striping). The black triangles represent the location of acquisition dates along the time-axis.

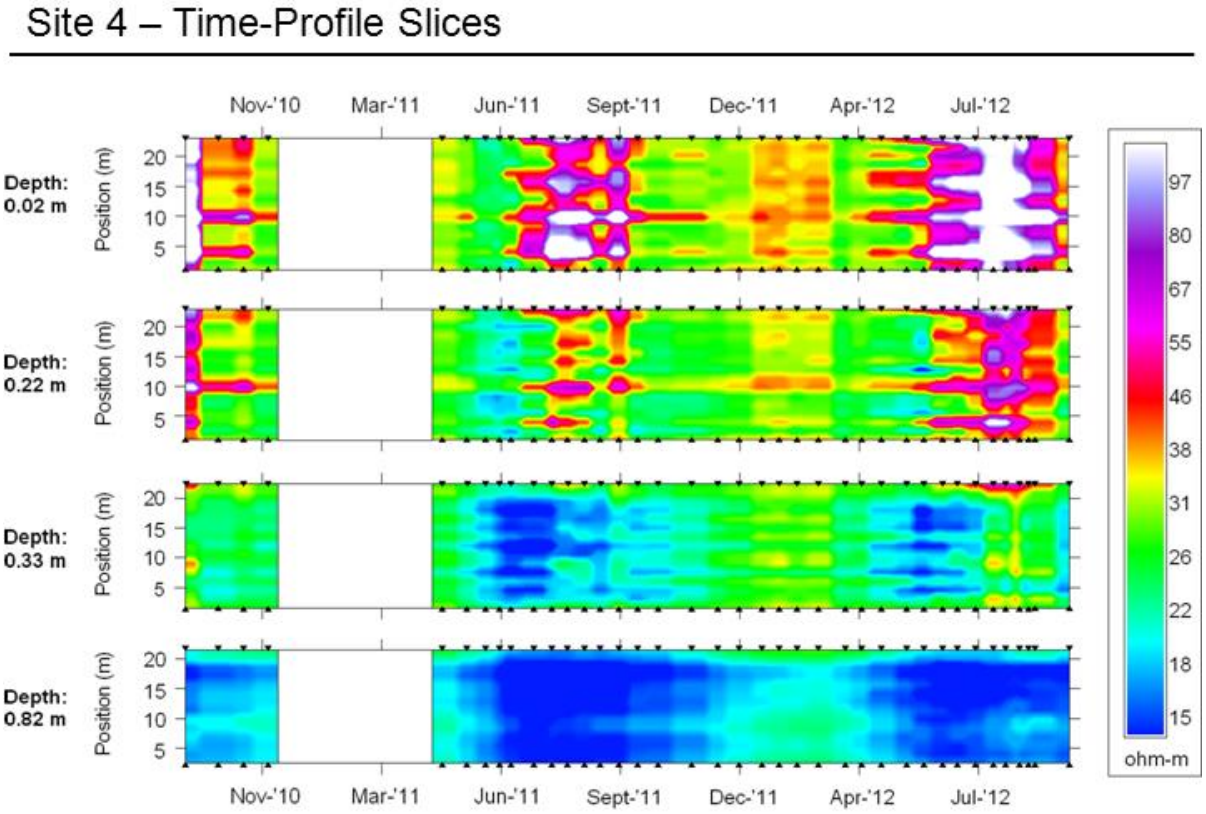

Figure 4.15 – ERT inversion time-profile slices for four depths at Site 4. The cyclic nature of the spatial resistivity distribution across the profile is strongly evident in the shallower slices (i.e., horizontal striping). The black triangles represent the location of acquisition dates along the time-axis. Gaps in data during the winter of 2010 – 2011 are due to periods with no data collection.

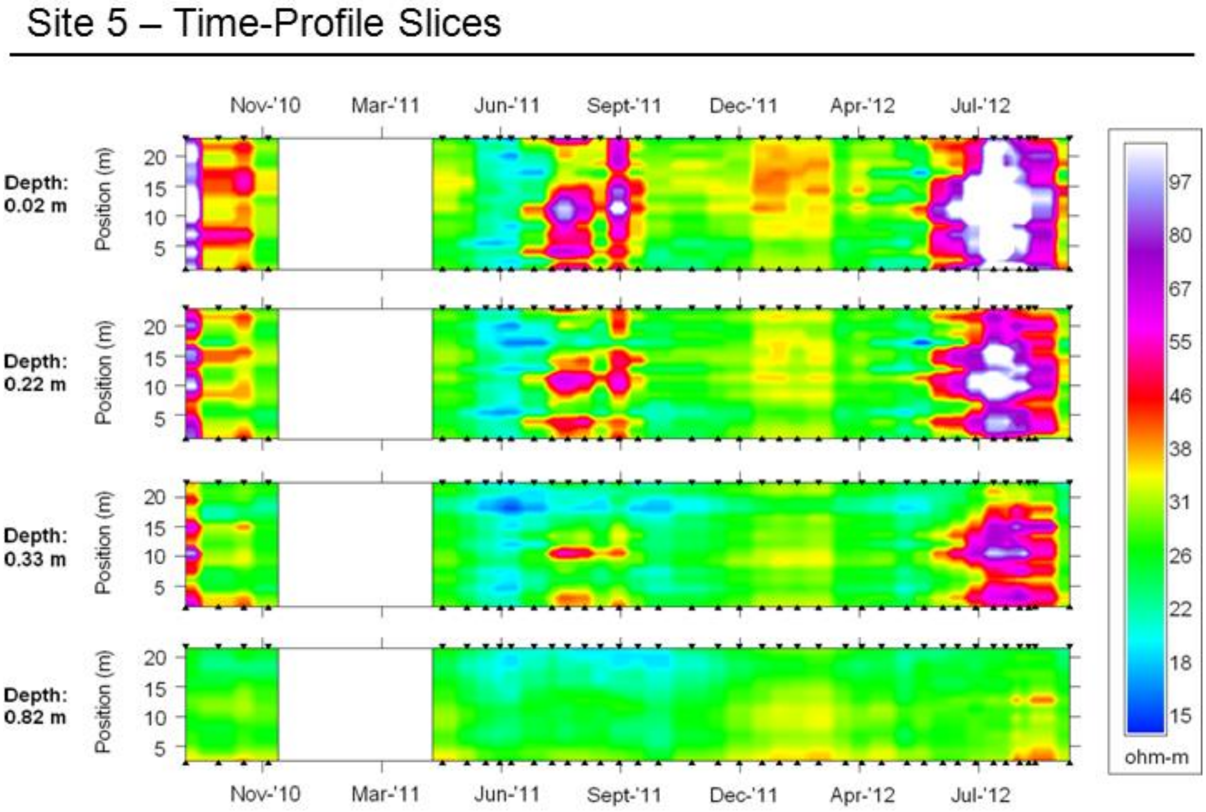

Figure 4.16 – ERT inversion time-profile slices for four depths at Site 5. The cyclic nature of the spatial resistivity distribution across the profile is strongly evident in the shallower slices (i.e., horizontal striping). The black triangles represent the location of acquisition dates along the time-axis. Gaps in data during the winter of 2010 – 2011 are due to periods with no data collection.

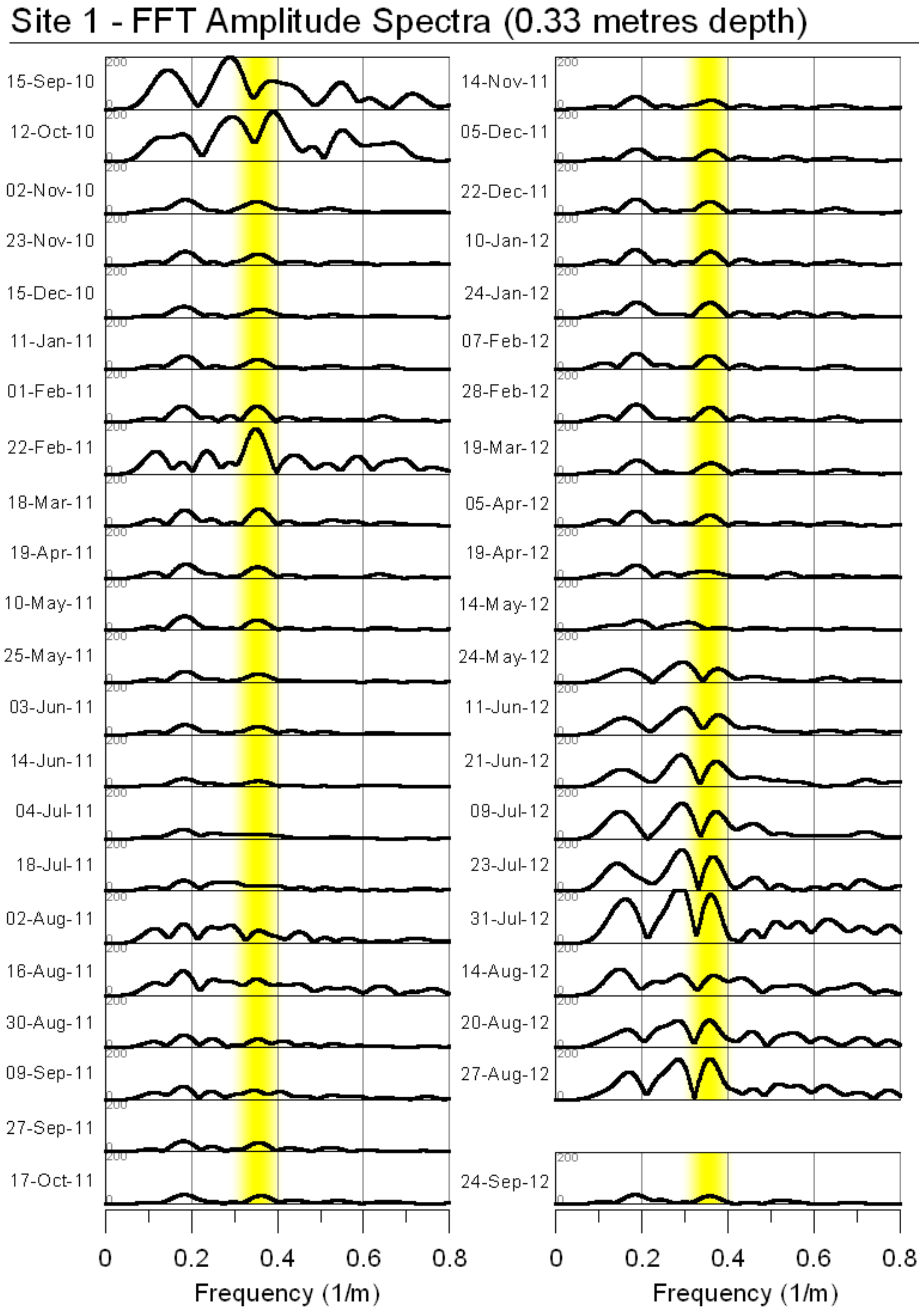

Figure 4.17 – FFT amplitude spectra for ERT inversion profile data at 0.33 metres depth at Site 1. The yellow highlights the 0.35 m^{-1} frequency component. Data gaps indicate period of no data collection.

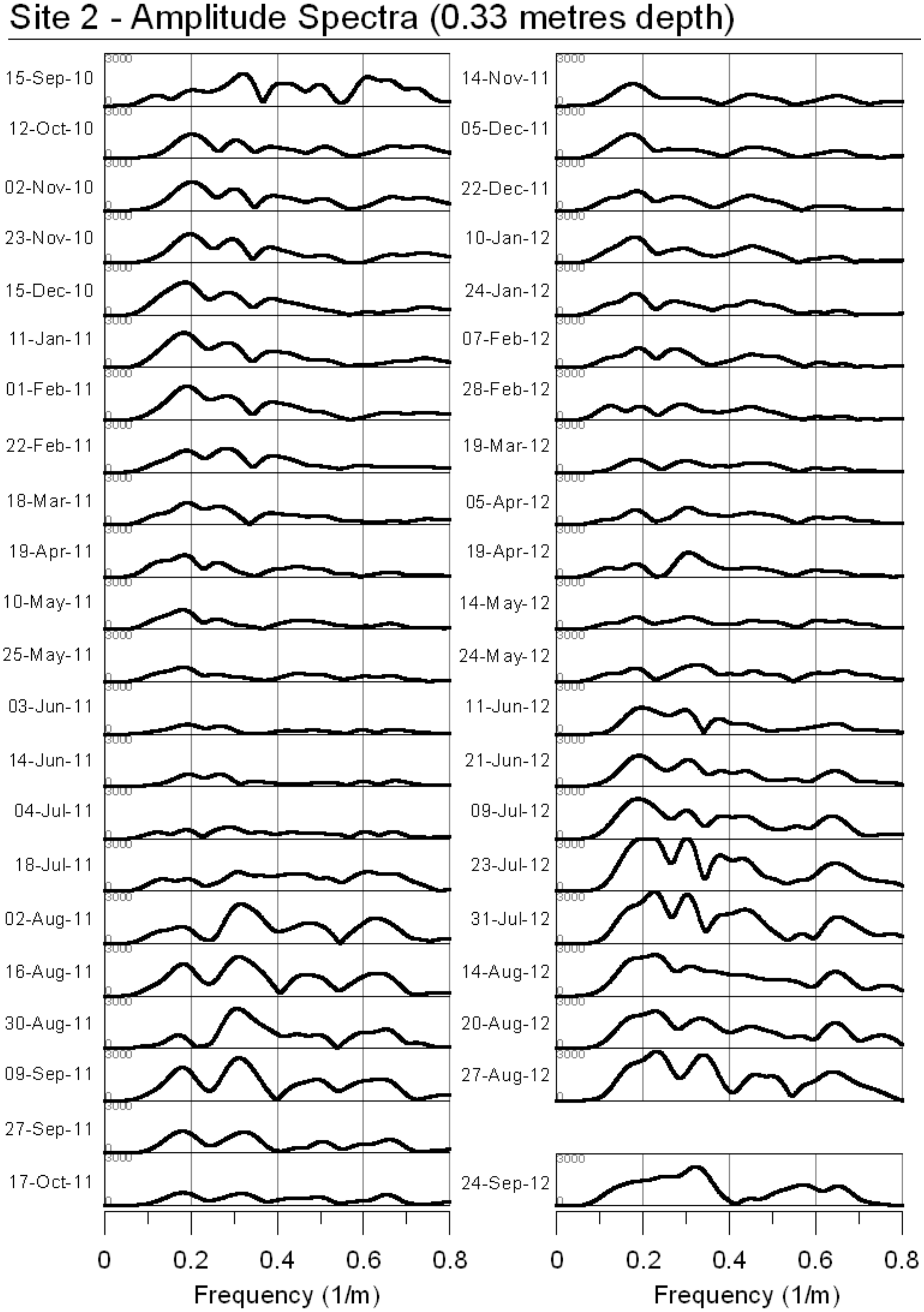

Figure 4.18 – FFT amplitude spectra for ERT inversion profile data at 0.33 metres depth at Site 2. Data gaps indicate period of no data collection.

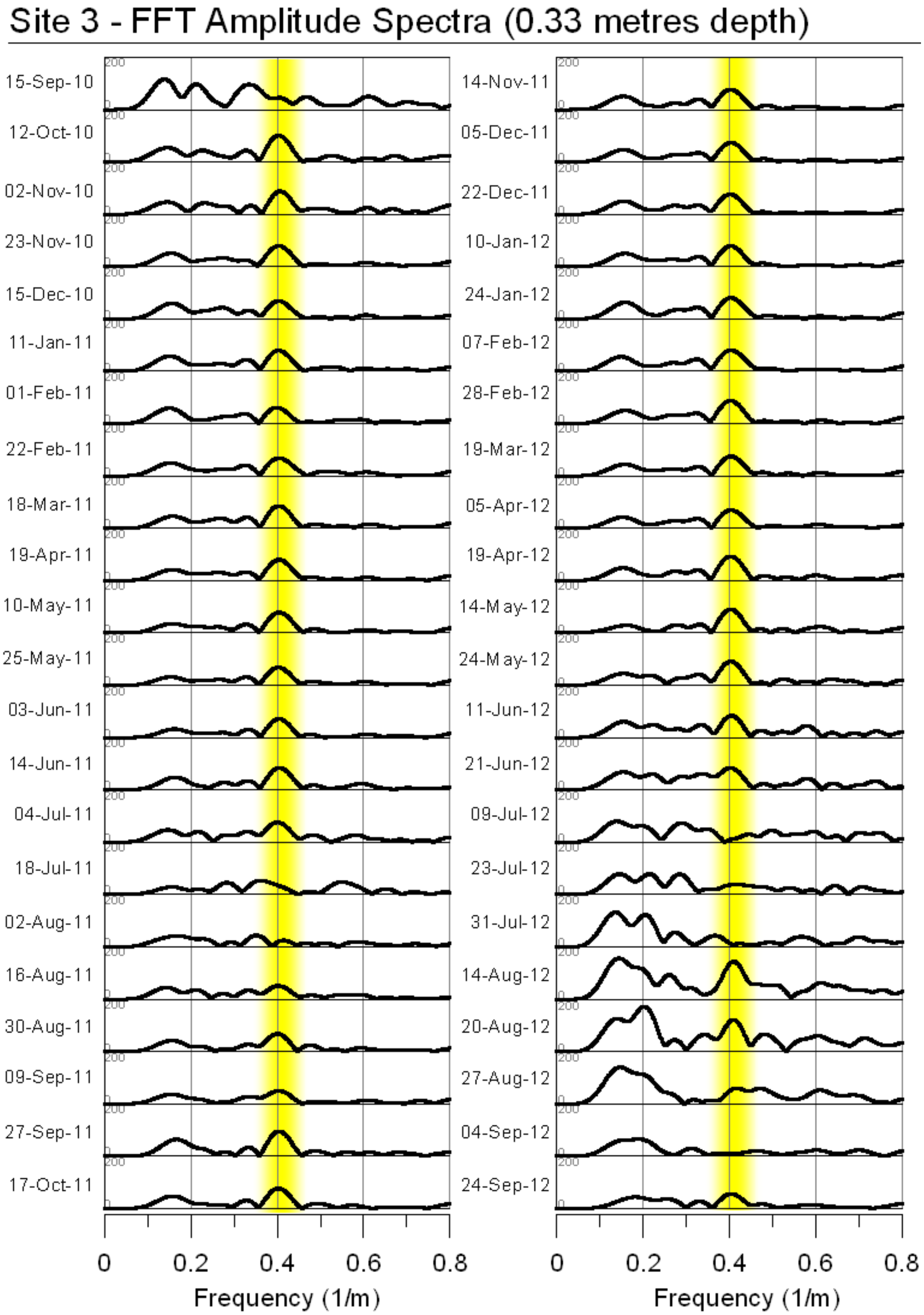

Figure 4.19 – FFT amplitude spectra for ERT inversion profile data at 0.33 metres depth at Site 3. The yellow highlights the 0.4 m^{-1} frequency component.

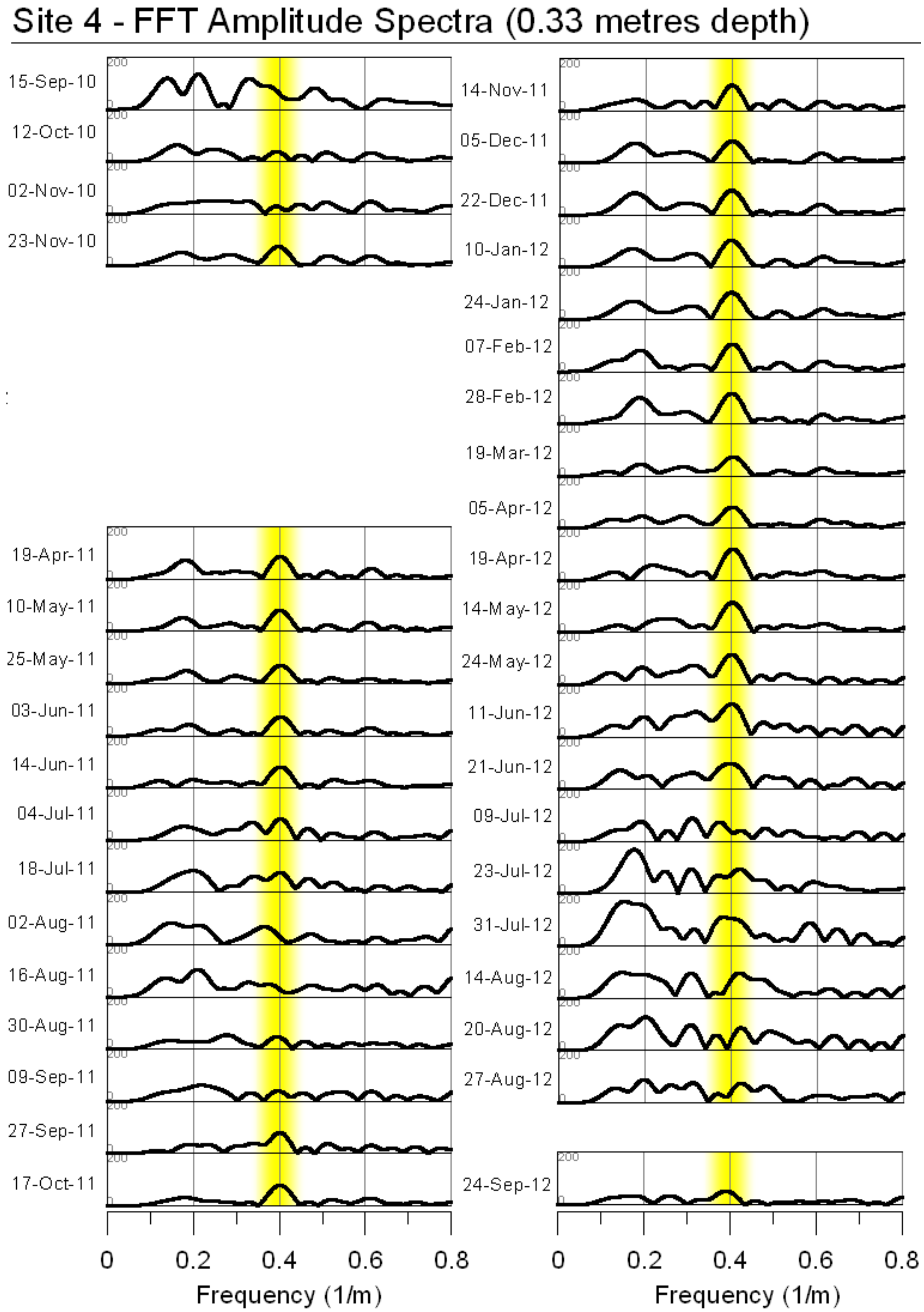

Figure 4.20 – FFT amplitude spectra for ERT inversion profile data at 0.33 metres depth at Site 4. The yellow highlights the 0.4 m^{-1} frequency component. Data gaps indicate period of no data collection.

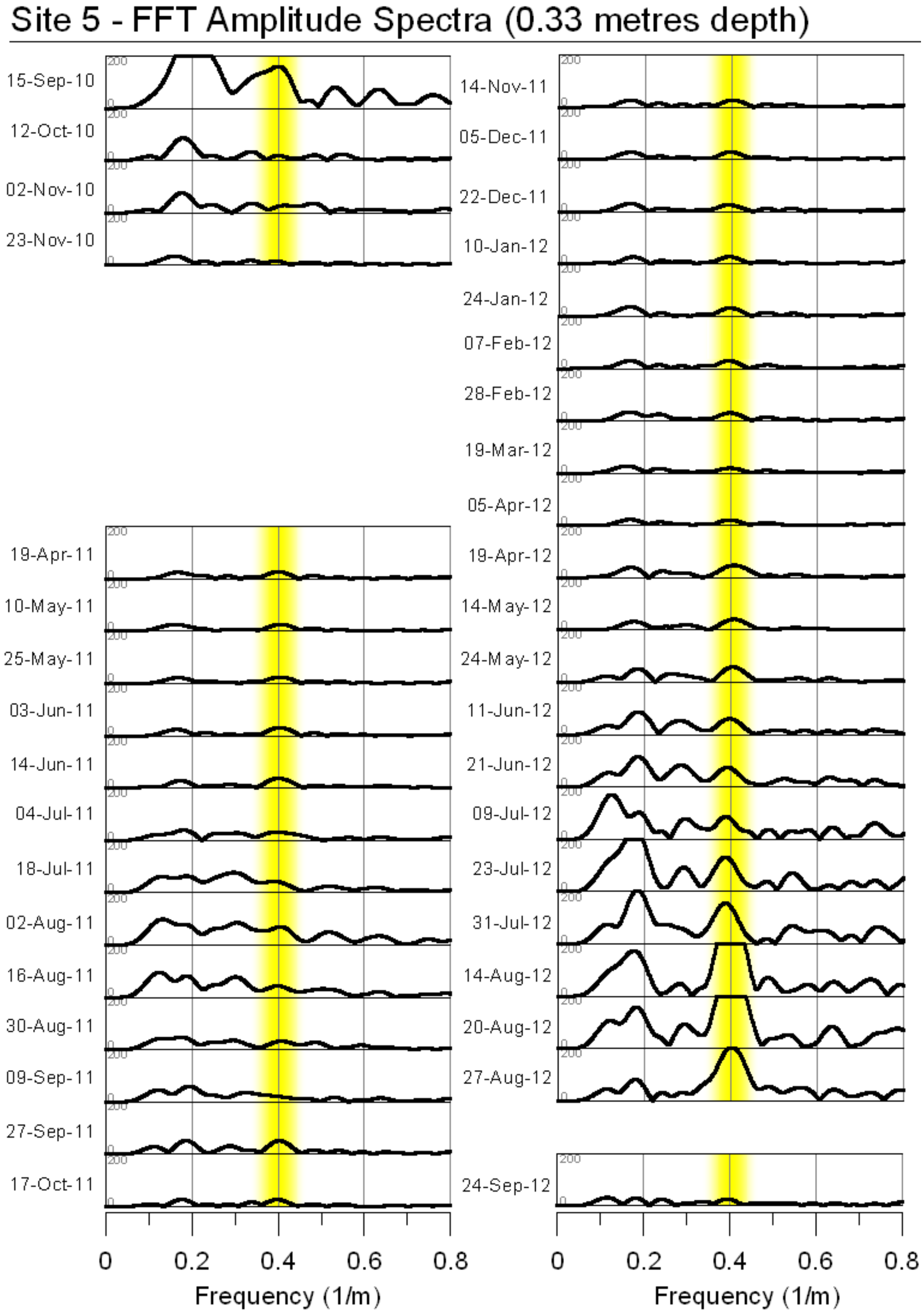

Figure 4.21 – FFT amplitude spectra for ERT inversion profile data at 0.33 metres depth at Site 5. The yellow highlights the 0.4 m^{-1} frequency component. Data gaps indicate period of no data collection.

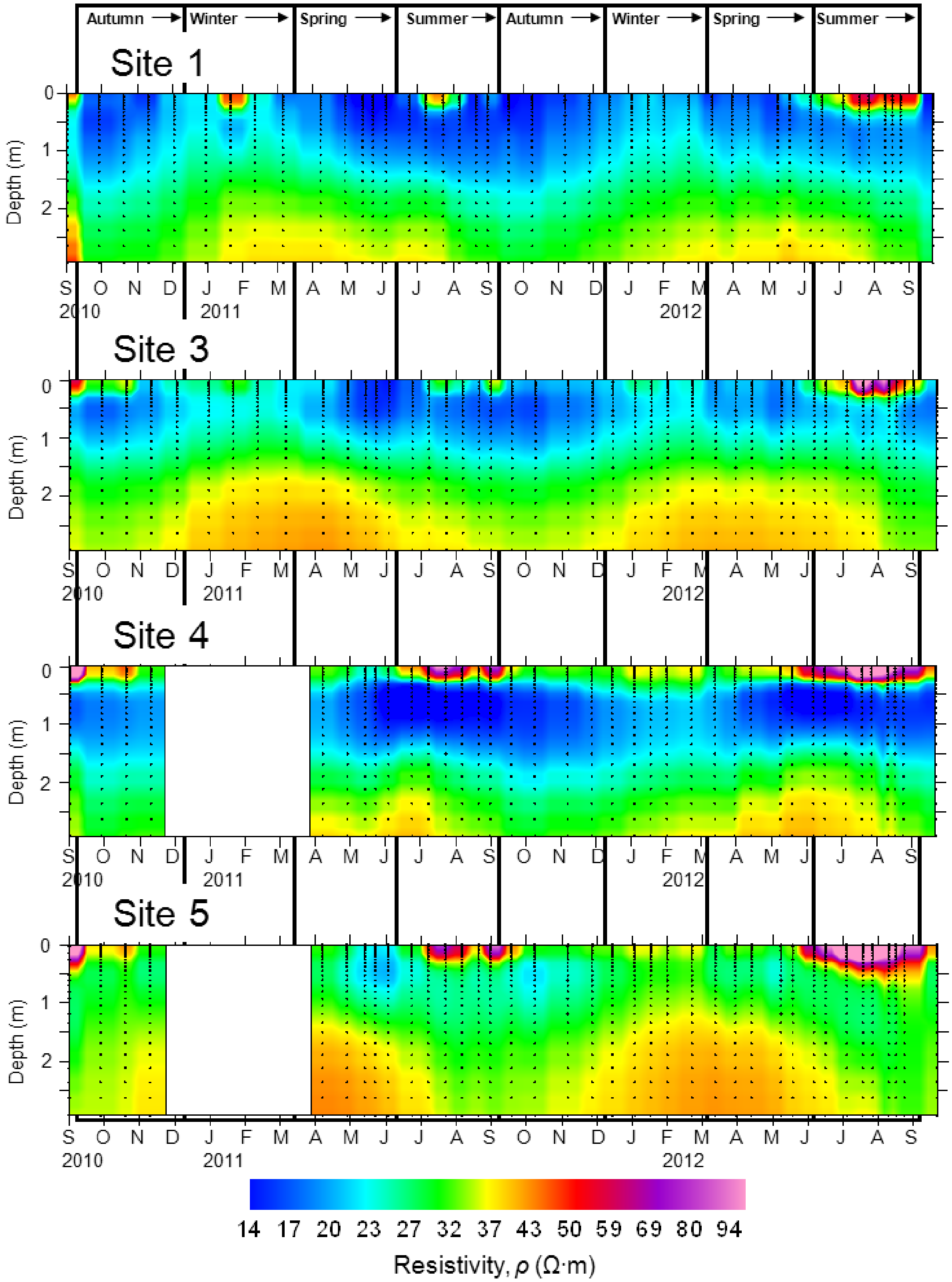

Figure 4.22 – Mean resistivity depth profiles (average from 9.00 – 15.00 metres along profile) presented as a time series for the two-years of monitoring at Sites 1, 3, 4 and 5. Data gaps for Sites 4 and 5 indicate period of no data collection at those sites.

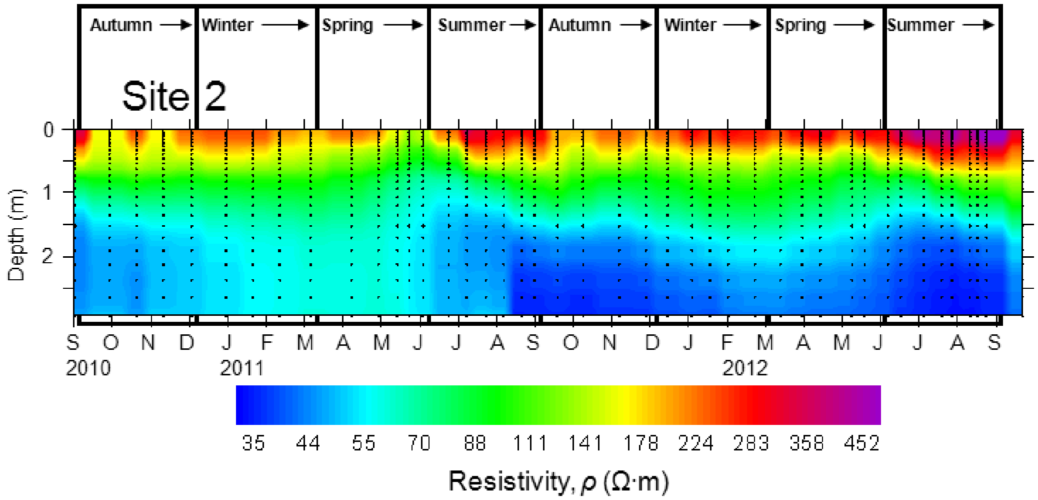

Figure 4.23 – Mean resistivity depth profile (average from 9.00 – 15.00 metres along profile) presented as a time series for the two-years of monitoring at Sites 2.

Site 1

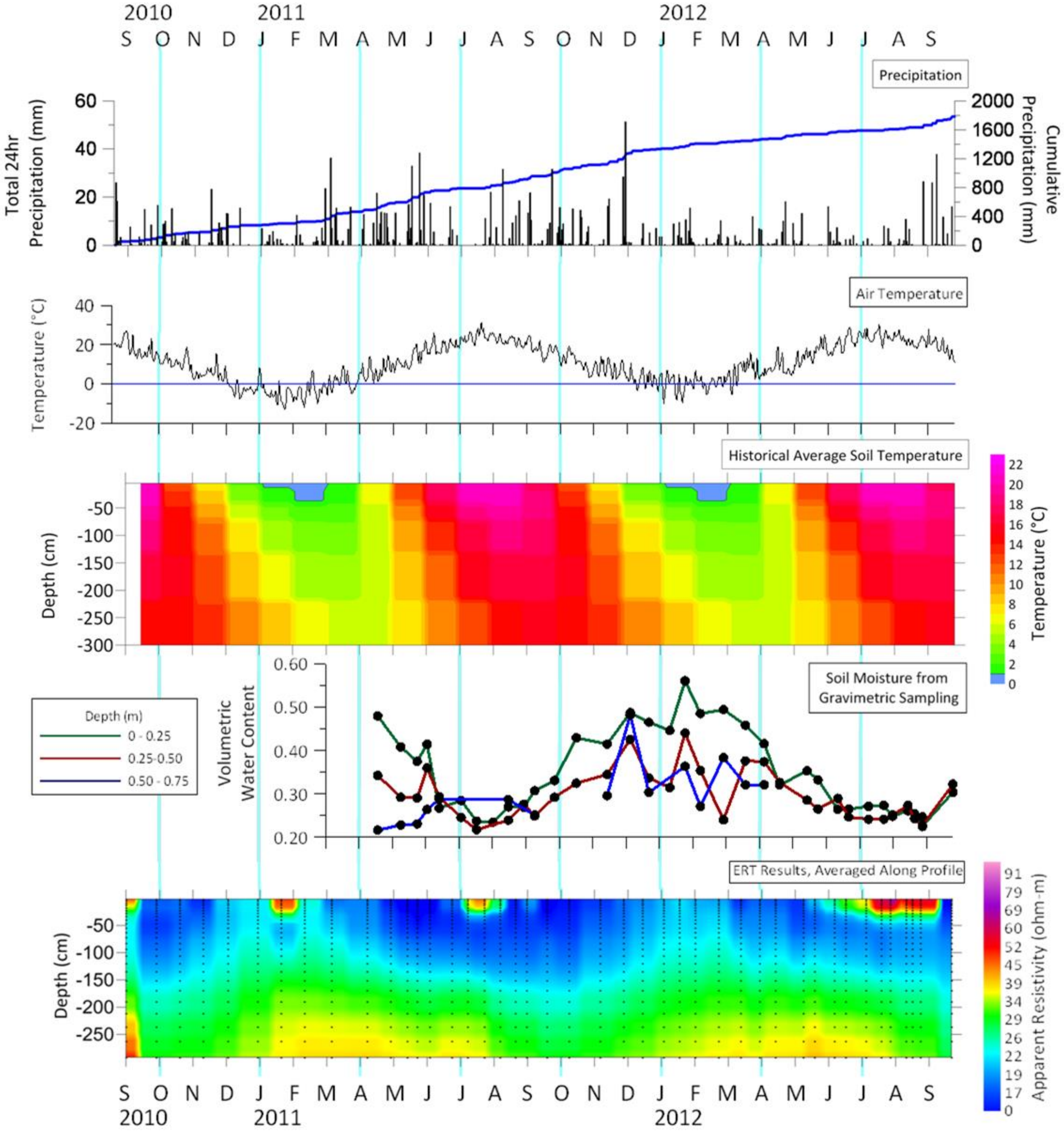

Figure 4.24 – Summarized data for Site 1 displaying precipitation, air and subsurface temperature, volumetric moisture content and mean resistivity depth profile.

Site 2

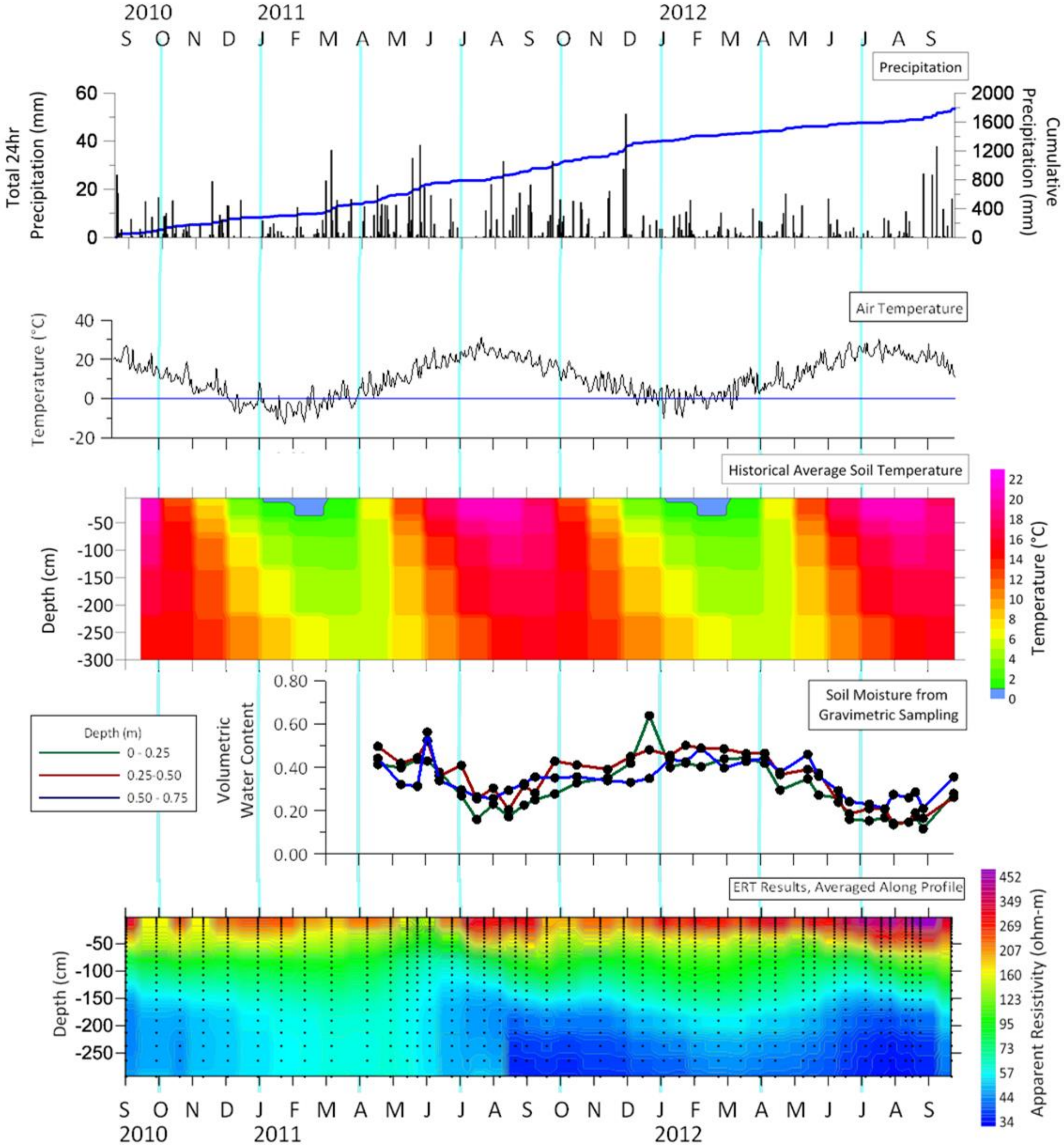

Figure 4.25 – Summarized data for Site 2 displaying precipitation, air and subsurface temperature, volumetric moisture content and mean resistivity depth profile.

Site 3

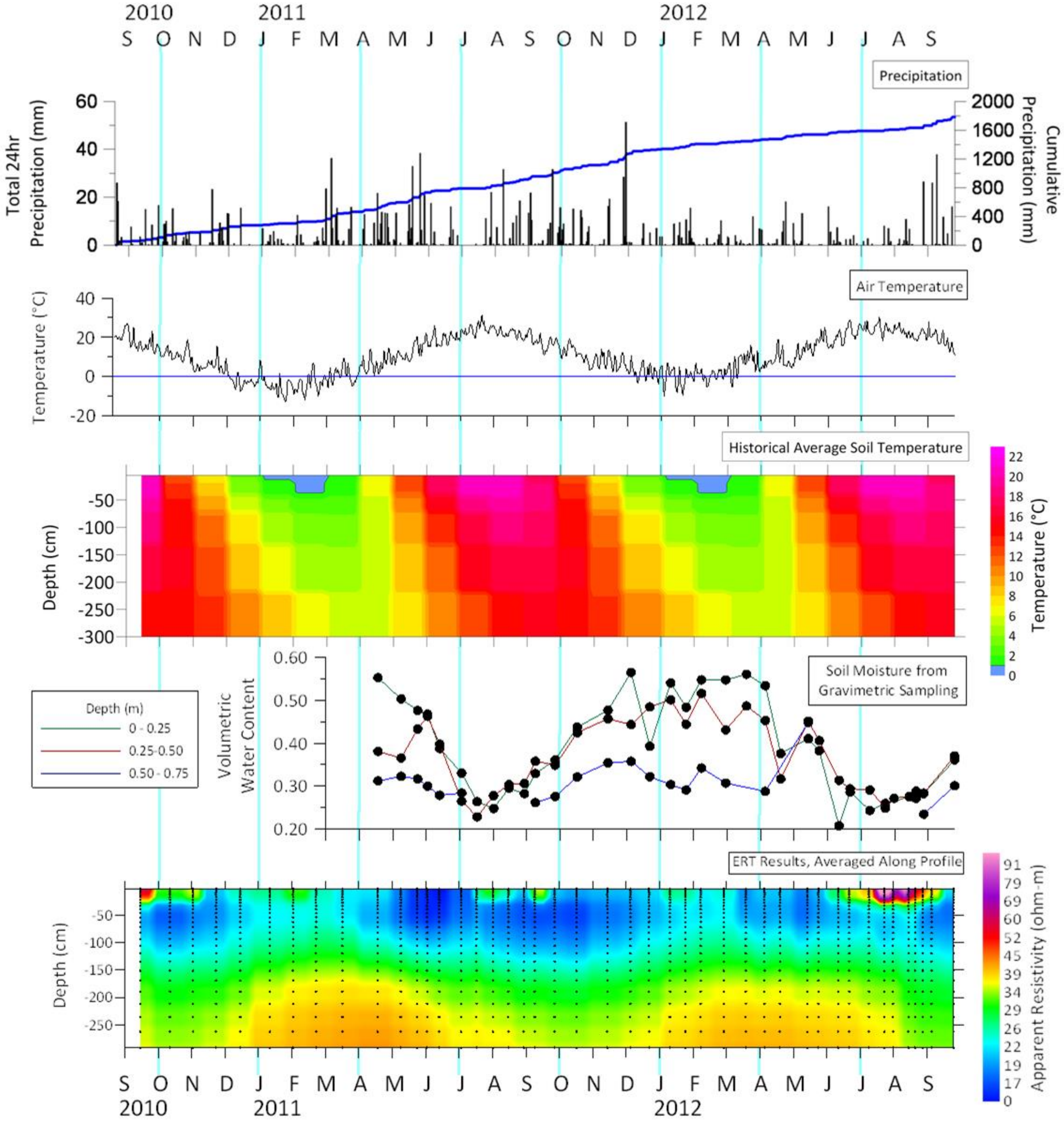

Figure 4.26 – Summarized data for Site 3 displaying precipitation, air and subsurface temperature, volumetric moisture content and mean resistivity depth profile.

Site 4

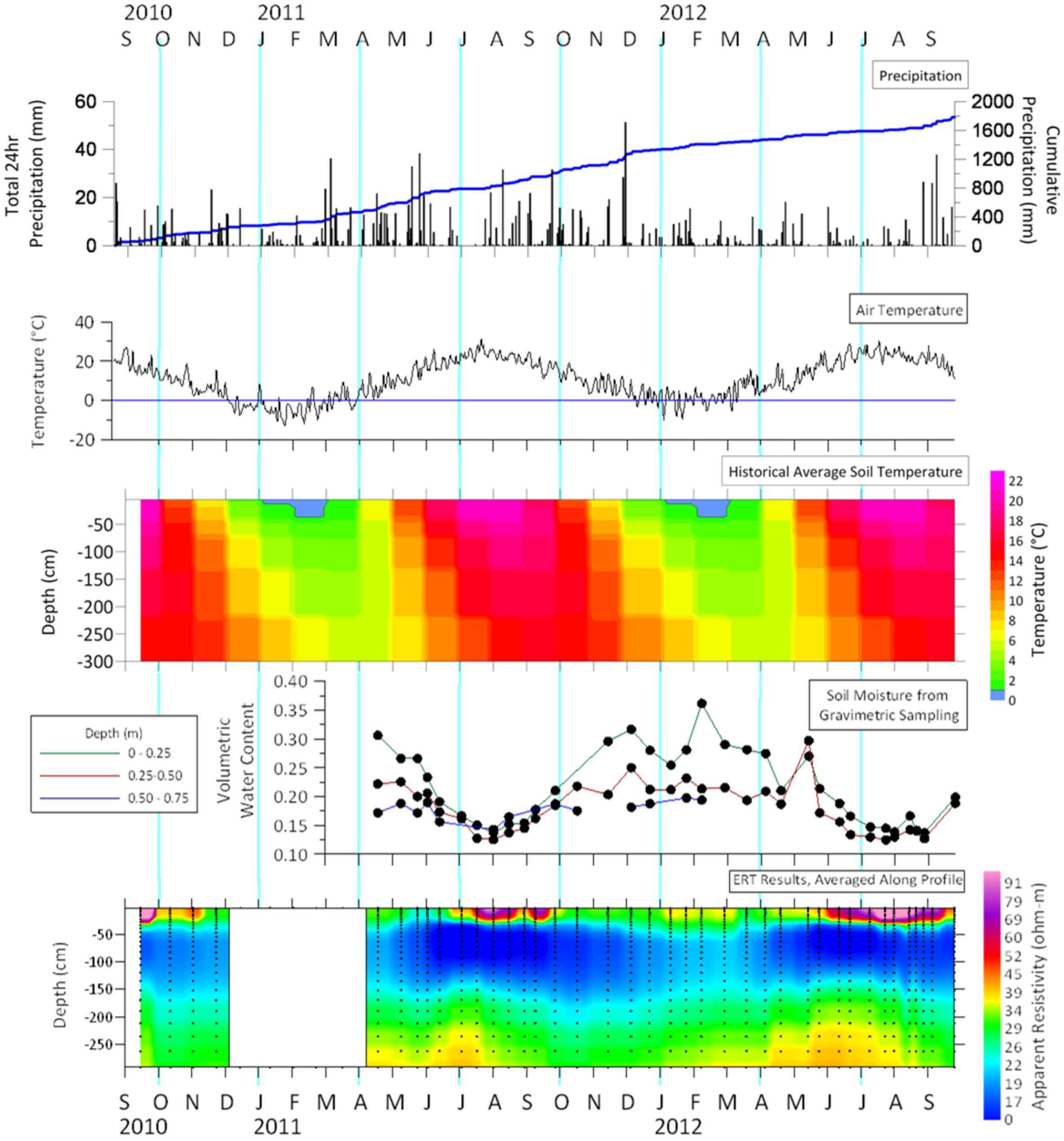

Figure 4.27 – Summarized data for Site 4 displaying precipitation, air and subsurface temperature, volumetric moisture content and mean resistivity depth profile.

Site 5

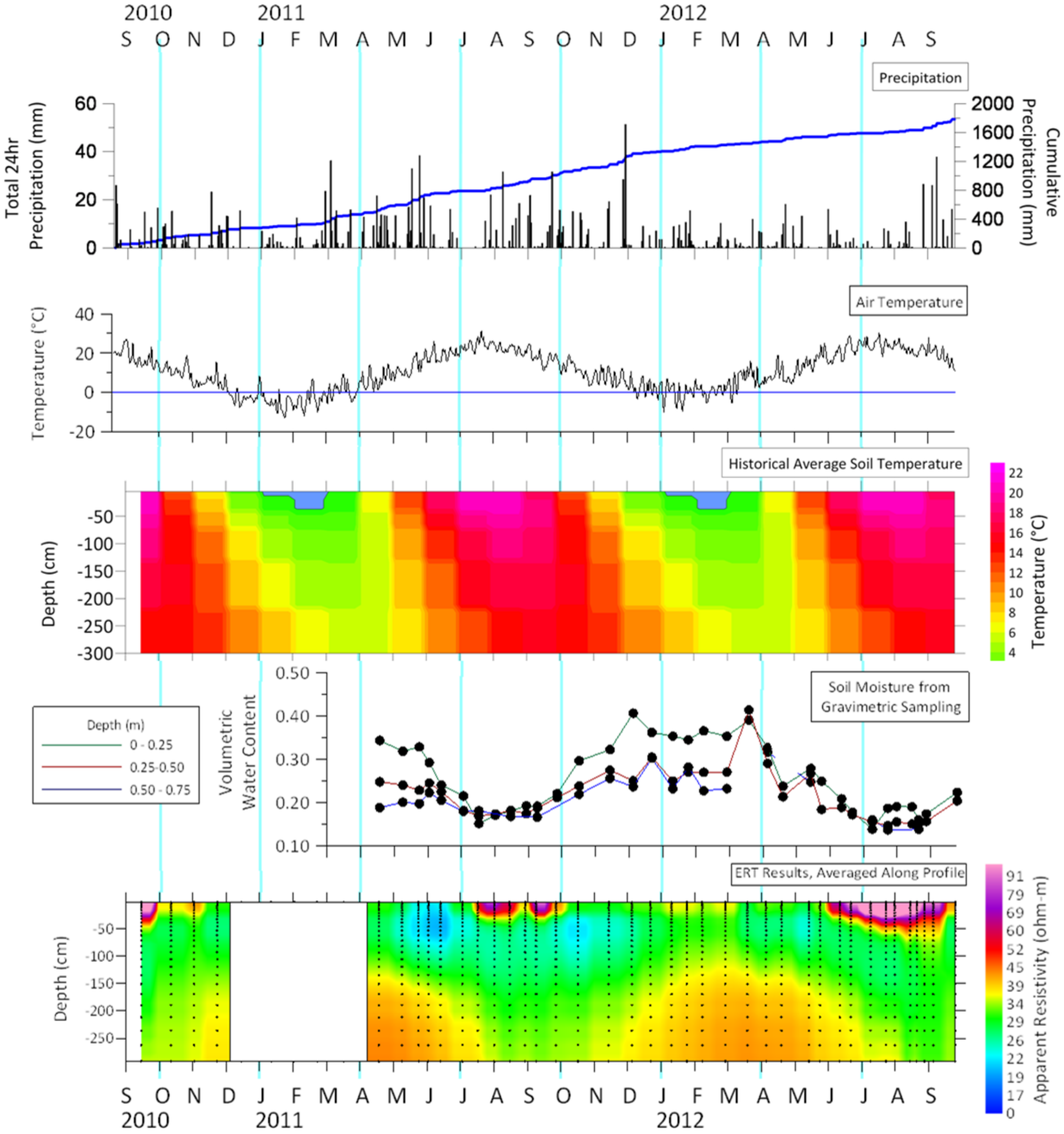

Figure 4.28 – Summarized data for Site 5 displaying precipitation, air and subsurface temperature, volumetric moisture content and mean resistivity depth profile.

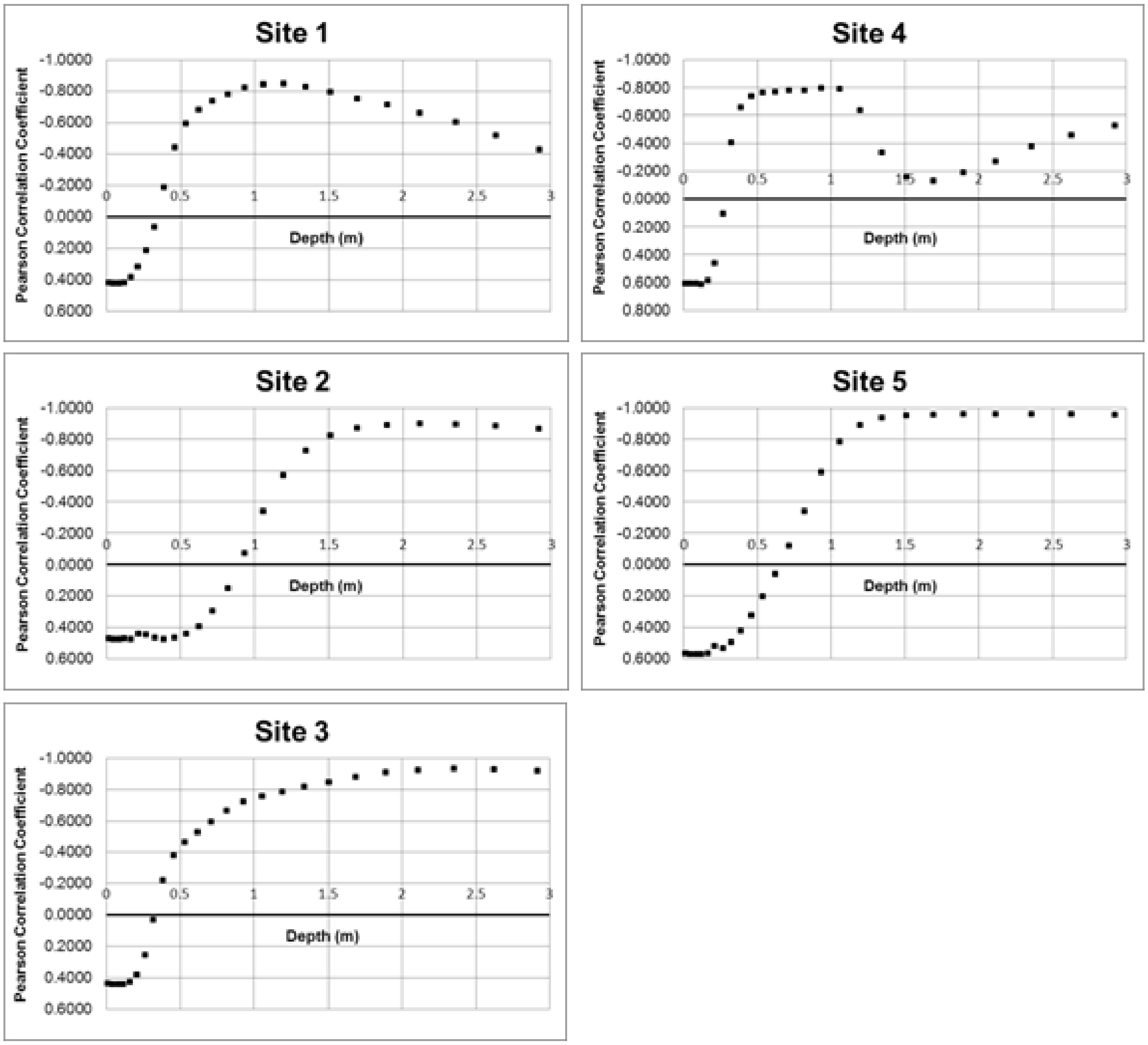

Figure 4.29 – Pearson product-moment correlation coefficient for the linear dependency between historic subsurface temperatures and inverted resistivity results at each model depth layer.

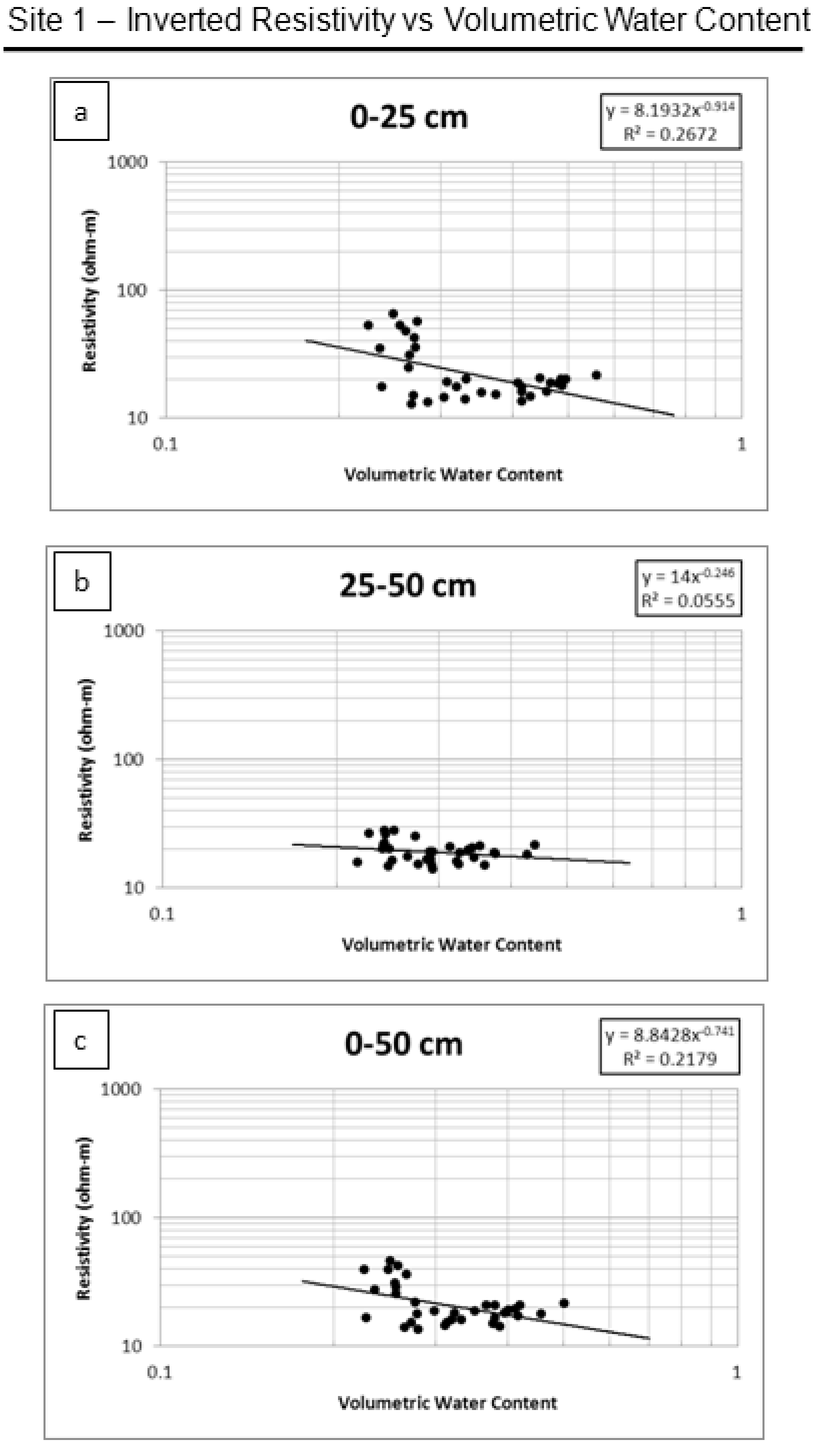

Figure 4.30 – Comparison of averaged inverted resistivity values to volumetric water content data for three depth intervals at Site 1.

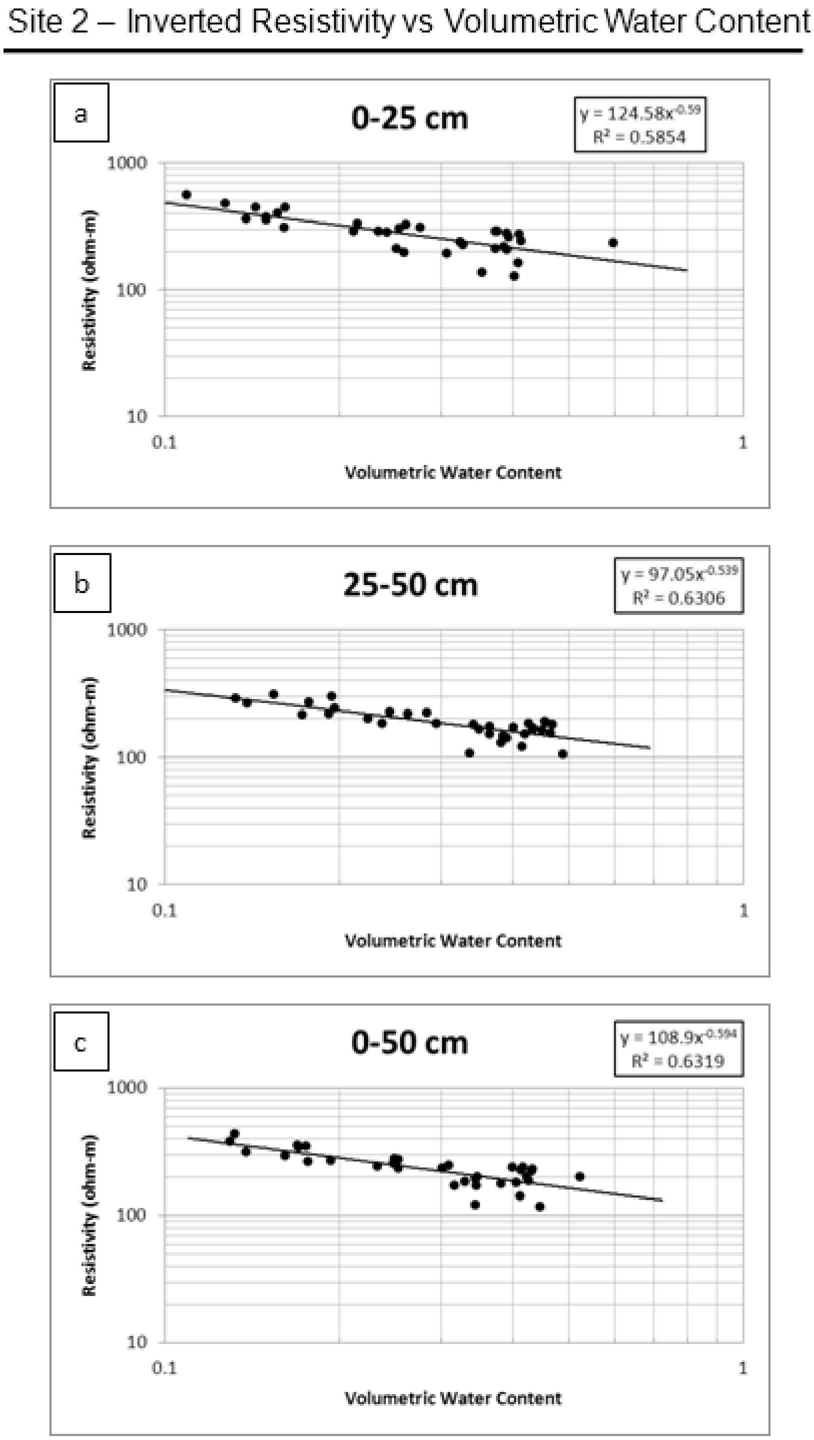

Figure 4.31 – Comparison of averaged inverted resistivity values to volumetric water content data for three depth intervals at Site 2.

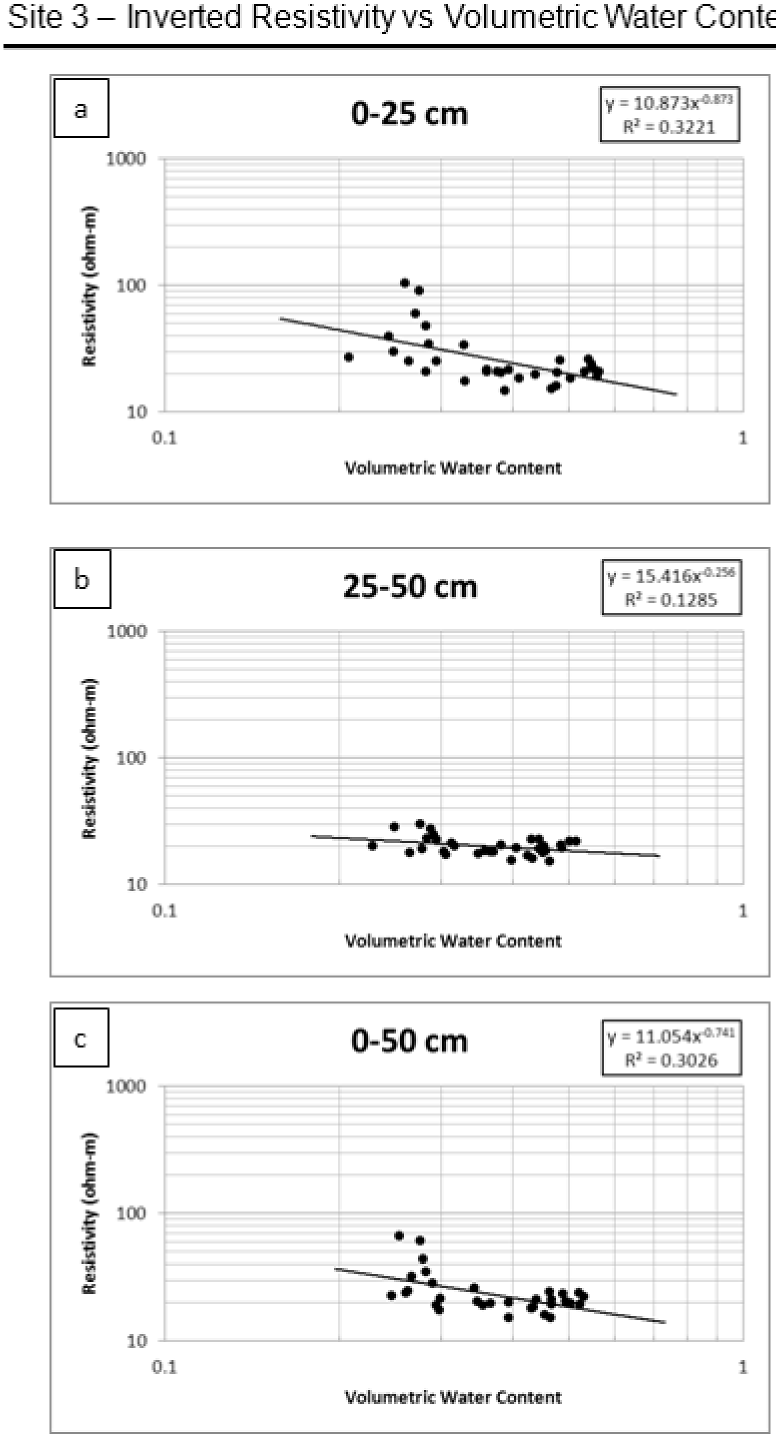

Figure 4.32 – Comparison of averaged inverted resistivity values to volumetric water content data for three depth intervals at Site 3.

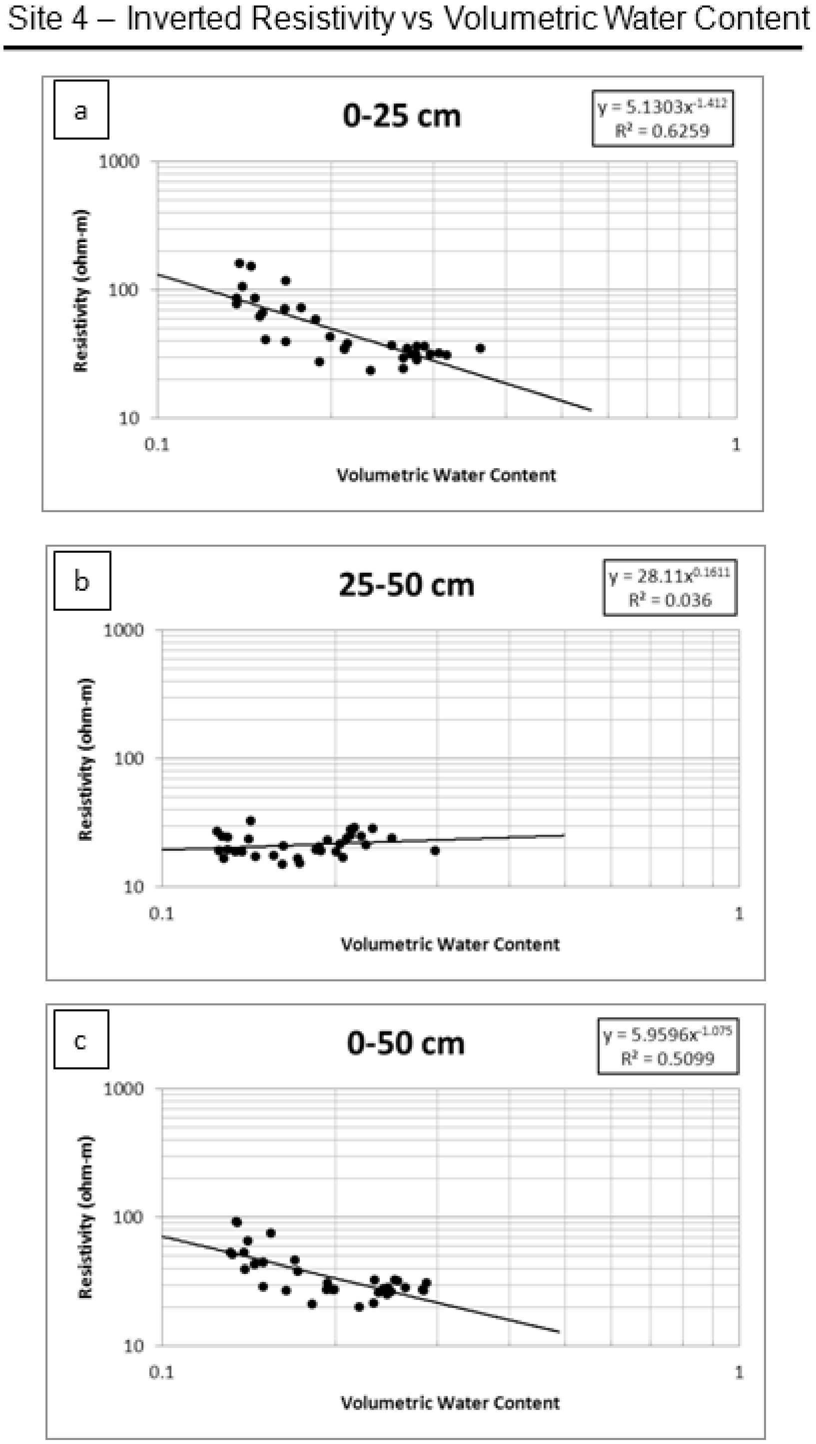

Figure 4.33 – Comparison of averaged inverted resistivity values to volumetric water content data for three depth intervals at Site 4.

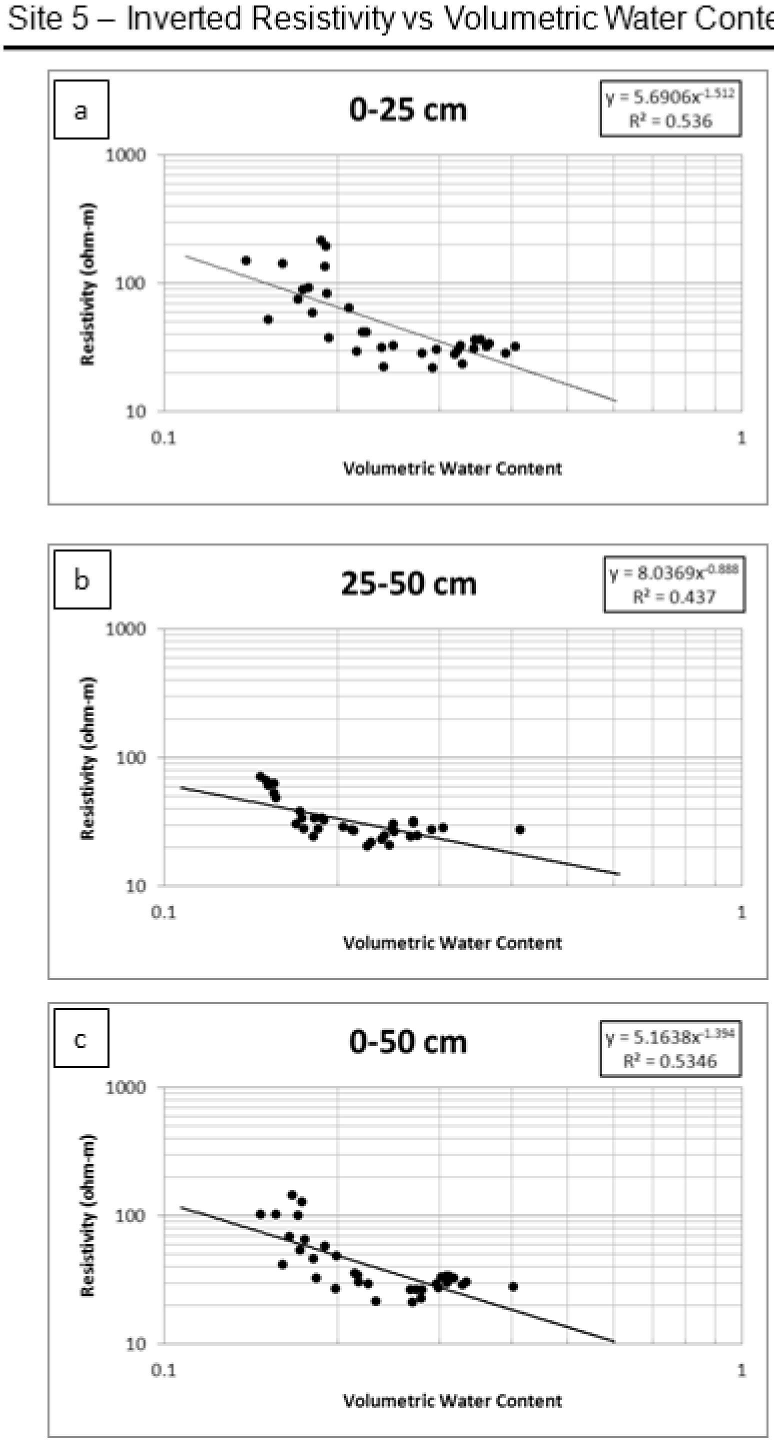

Figure 4.34 – Comparison of averaged inverted resistivity values to volumetric water content data for three depth intervals at Site 5.

Table 4.1 – ERT monitoring schedule giving dates of data acquisition.

Acquisition Day #	Date	Days since previous	ERT	Notes
1	15 September 2010	-	YES	
2	12 October 2010	27	YES	
3	02 November 2010	21	YES	
4	23 November 2010	21	YES	
5	15 December 2010	22	YES	Only at Sites 1, 2, 3
6	11 January 2011	27	YES	Only at Sites 1, 2, 3
7	01 February 2011	21	YES	Only at Sites 1, 2, 3
8	22 February 2011	21	YES	Only at Sites 1, 2, 3
9	18 March 2011	24	YES	Only at Sites 1, 2, 3
10	19 April 2011	32	YES	
11	10 May 2011	21	YES	
12	25 May 2011	15	YES	
13	03 June 2011	9	YES	
14	14 June 2011	11	YES	
15	04 July 2011	20	YES	
16	18 July 2011	14	YES	
17	02 August 2011	15	YES	
18	16 August 2011	14	YES	
19	30 August 2011	14	YES	
20	09 September 2011	10	YES	
21	27 September 2011	18	YES	
22	17 October 2011	20	YES	
23	14 November 2011	28	YES	
24	05 December 2011	21	YES	
25	22 December 2011	17	YES	
26	10 January 2012	19	YES	
27	24 January 2012	14	YES	
28	07 February 2012	14	YES	
29	28 February 2012	21	YES	
30	19 March 2012	20	YES	
31	05 April 2012	17	YES	
32	19 April 2012	14	YES	
33	14 May 2012	25	YES	
34	24 May 2012	10	YES	
35	11 June 2012	18	YES	
36	21 June 2012	10	YES	
37	09 July 2012	18	YES	
38	23 July 2012	14	YES	
39	31 July 2012	8	YES	
40	14 August 2012	14	YES	
41	20 August 2012	6	YES	
42	27 August 2012	7	YES	
43	04 September 2012	8	YES	Only at Site 3
44	24 September 2012	20	YES	

Table 4.2 – Summary of RES2DINV inversion parameters used. An asterisk (*) beside the setting indicates the default value was used.

Parameter	Setting
Inversion Damping Parameters	
Initial damping factor	0.150*
Minimum damping factor	0.020*
First layer damping factor	5.000*
Damping factor increase with depth	1.10*
Damping factor optimization?	Yes
Limit model resistivity?	No
Vertical-to-horizontal flatness filter ratio	1.0*
Mesh Parameters	
Finite mesh grid size	4 nodes
Type of forward modeling method	Finite-Difference
Mesh refinement	Finest Mesh
Number of nodes per electrode spacing	4 nodes
Inversion Methods and Settings	
Use combined Marquardt and Occam inversion?	No
Data Inversion Constraint: standard least-squares or robust	Robust
Robust data constraint cutoff factor	0.050
Model Inversion Constraint: standard least-squares or robust	Robust
Robust model constraint cutoff factor	0.005
Automatically allow model blocks to exceed data points?	Yes
Reduce effect of side blocks?	No
Limit range of model resistivity values?	No
Use fast calculation of Jacobian matrix?	No
Standard or incomplete Gauss-Newton optimization?	Standard
Fast inversion?	No
Time-lapse Inversion Constraints	
Type of time-lapse constraint	Least-squares smoothness constraint
Simultaneous or sequential inversion method	Simultaneous
Type of Time-Lapse Data: direct or difference	Direct
Reference model	Preceding data set
Time-constraint weight	0.200*
Model Discretization	
Thickness of first layer	0.125 x 0.25 m = 0.03125 m
Factor layer thicknesses increases by with depth	1.1000
Extend Model?	No
Model blocks must have equal widths?	Yes
Use model-refinement?	Yes

Table 4.3 – The RMS percent-error obtained for the inversions of each data set.

Date	Site 1	Site 2	Site 3	Site 4	Site 5
15 September 2010	2.70	1.28	1.04	1.01	1.00
12 October 2010	0.58	1.06	0.73	0.55	0.91
02 November 2010	0.55	1.03	0.79	0.66	1.04
23 November 2010	0.55	1.01	0.40	0.39	0.60
15 December 2010	0.62	0.97	0.45	Survey not performed	
11 January 2011	0.69	1.02	0.51	Survey not performed	
01 February 2011	1.28	0.87	0.54	Survey not performed	
22 February 2011	0.59	0.82	0.45	Survey not performed	
18 March 2011	0.70	0.86	0.44	Survey not performed	
19 April 2011	0.60	0.83	0.48	0.52	0.43
10 May 2011	0.63	0.96	0.54	0.54	0.57
25 May 2011	0.57	0.96	0.49	0.54	0.54
03 June 2011	0.63	0.88	0.56	0.51	0.56
14 June 2011	1.24	0.80	0.76	0.71	0.92
04 July 2011	1.33	0.93	0.98	1.71	1.43
18 July 2011	1.89	1.13	1.65	2.10	1.32
02 August 2011	1.82	1.35	1.21	1.85	1.22
16 August 2011	1.50	1.12	1.07	1.36	1.11
30 August 2011	0.75	1.40	0.88	1.21	0.99
09 September 2011	0.71	1.21	0.97	0.98	0.99
27 September 2011	0.41	1.14	0.69	0.60	0.81
17 October 2011	0.57	0.96	0.61	0.48	0.53
14 November 2011	0.61	0.85	0.53	0.52	0.48
05 December 2011	0.58	1.00	0.43	0.48	0.38
22 December 2011	0.58	0.88	0.45	0.50	0.44
10 January 2012	0.54	0.84	0.46	0.47	0.45
24 January 2012	0.65	1.28	0.40	0.51	0.41
07 February 2012	0.72	0.86	0.46	0.48	0.42
28 February 2012	0.58	0.92	0.47	0.50	0.42
19 March 2012	0.67	0.87	0.46	0.51	0.45
05 April 2012	0.65	0.81	0.51	0.56	0.53
19 April 2012	0.92	0.92	0.73	0.75	0.97
14 May 2012	1.00	0.84	0.87	0.93	0.86
24 May 2012	2.4	1.01	1.05	1.20	1.21
11 June 2012	2.2	1.35	1.31	1.44	1.24
21 June 2012	2.3	1.33	1.99	1.64	1.39
09 July 2012	2.4	1.47	1.72	1.73	1.54
23 July 2012	2.1	1.48	1.42	1.41	1.35
31 July 2012	2.2	1.23	1.72	1.35	0.99
14 August 2012	1.21	1.30	1.17	0.85	0.83
20 August 2012	1.3	1.31	1.29	1.09	0.98
27 August 2012	1.64	2.70	1.28	0.90	0.99
04 September 2012	Survey not performed		1.14	Survey not performed	
24 September 2012	0.58	1.47	0.88	0.78	1.15

Chapter 5 MONITORING SOIL MOISTURE DYNAMICS BY ELECTROMAGNETIC INDUCTION

5.1 Introduction

High-resolution near-surface electromagnetic induction (EMI) surveys were performed at multiple monitoring sites during a two-year study to examine the response of EMI instruments to soil moisture dynamics. Acquisition of EMI data occurred on forty-three dates between 15 September 2010 and 24 September 2012. Surveys were performed along 25-metre profile lines at three of the five established monitoring sites located at the RGRS: Sites 3, 4 and 5. Sites 1 and 2 were not surveyed due to potential interference from the intersecting trellis network (Section 3.2). The monitoring schedule is summarized in Table 5.1.

5.2 EMI Data Acquisition and Management

The primary ground conductivity meter (GCM) used in this study is the Geonics EM38 (Geonics Ltd; Mississauga, Canada). The coil separation of the EM38 is 1.00 metre and the operating frequency is 14.6 Hz. At Site 3, data was also collected with the Geonics EM31-MK2 (Geonics Ltd.; Mississauga, Canada). The EM31 is a GCM with a coil separation of 3.66 metres and an operating frequency of 9.8 Hz. The larger coil separation allows for a greater depth of investigation at Site 3. Both GCMs were operated in both the vertical and horizontal dipole orientations. Figure 5.1 displays the relative response curves for both instruments at depths between 0 and 10 metres. These response curves allow for a comparison of the effective investigation depths and nature of the sensitivity with depth of both GCM in each dipole orientations.

Data was collected along the 25-metre profiles established at each monitoring site (Section 3.2). EM38 surveys were performed by acquiring readings every 0.25 metres along the profile for a total of 101 data points per profile. Each EM38 reading consisted of 10 measurements that were averaged together and stored on a Juniper Systems TK6000 handheld computer (Juniper Systems; Logan UT, USA). EM31 surveys were performed by acquiring readings every 0.50 metres for a total of 51 data points per profile. Each EM31 reading consisted of 10 measurements that were averaged together and stored on a Polycoder 720 handheld computer (Wescor Inc.; Logan UT, USA). Figure 5.2 shows examples of the data acquisition with each device.

A start-up and calibration routine for the EM38 was performed at the commencement of each acquisition day. Prior to calibration, the EM38 would be turned on and positioned at Site 3 without disturbance for a minimum of ten minutes. It had been found through previous studies (e.g., Robinson et al., 2004) that this instrument may lack stability if it is not given time to equilibrate to the field site conditions. After the equilibration period, the instrument was calibrated by following the steps outlined in the EM38 operating manual (Geonics Ltd., 2001). To ensure consistent calibration between acquisition dates, calibration sequences intended to be completed at 1.5 metres above ground level were completed on top of a 1.5-metre-long wooden pole. Calibration was always performed at the 12-metre position on the survey profile at Site 3 to ensure that the calibration procedure and environment was consistent between acquisition dates.

Test lines performed at the start and end of data acquisition on three acquisition days corresponding to wet (19 April 2011) and dry (02 August 2011 and 30 August 2011) subsurface conditions reveals a maximum mean drift of 0.9 mS/m over the course of each survey date (Figure 5.3), indicating that minor instrument drift occurred throughout the acquisition day. In addition to these repeated test lines, repeat EM38 measurements were regularly made at the 6, 12 and 18 metre positions at Site 3 following EM38 data acquisition throughout the monitoring period to ensure no substantial drift had occurred during data acquisition for the day.

The EM31 is factory-calibrated and does not require additional calibration before or between surveys. In contrast to the common EM31 operating procedure where measurements are taken while carrying the instrument one metre above the ground surface (Geonics Ltd., 1995), the EM31 data in this survey was acquired with the instrument placed directly on the ground (Figure 5.2) to achieve the maximum penetration depth. To convert the instrument readings to the equivalent ground level measurements, the following conversion factor provided by the instrument manufacturer was used:

$$\sigma_a(ground) = \frac{\sigma_a(reading)}{1.12} \tag{5.1}$$

where $\sigma_a(ground)$ is the EM31 reading if the instrument had been calibrated to be operated on the ground and $\sigma_a\ (reading)$ is the actual measurement read by the instrument.

Following data acquisition, conductivity data were downloaded from the field computers to a desktop computer. Quality control was performed to ensure the data was properly acquired and transferred.

It was apparent from the EM38 data acquired that the metal components of the survey tape (i.e., end clip and reel) interfered with measurements along the first and last metre of the profile, resulting in data spikes at these locations. As a result, the first and last two metres of the profile have been removed for each survey date. No other edits were made to the data. Therefore, each final EM38 data set contains 93 data points along the profile while the final EM31 data sets contain 47 data points per profile.

5.3 EM38 Results

5.3.1 Individual Profile Results

5.3.1.1 Survey Results

Selected EM38 profiles from Sites 3 – 5 are displayed in Figures 5.4 and 5.5 for data obtained in the vertical and horizontal dipole orientations, respectively. The dates selected show examples of profile data during a range of subsurface moisture conditions. Winter, wet spring, very-dry late summer and autumn-wetting conditions correspond to the 28 February 2012, 14 May 2012, 14 August 2012 and 24 September 2012 profiles, respectively, while 19 April 2012 and 21 June 2012 dates correspond respectively to mid-spring and mid-summer transitional soil moisture conditions, respectively. The complete data set for each monitoring site is displayed in a time-profile plot in Figures 5.6 and 5.7. The time-profile plots depict apparent conductivity values for all acquisition dates (along the x-axis) and at all profile positions (along the y-axis). The complete set of profiles can be found in Appendix A.

Several observations can be made about the EMI response from the data presented in Figures 5.4 – 5.7. These figures show that apparent conductivity values correlate with the seasonal conditions described in Section 3.3. Wetter spring and autumn periods are associated with higher conductivity values while dry summer and frozen winter periods experience lower overall conductivity values. Comparing monitoring sites, it is clear that Site 5 is consistently the less conductive site. It is also notable that measurements conducted in the vertical dipole orientation are consistently more conductive than the corresponding measurements made in the horizontal dipole orientation.

It is observable from Figures 5.4 – 5.7 that lateral variations are present in the apparent conductivity along each profile line at each monitoring site. The lateral variations can be separated into two types: large-scale and small-scale variations. Large-scale lateral variations are present in the apparent conductivity across the survey profiles at the three monitoring sites; however, they are minor when compared to the magnitude of the seasonal variation in apparent conductivity. The general large-scale lateral trends are consistently observable at each site between acquisition dates although features are more prominent on dates with lower overall conductivity.

The more significant small-scale lateral variation is the cyclic component that is very prominent in the vertical dipole orientation data during the wettest conditions. During the wet conditions, the magnitude of the apparent conductivity variation associated with these cyclic features is significantly larger than the magnitude of fluctuations due to large-scale lateral variability across the entire profile. The lateral cyclic component is further discussed in Section 5.3.1.2.

Site 5 contains spike features from 17.5 to 20 metres on the profile line that are uncharacteristic of the electrical conductivity signature expected from naturally occurring subsurface conditions. These spikes are observed in both dipole orientations, but are more prominent in the results for the horizontal dipole orientation, suggesting that the source is shallow. Examination of Site 5 found no potential source for these spikes present at the surface. Since digging was not permitted, a buried source remains a possibility.

5.3.1.2 Analysis of Lateral Cyclic Features

It is clear from the apparent conductivity profiles in Figure 5.4 and the time-profile plots in Figure 5.6 that the lateral variability of the conductivity observed by the EM38 along each profile line in the vertical dipole orientation contains a cyclic component at each of the three monitoring sites. The figures suggest that the strength of the cyclic component in the profile data varies seasonally, with dry conditions associated with smaller amplitude cyclic component.

Fast Fourier transform (FFT) analysis was performed on vertical dipole orientation profile data to characterize the frequency of the cyclic component between monitoring sites and acquisition dates. Prior to performing the FFT computation, a 5th-order best-fit polynomial was removed from each data profile. The removal of the 5th-order trend across the profile enhanced the residual cyclic signature by minimizing the response of the DC and low-frequency components in the resulting amplitude spectra. FFT computation was performed on the resulting residual profile using the Excel 2010 Analysis ToolPak, (Microsoft; Redmond, USA). The residual profile was zero-padded for a total of 4096 data points to create a well-discretized amplitude spectrum. Resulting FFT amplitude spectra are displayed in Figures 5.8 – 5.10 for Sites 3 – 5, respectively. Analysis of the results at Site 3 (Figure 5.8) shows a well-defined and re-occurring frequency component at approximately 0.4 m^{-1}. The magnitude of this frequency component between acquisition dates varies with dry, low-conductivity data sets containing a significantly weaker 0.4 m^{-1} component in the FFT analysis. Comparable results were obtained at Sites 4 (Figure 5.9) and 5 (Figure 5.10). The magnitude of the 0.4 m^{-1} component is the largest at Site 3 and the smallest at Site 5. The value of 0.4 m^{-1} translates to a spatial wavelength of 2.5 metres.

5.3.2 Profile Means

To further study the temporal evolution in the EM38 data set, each profile was represented by a single conductivity value for each acquisition date. This value is the mean conductivity along the profile from 9.00 to 15.00 metres. This range along the profile was chosen to coincide with the length of profile chosen for mean resistivity analysis in the ERT component of this study. The spike features observed in profiles at Site 5 occur outside of this range and do not impact the calculation of the mean. Figure 5.11 shows the EM38 data summarized in this manner.

The mean conductivity values show consistent seasonal variations at all three monitoring sites. In general, higher values occur during the relatively wetter autumn, winter and spring periods while lower values occur in the drier summer. Further, the effects of contrasting annual cycle conditions are evident in Figure 5.11. It can be seen that the mean conductivity values during the 2011 spring and summer period are persistently higher than the corresponding values for the 2012 spring and summer period. This pattern correlates with lower cumulative precipitation experienced during the 2012 season compared to the 2011 season, as seen in Figure 3.4. Mean electrical conductivity measured in the vertical dipole orientation at each monitoring site was consistently more conductive than the corresponding measurement with the horizontal dipole orientation, indicating persistently less conductive conditions in the vicinity of the surface throughout the monitoring period. In addition, the magnitude of the seasonal variation in apparent conductivity is greater for the horizontal dipole orientation than the vertical dipole orientation. This greater fluctuation indicates that the impact of seasonal soil moisture changes on the in-situ conductivity decrease with depth.

Figure 5.12 compares the mean conductivity values from all three monitoring sites over the entire acquisition period for each dipole orientations. Site 5 gave the least conductive values on each survey date throughout the entire study. During the autumn-winter-spring period, the most conductive values on each survey date were obtained at Site 3. However, the values for Sites 3 and 4 converge during the summer period. These results suggest that while conditions are persistently different at Site 5 relative to the other two sites, differences between Sites 3 and 4 have a seasonal component.

5.3.3 EMI Response to Storm Events

The opportunity to observe the immediate effects of large precipitation events on the EM38 response occurred on two acquisition dates: 27 August 2012 and 04 September 2012. On each occasion, EM38 data was acquired before and after a heavy rainfall event of approximately one hour duration. Based on information obtained the on-site weather station, it was estimated that approximately 26 mm of rain fell during each event. On 27 August 2012, data was acquired at Sites 3, 4 and 5; on 04 September 2012, data was acquired only at Site 3.

Figures 5.13 and 5.14 display the results from the first and second storm event, respectively. Due to the time of year these events occurred, the pre-rainfall data sets have low conductivity characteristic of dry summer conditions. At each monitoring, site the post-precipitation conductivity values along the profile line significantly increased. Since measurements in both acquisition orientations increase, it can be inferred that conductivity increases due to an increased moisture content that is vertically distributed through the near surface. An increase in amplitude of the lateral cyclic component is also noticeable in the post-rainfall data set collected in the vertical dipole orientation. Observations made with a soil probe in visibly crack-free locations found that wetting only extended approximately 1 cm into the subsurface. However, probing into desiccation cracks found wetting extending down over approximately 10 cm at the base of the crack. These observations suggest that this focussed recharge through the desiccation cracks contributes to the vertical changes in moisture observed in these storm events.

5.3.4 Dependence of Conductivity on Soil Moisture

The dependence of the EM38 response on soil moisture conditions was examined by comparing profile mean conductivity data to the gravimetrically-acquired volumetric moisture content data (Figure 3.6). Analogous to the analysis of the resistivity data in Chapter 4, this analysis was performed using log-log plots with a regression based on the commonly-used power law relationship. The results from cross-plotting these two parameters are displayed in Figures 5.15 – 5.20 for each of the different monitoring sites and dipole orientations. Each figure contains three panels that display the results from using three different subsurface intervals for the moisture content data. Panel A compares apparent electrical conductivity to cumulative moisture content data collected from the surface to the depth of 0.25 metres. Similarly, Panel B compares EMI data to moisture content data from the surface to the depth of 0.50 metres and Panel C compares EMI data with moisture content data from surface to the depth of 0.75 metres.

The R^2-values from this analysis vary systematically between different monitoring sites and dipole orientations. Consistently for each monitoring site and dipole orientation, the highest R^2-values for the cross-plotting of these data is obtained for the 0 – 0.50 metre interval. The R^2-values associated with EM38 data acquired in the horizontal dipole orientation are higher than those associated with EM38 data acquired in the vertical dipole orientation for each monitoring site. The lowest R^2-values obtained in either dipole orientation are obtained at Site 4.

5.4 EM31 Results

The EM38 data at Site 3 is supplemented with data from EM31 surveys. The EM31 profiles for both vertical and horizontal dipole data are displayed in Figure 5.21 for the same dates used earlier to present the EM38 data (Figures 5.4 and 5.5). The complete data set for both dipole orientations is displayed in the time-profile plots in Figure 5.22. The complete set of profiles can be found in Appendix A.

A few observations can be made from the individual profiles of the EM31 data. For both dipole orientations, overall apparent conductivity of the individual profiles is highest during wet conditions and lowest during dry conditions. Figure 5.22 shows that lateral variations in apparent conductivity are observable in the EM31 results across the profile at Site 3. The lateral variations in the horizontal dipole orientation data are consistently less than what is observed in the vertical dipole orientation data. In the vertical dipole orientation the magnitude of variations across the profile appears to increase with an increase in overall conductivity.

Mean EM31 apparent conductivity results were calculated to further study the temporal evolution of the EM response. The mean apparent conductivity values are calculated as described in Section 5.3.2. The results are displayed in Figure 5.23 alongside corresponding EM38 mean apparent conductivity results. Considering only the EM31 data, the range of variation in overall apparent conductivity is greater in the horizontal dipole orientation that in the vertical dipole orientation (i.e. the vertical dipole orientation is showing much less seasonal variation), indicating that much of the temporal conductivity variation is occurring above the depth range where the EM31 vertical dipole orientation is most sensitive. The relative magnitude of the mean apparent conductivity measured with the EM31 between dipole orientations varies throughout an annual cycle. The inversion of the two modes – when apparent conductivity is greater in the vertical dipole orientation than in the horizontal dipole orientation – occurs during the summer months, which is associated with dry subsurface conditions. During the second annual cycle of data acquisition, the inversion occurs at an earlier point in the year (24 May 2012 compared to 04 July 2011), which is consistent with the weather data showing the 2012 year was drier than 2011.

Analyzing the range in seasonal variation of the mean apparent conductivity values (Figures 5.23) provides insight into the depths of temporal variations in subsurface conductivity. Comparison of EM31 and EM38 means shows that both vertical and horizontal dipole orientation measurements from the EM38 display more seasonal variations than the EM31 measurements, indicating that a major component of the temporal conductivity variation occurs within the effective depth of investigation of the EM38. From Figure 5.1, this depth can be inferred to be the upper 1.0 metre of the subsurface.

5.5 Conclusions

Similar to the ERT data discussed in Chapter 4, temporal variations in the EM38 profile data and the associated mean profile values show good qualitative agreement with the shallow soil moisture conditions inferred from the gravimetric sampling and weather data. Both dipole orientations give high apparent conductivity values during the wet soil condition during the fall – spring period and low values during the dry soil conditions summer season. The effects of contrasting annual cycles are observed as the relatively lower apparent conductivity values during the drier, warmer summer of 2012 compared to data from the summer of 2011.

The apparent conductivity readings from the horizontal dipole orientation are consistently lower than the concurrent reading from vertical dipole orientation at all three sites. This pattern indicates that there is a persistent near surface zone of lower conductivity conditions, possibly due to vertical variations in soil texture.

The results of the quantitative analysis of the relationship between the EM38 data and soil moisture content derived from gravimetric sampling obtained moderately better correlation coefficient values than the ERT analysis in Chapter 4. The best correlation was obtained for the horizontal dipole orientation over the 0 – 0.50 metre interval; this outcome is due to the nature and differences of the response functions for the two EM38 dipole orientations.

As with the ERT data, EM38 profile data exhibit a cyclic component in the lateral variation of apparent condition values along the survey lines with a spatial wavelength of 2.50 metres at Sites 3, 4 and 5. The amplitude of this cyclic component appears to be a function of soil moisture conditions with the higher amplitude occurring during wet soil periods and becoming significantly smaller during dry period. Further, it can be seen that while this cyclic component is prominent in the vertical dipole data, it has very low amplitude in the horizontal dipole data. Given the nature of the response function of these two dipole orientation, this relative sensitivity implies that the source of the cyclic component is located at a depth below the main sampling zone of the horizontal dipole.

On two occasions, the impact of large, short-term storm events on the soil electrical conductivity were observed using the EM38 device. In both occasions, there was a significant increase in apparent conductivity after the storm event in response to vertical moisture increase due to focussed flow through desiccation cracks.

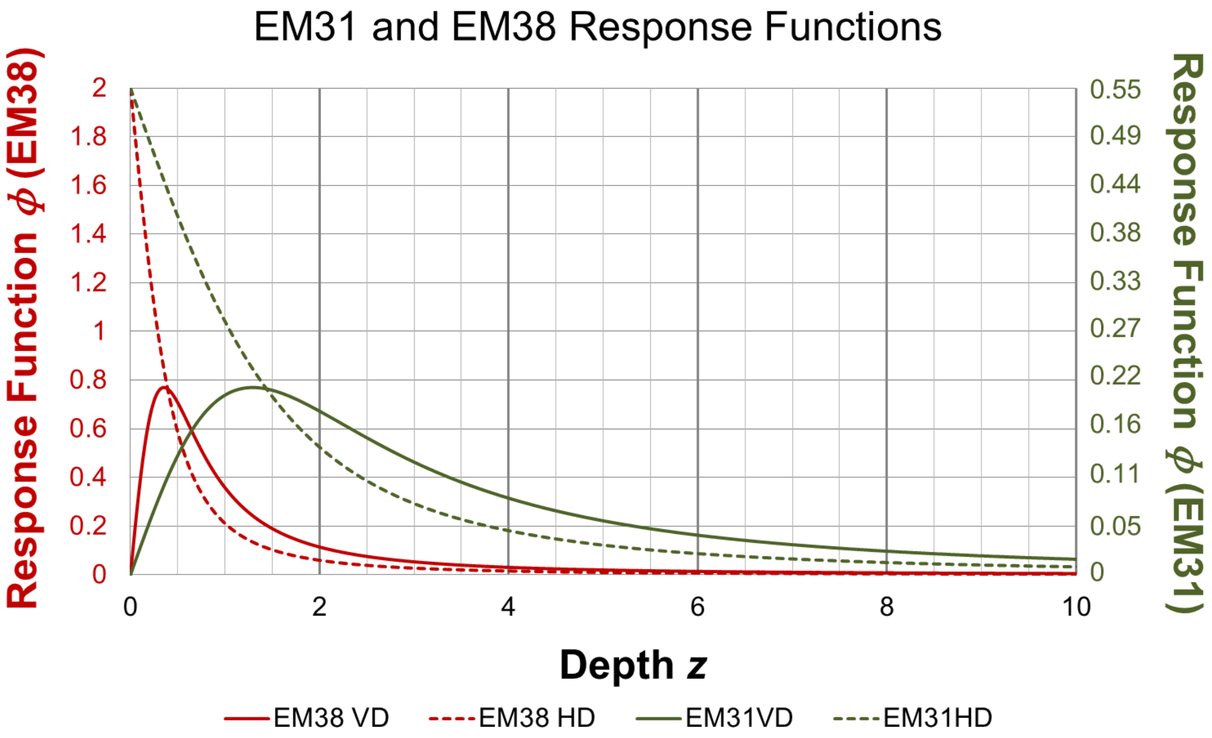

Figure 5.1 – Relative response functions for depths between 0 and 10 metres for the EM38 and EM31 ground conductivity meters in both vertical and horizontal dipole orientations.

Figure 5.2 – Examples of EMI data acquisition using the EM38 and EM31 in both vertical and horizontal dipole orientations. a) EM38 vertical dipole, b) EM38 horizontal dipole, c) EM31 vertical dipole, d) EM31 horizontal dipole.

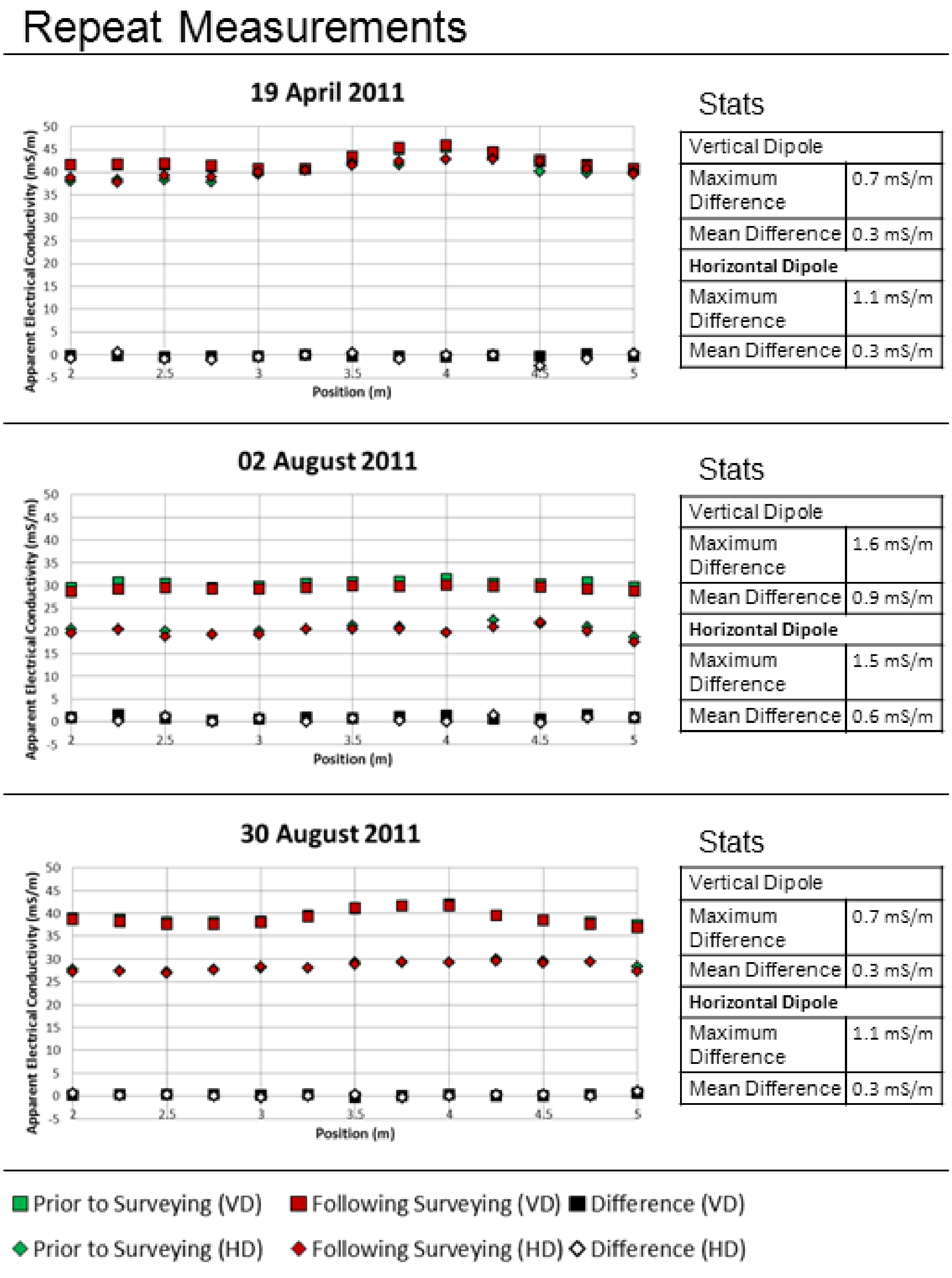

Repeat Measurements

19 April 2011

Stats

Vertical Dipole	
Maximum Difference	0.7 mS/m
Mean Difference	0.3 mS/m
Horizontal Dipole	
Maximum Difference	1.1 mS/m
Mean Difference	0.3 mS/m

02 August 2011

Stats

Vertical Dipole	
Maximum Difference	1.6 mS/m
Mean Difference	0.9 mS/m
Horizontal Dipole	
Maximum Difference	1.5 mS/m
Mean Difference	0.6 mS/m

30 August 2011

Stats

Vertical Dipole	
Maximum Difference	0.7 mS/m
Mean Difference	0.3 mS/m
Horizontal Dipole	
Maximum Difference	1.1 mS/m
Mean Difference	0.3 mS/m

Figure 5.3 – Results of EM38 drift testing performed at Site 3 prior to and following daily surveying on three acquisition dates.

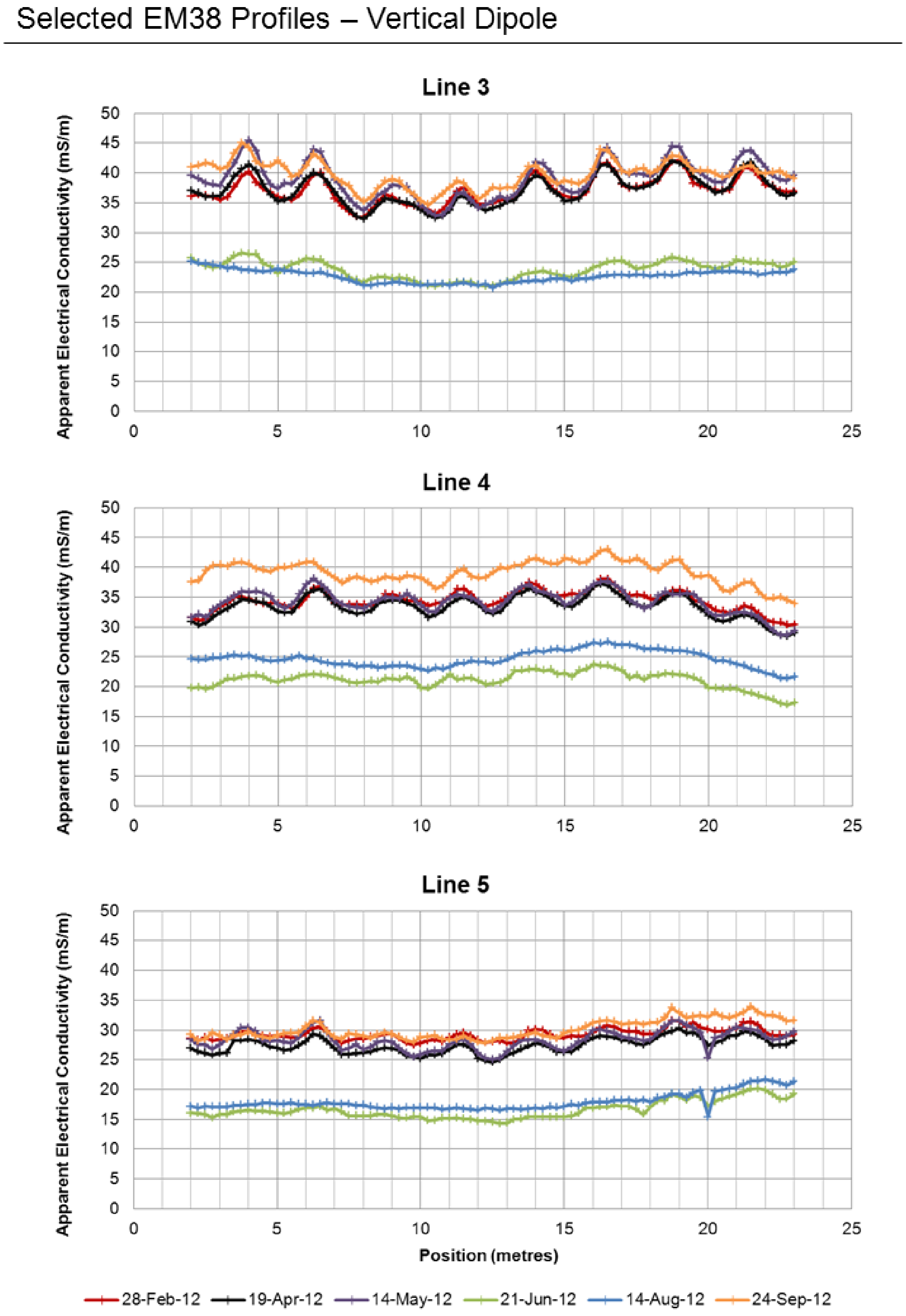

Figure 5.4 – EM38 profiles collected in the vertical dipole orientation at each monitoring site for six selected dates representing a range of seasonal soil moisture conditions.

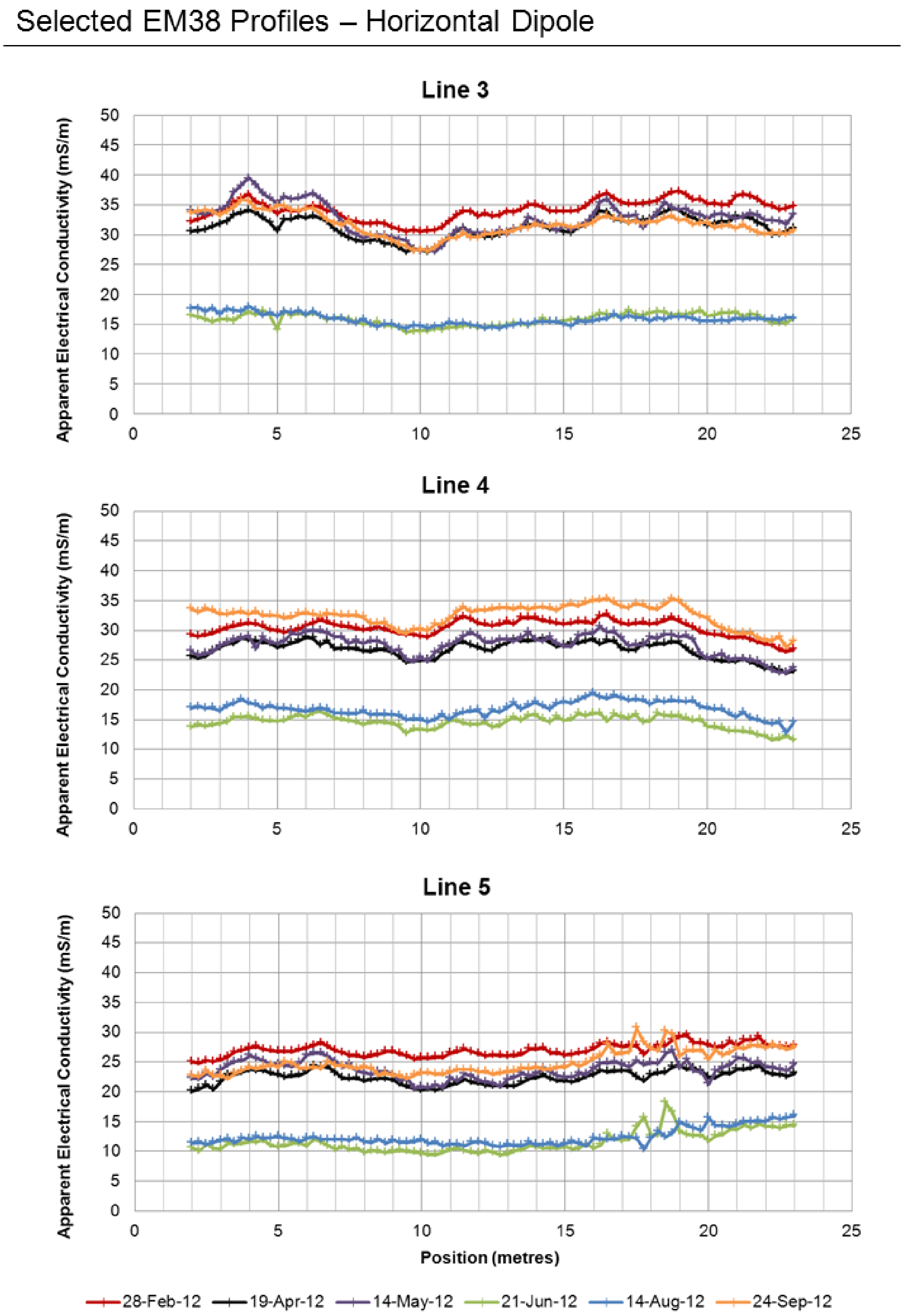

Figure 5.5 – EM38 profiles collected in the horizontal dipole orientation at each monitoring site for six selected dates representing a range of seasonal soil moisture conditions.

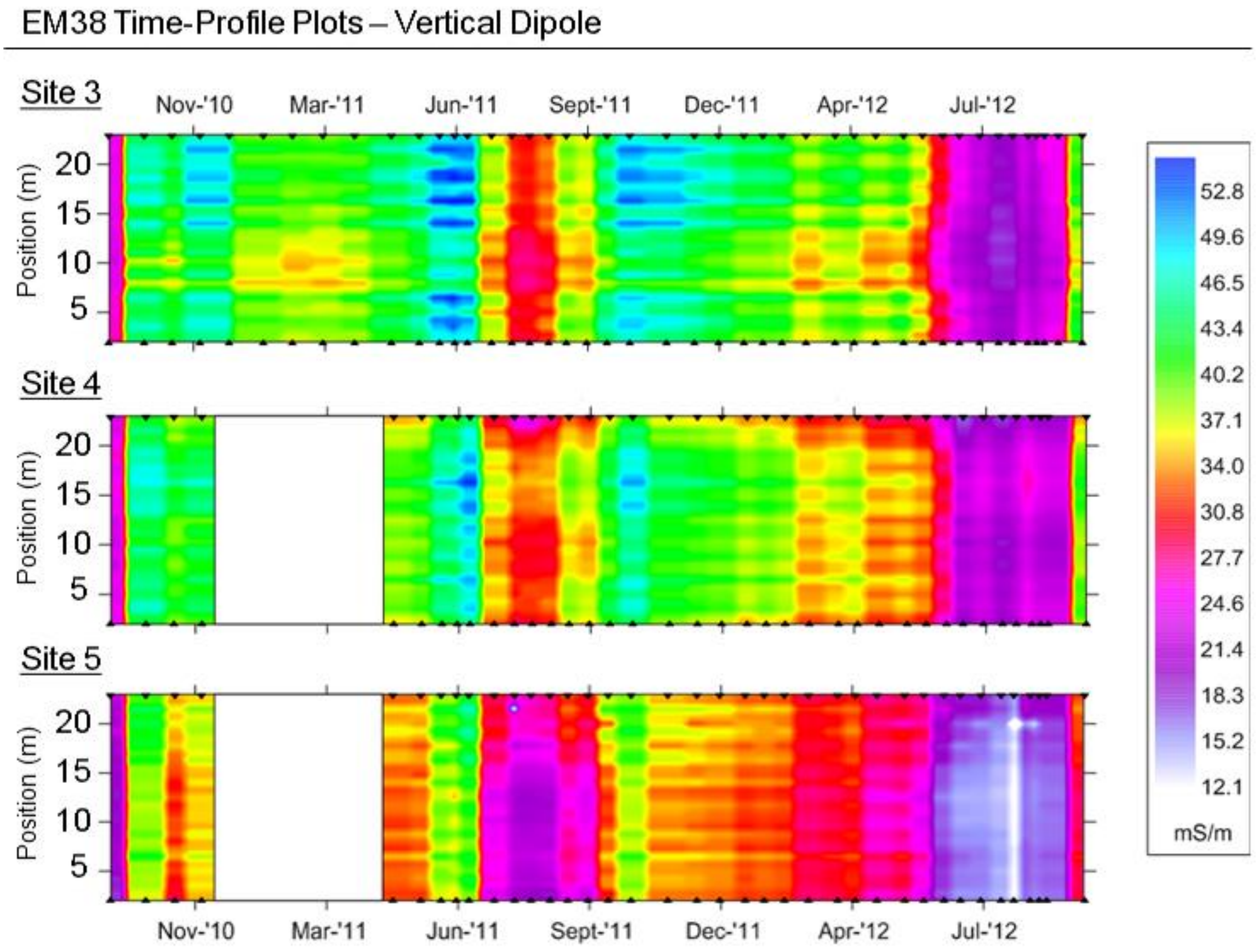

Figure 5.6 – Time-profile plots of EM38 vertical dipole orientation data at each of the three monitoring sites. White gaps represent period of no data collected at Sites 4 and 5. The black triangles represent the location of acquisition dates along the time-axis.

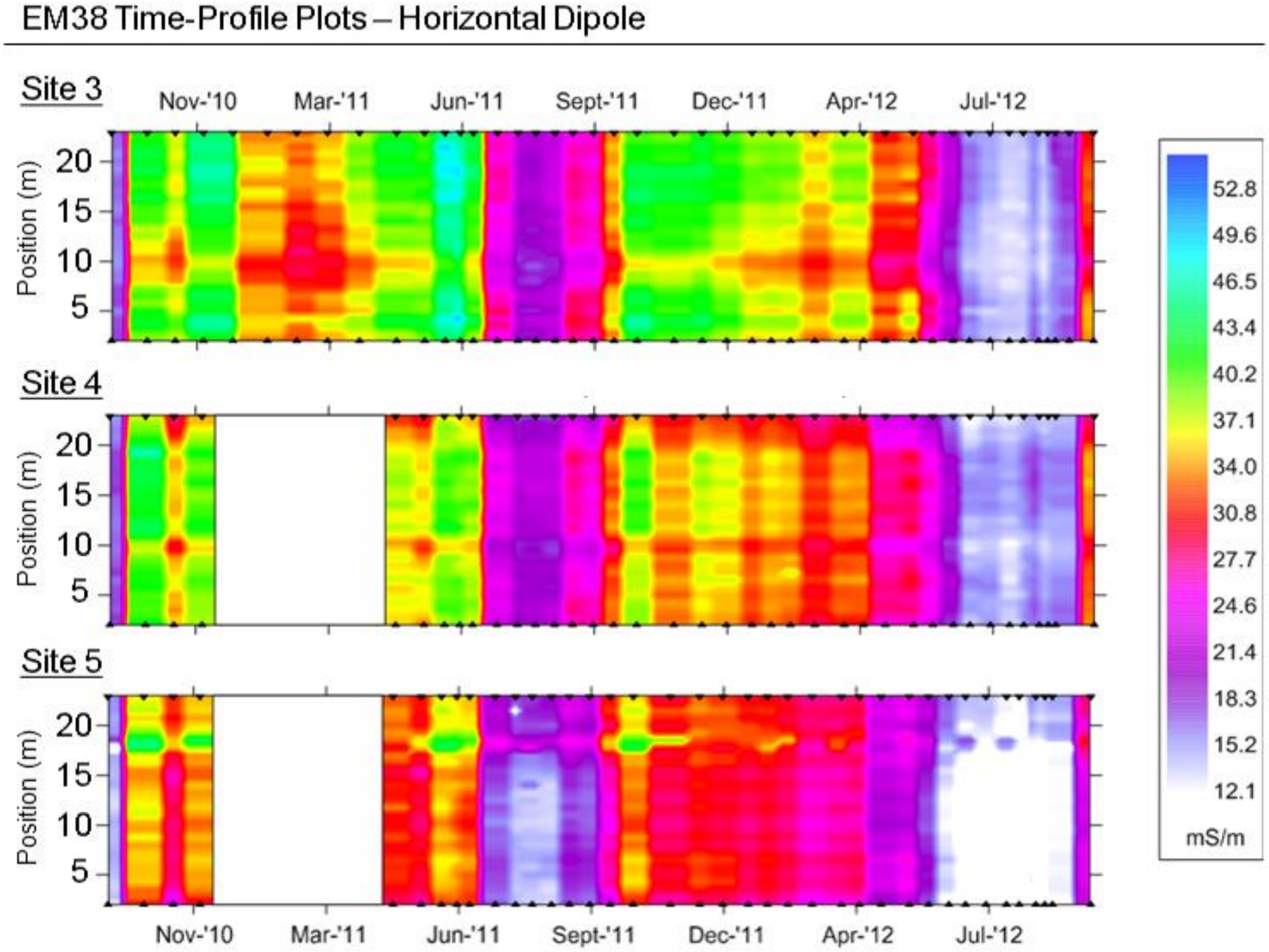

Figure 5.7 – Time-profile plots of EM38 horizontal dipole orientation data at each of the three monitoring sites. White gaps represent period of no data collected at Sites 4 and 5. The black triangles represent the location of acquisition dates along the time-axis.

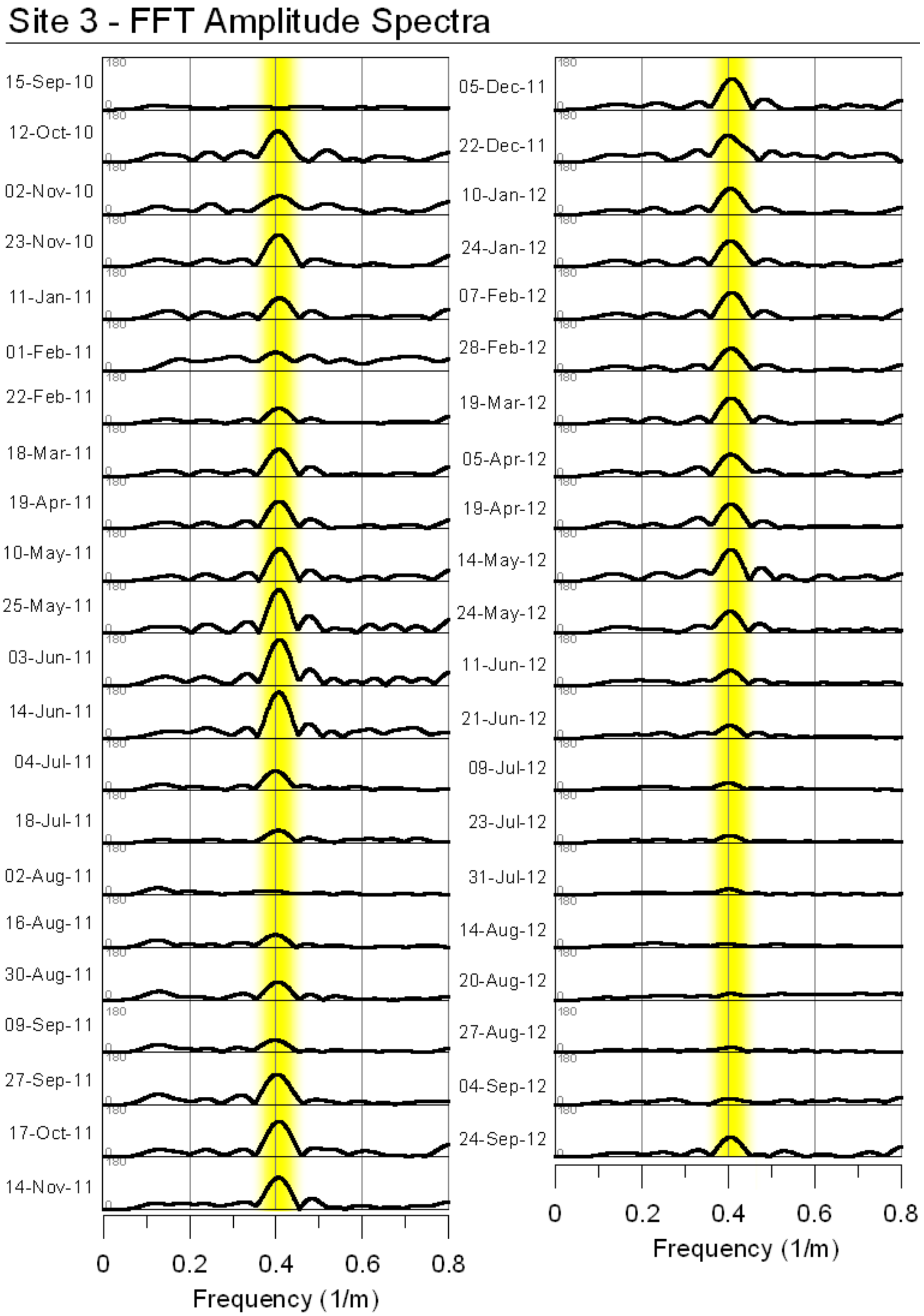

Figure 5.8 – FFT amplitude spectra for EM38 vertical dipole profile data at Site 3. The yellow highlights the 0.4 m^{-1} spatial frequency component.

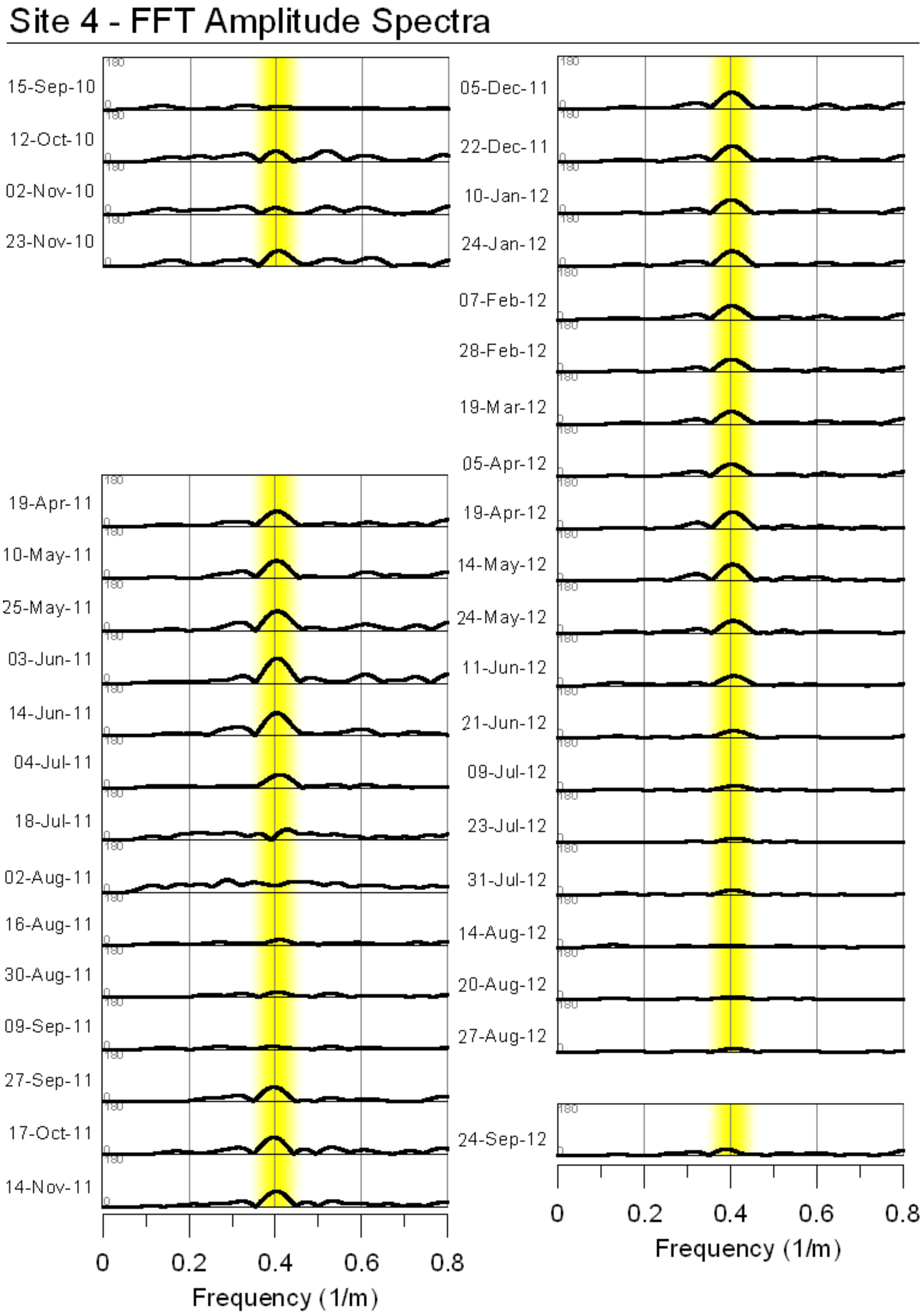

Figure 5.9 – FFT amplitude spectra for EM38 vertical dipole profile data at Site 4. The yellow highlights the 0.4 m^{-1} spatial frequency component. Data gap is present at times of no data collection at this site.

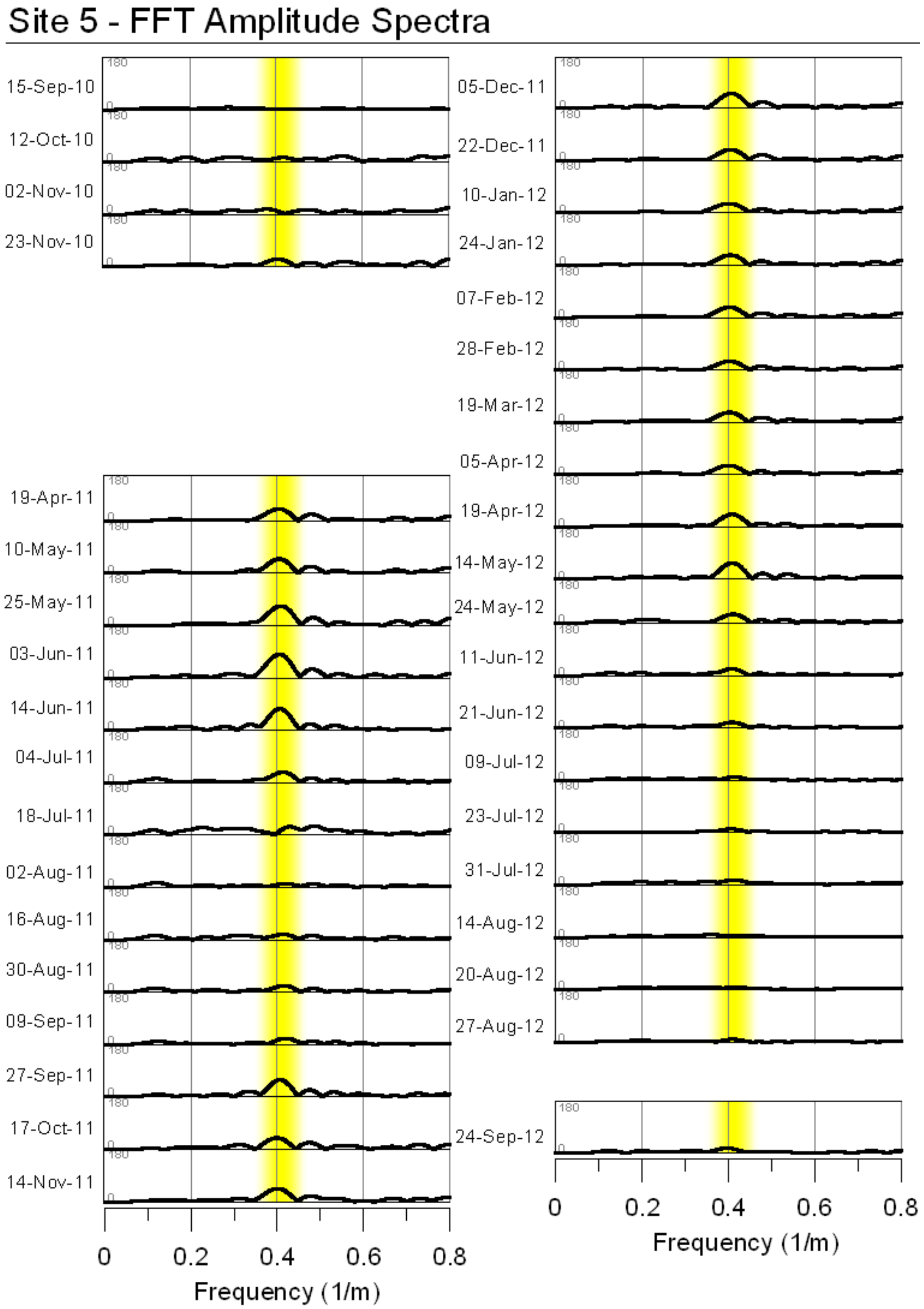

Figure 5.10 – FFT amplitude spectra for EM38 vertical dipole profile data at Site 5. The yellow highlights the 0.4 m^{-1} spatial frequency component. Data gap is present at times of no data collection at this site.

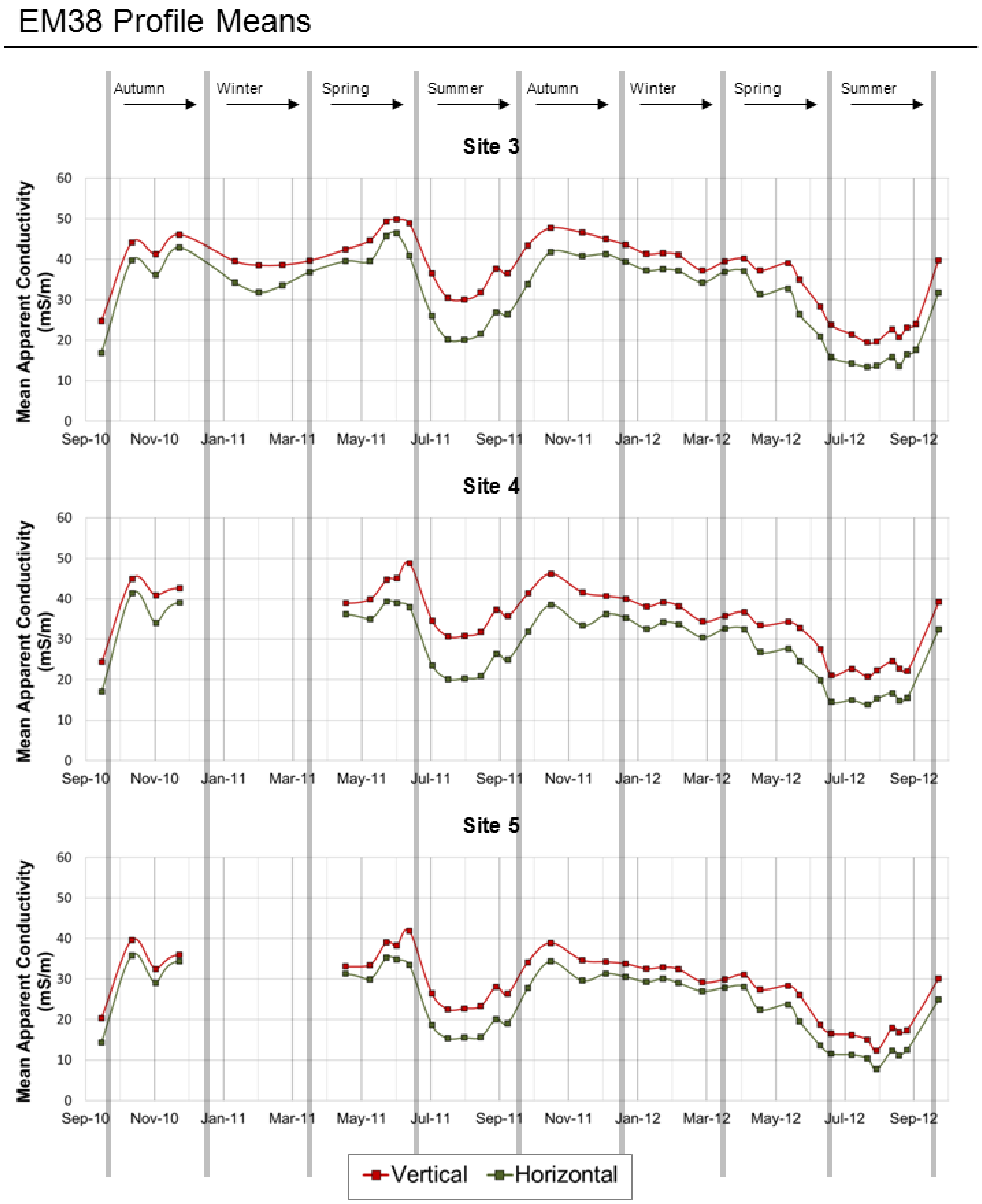

Figure 5.11 – EM38 profile means over the course of the study period at Sites 3, 4 and 5 in both vertical and horizontal dipole orientations.

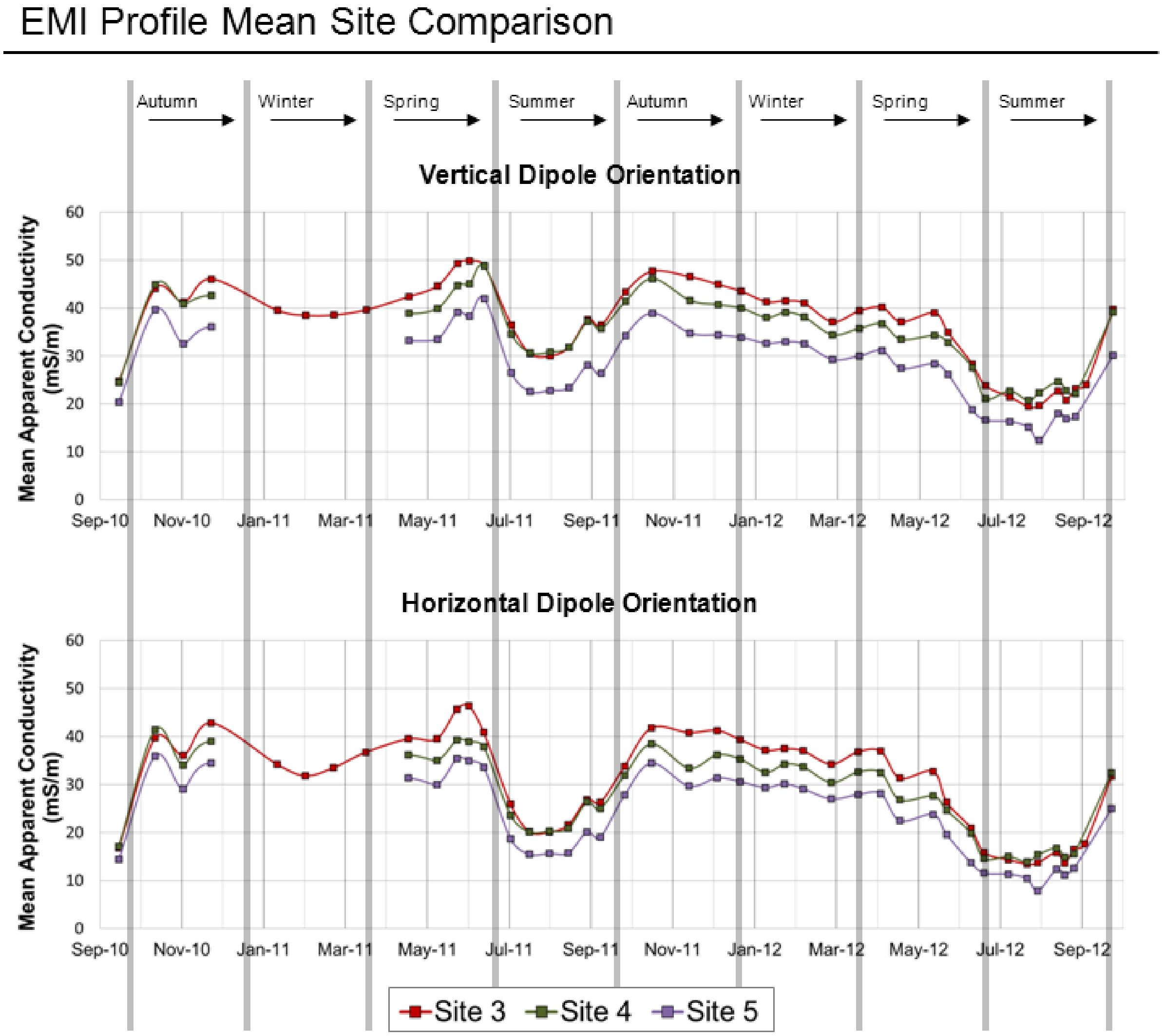

Figure 5.12 – EM38 profile means compared between each monitoring site in each dipole orientations.

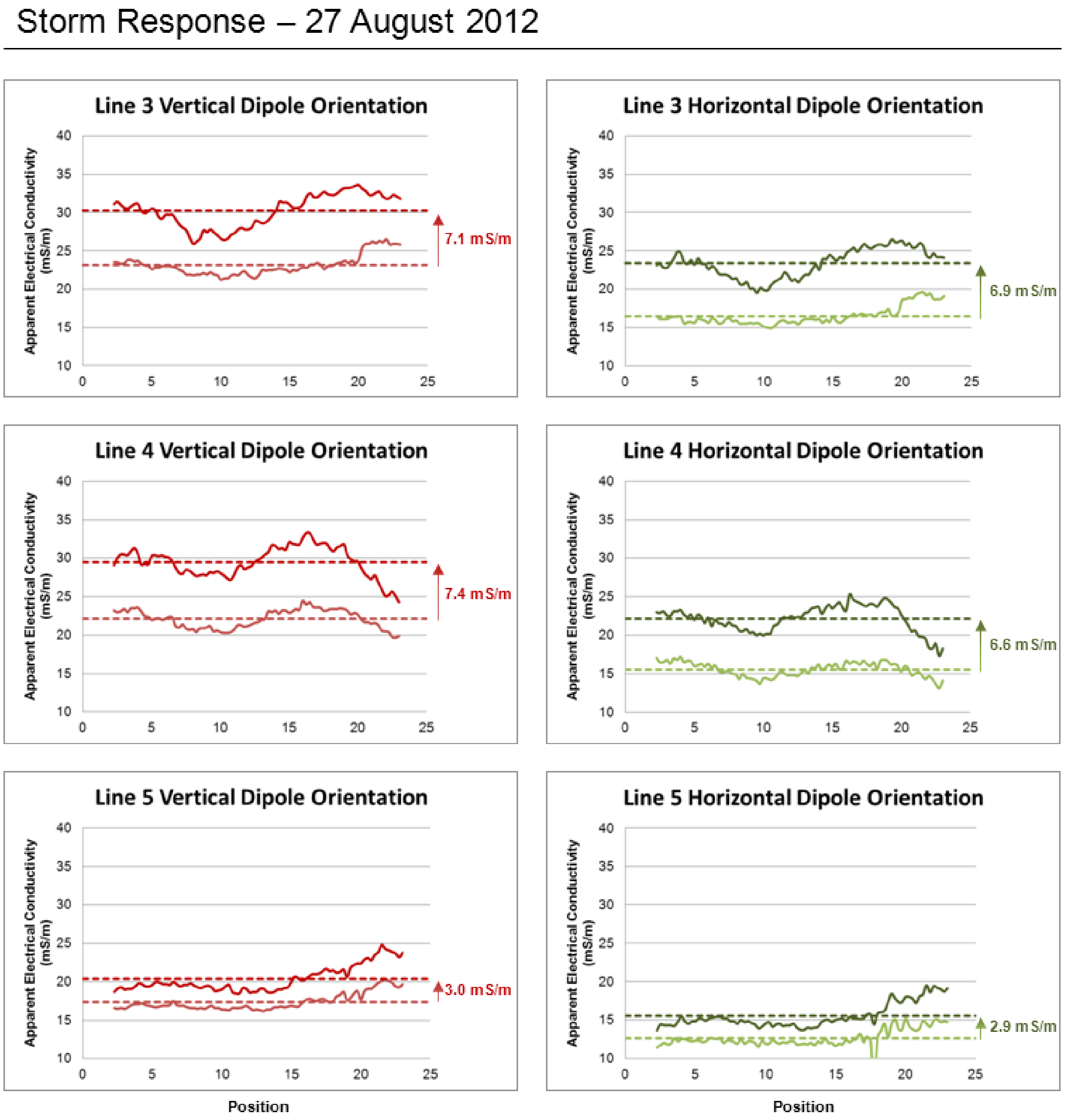

Figure 5.13 – Results of the storm-response study for 27 August 2012. Plots show apparent conductivity profiles before (lower conductivity) and after (high conductivity) the rainfall event, as well as the average (dotted line) for each profile and the amount of conductivity increase observed (beside arrow).

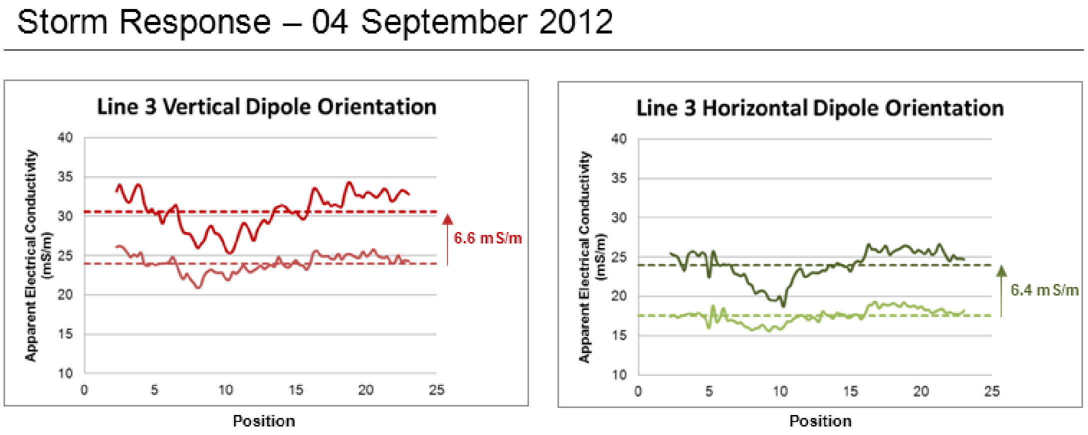

Figure 5.14 – Results of the storm-response study for 04 September 2012. Plots show apparent conductivity profiles before (lower conductivity) and after (high conductivity) the rainfall event, as well as the average (dotted line) for each profile and the amount of conductivity increase observed (beside arrow).

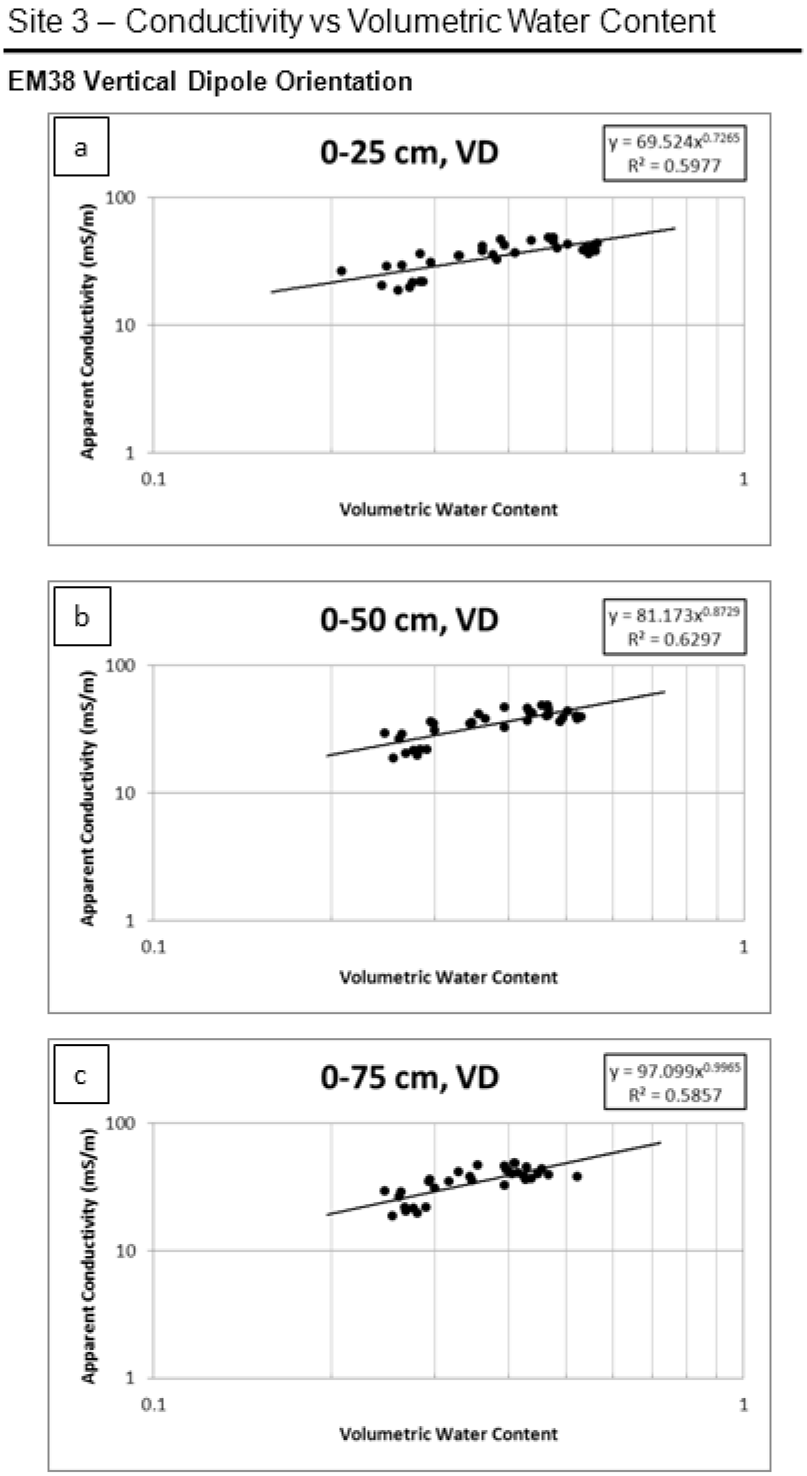

Figure 5.15 – Comparison of averaged apparent electrical conductivity values obtained from EM38 vertical dipole surveys to volumetric water content data for three depth intervals at Site 3.

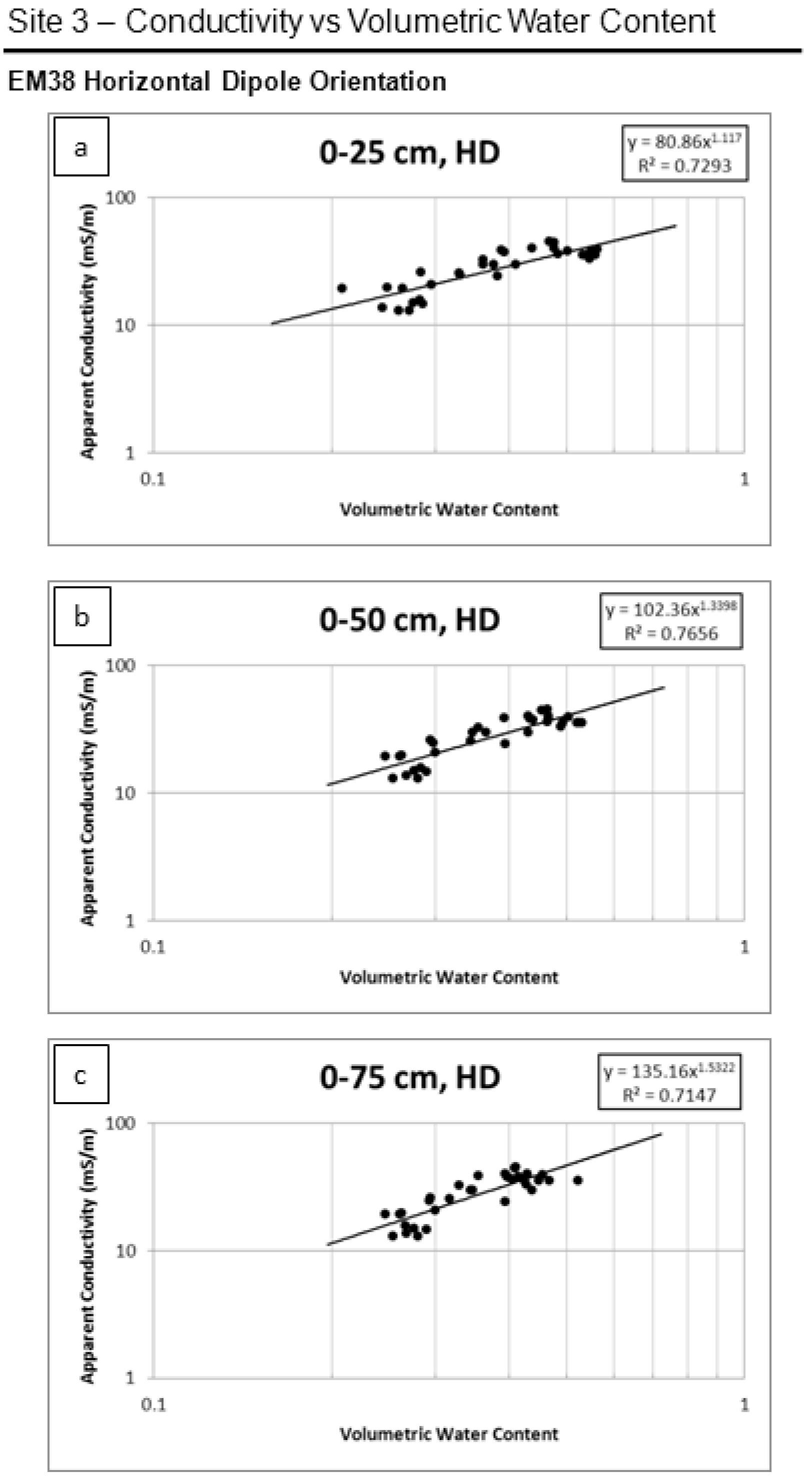

Figure 5.16– Comparison of averaged apparent electrical conductivity values obtained from EM38 horizontal dipole surveys to volumetric water content data for three depth intervals at Site 3.

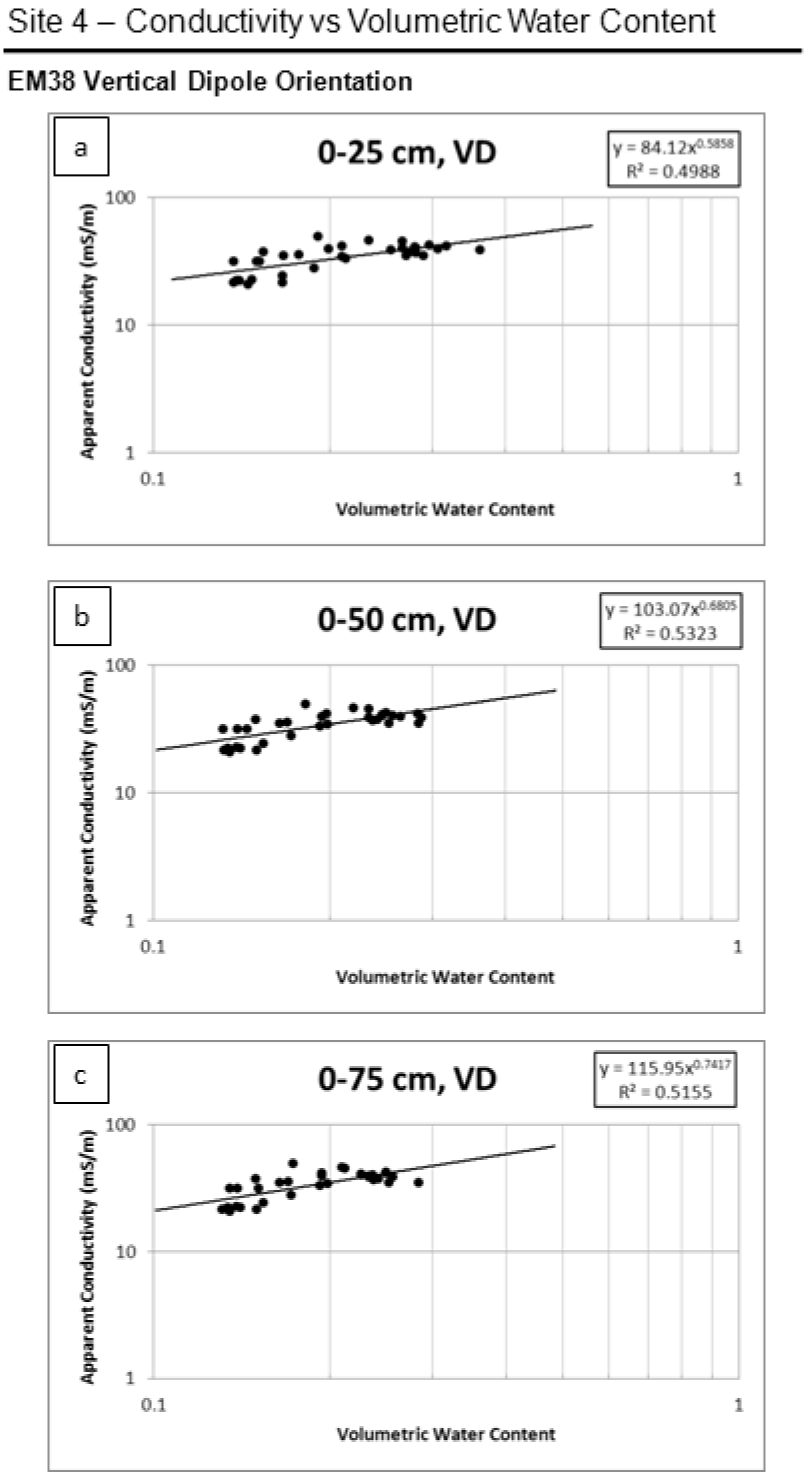

Figure 5.17 – Comparison of averaged apparent electrical conductivity values obtained from EM38 vertical dipole surveys to volumetric water content data for three depth intervals at Site 4.

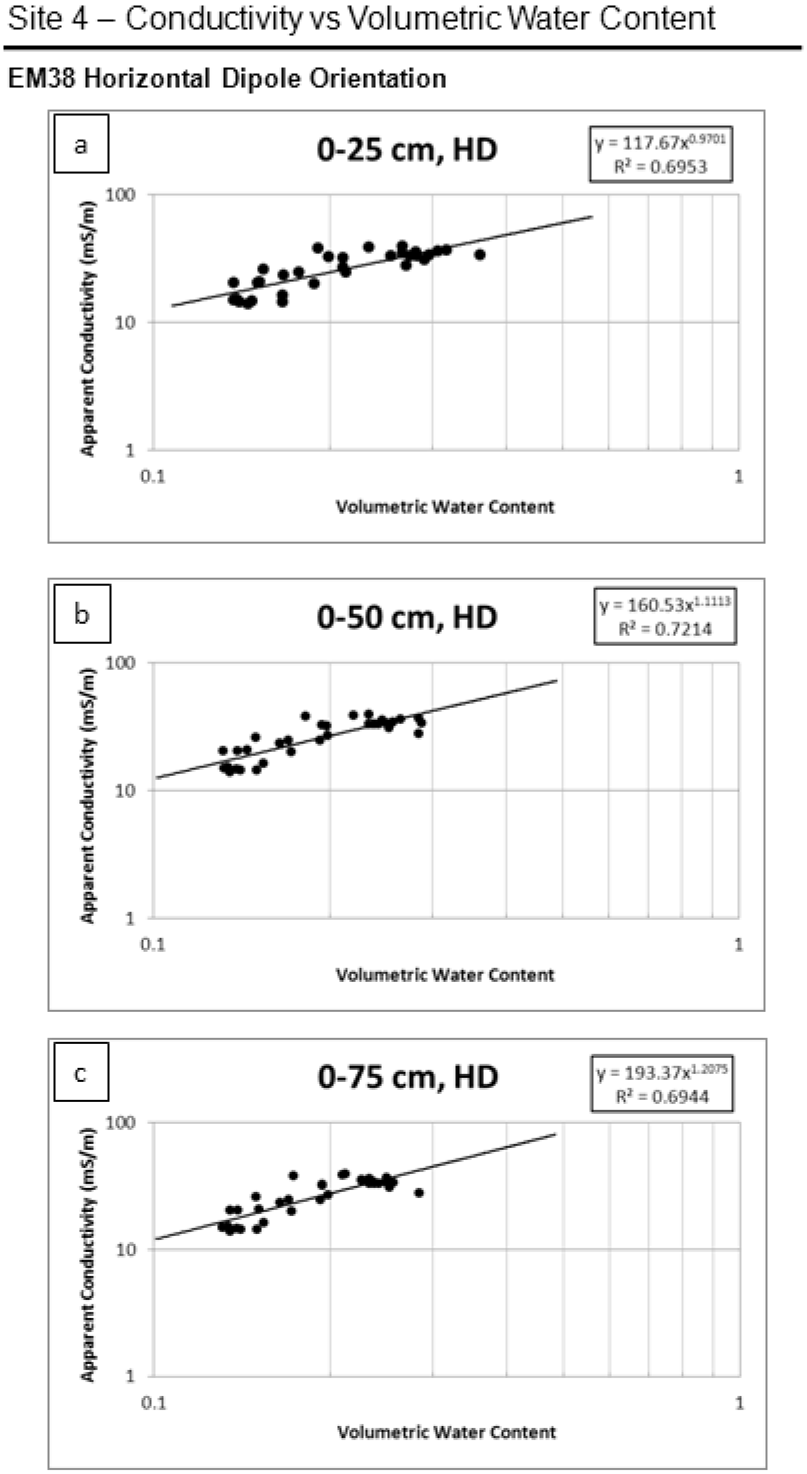

Figure 5.18 – Comparison of averaged apparent electrical conductivity values obtained from EM38 horizontal dipole surveys to volumetric water content data for three depth intervals at Site 4.

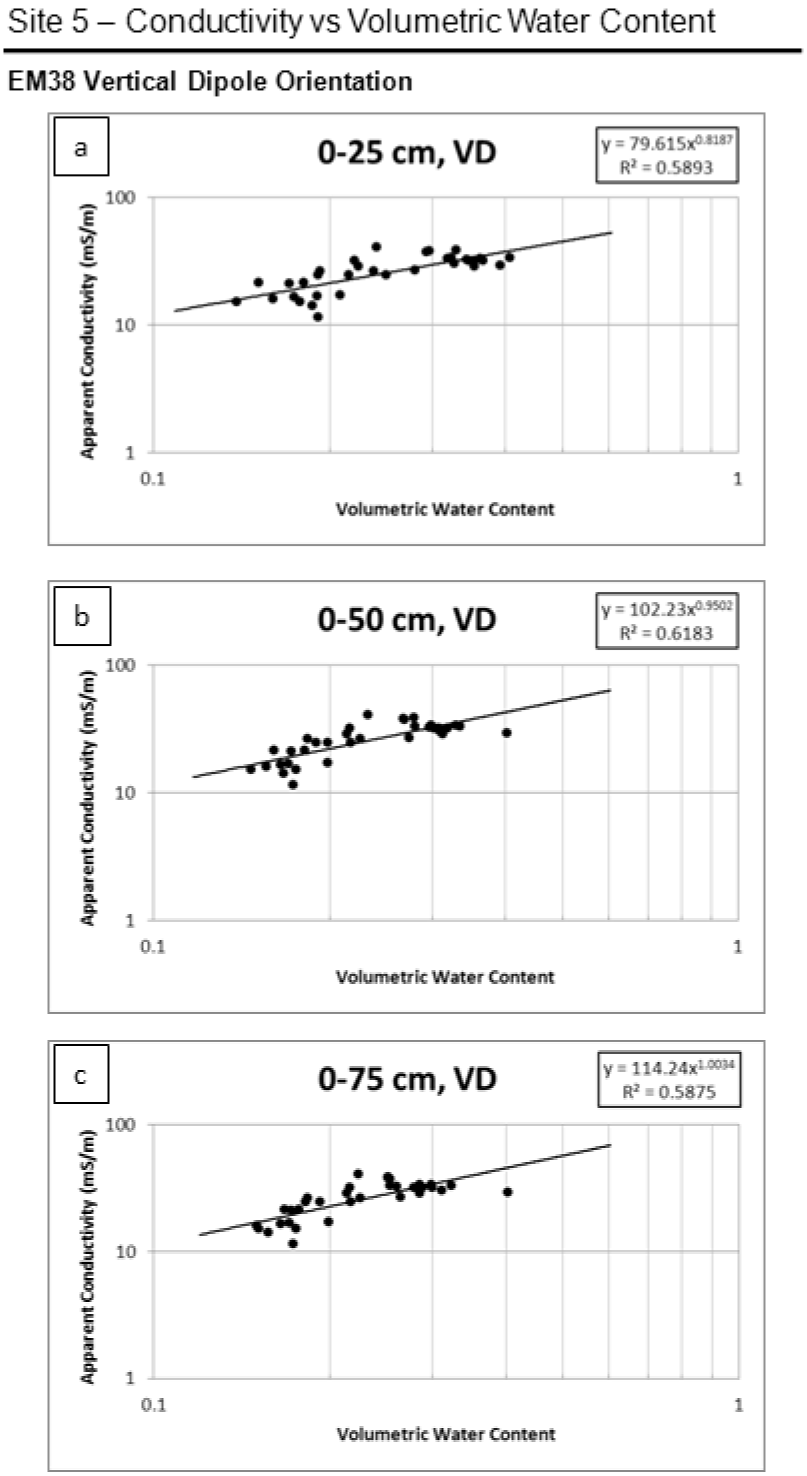

Figure 5.19 – Comparison of averaged apparent electrical conductivity values obtained from EM38 vertical dipole surveys to volumetric water content data for three depth intervals at Site 5.

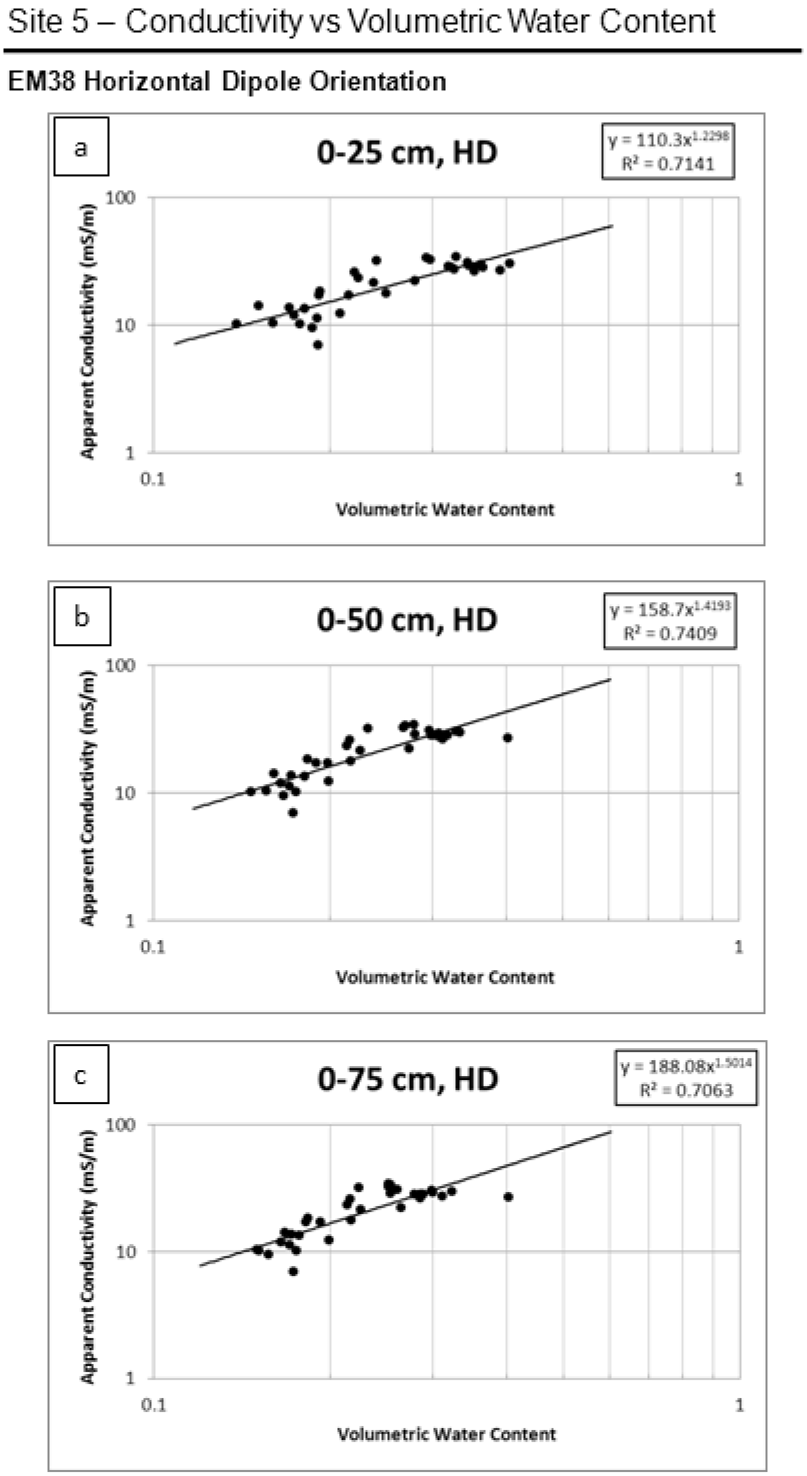

Figure 5.20 – Comparison of averaged apparent electrical conductivity values obtained from EM38 horizontal dipole surveys to volumetric water content data for three depth intervals at Site 5.

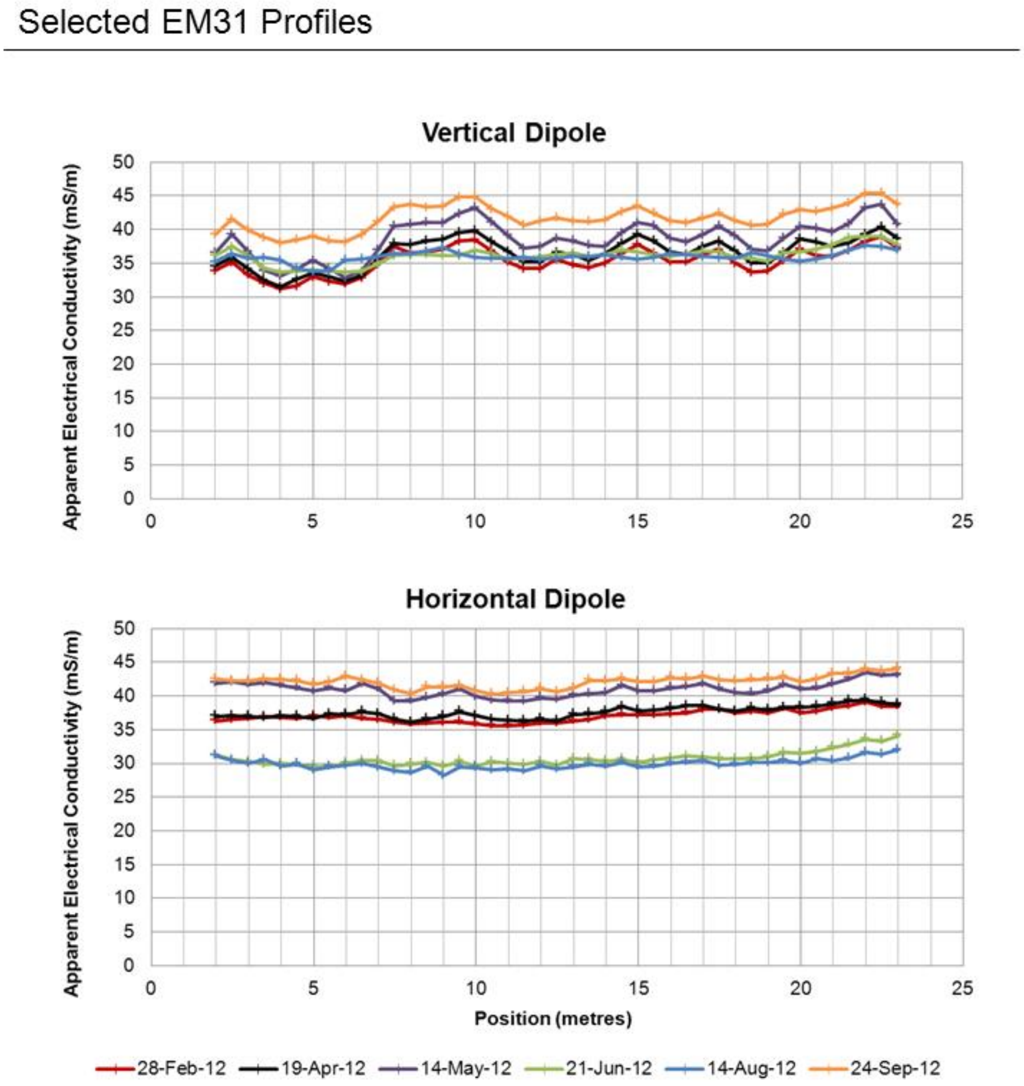

Figure 5.21 – EM31 profiles collected in both dipole orientations at each monitoring site for six selected dates representing a range of seasonal soil moisture conditions.

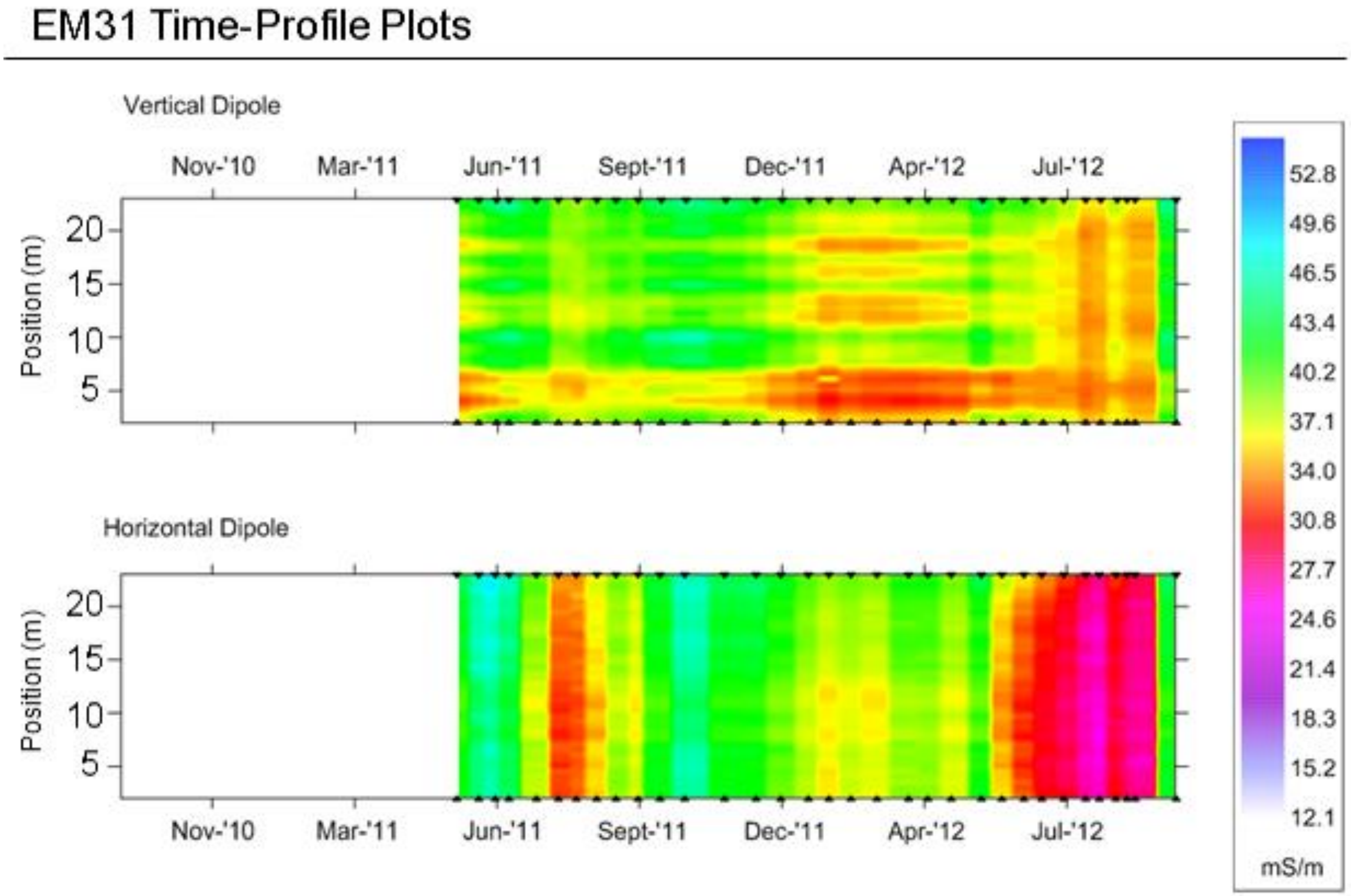

Figure 5.22 – Time-profile plots of EM31 data for both dipole orientations. The black triangles represent the location of acquisition dates along the time-axis. White gaps correspond to dates when data was not acquired.

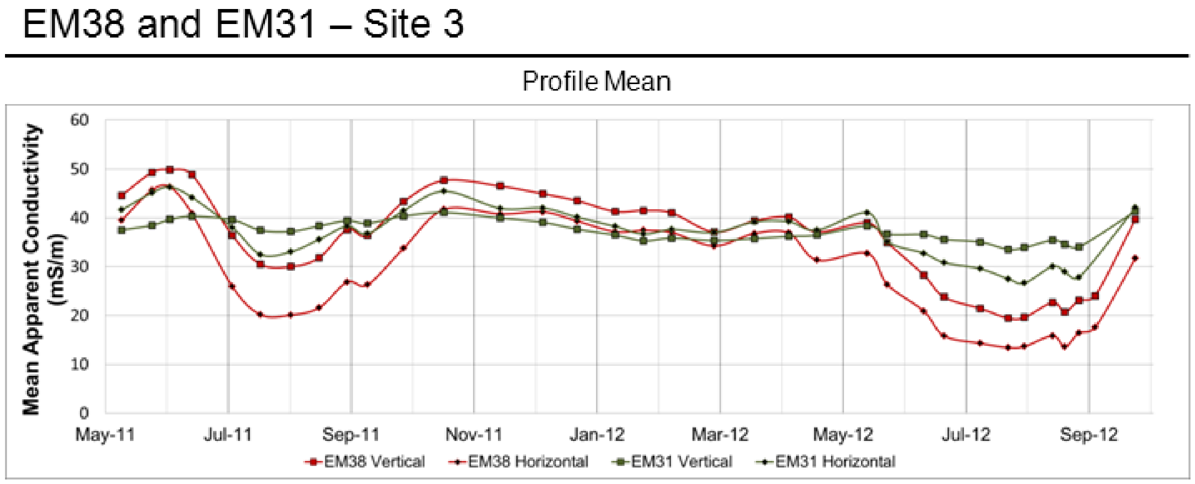

Figure 5.23 – Comparison of mean electrical conductivity values acquired with EM31 and EM38 devices at Site 3 during period of EM31 data acquisition.

Table 5.1 – Dates and summary of EMI data acquisition for each of the 43 acquisition days.

Acquisition Day #	Date	Days since initial	Days since previous	EM38	EM31	Notes
1	15 September 2010	0	-	YES	NO	
2	12 October 2010	27	27	YES	NO	
3	02 November 2010	48	21	YES	NO	
4	23 November 2010	69	21	YES	NO	
5	15 December 2010	91	22	NO	NO	
6	11 January 2011	118	27	YES	NO	Only at Site 3
7	01 February 2011	139	21	YES	NO	Only at Site 3
8	22 February 2011	160	21	YES	NO	Only at Site 3
9	18 March 2011	184	24	YES	NO	Only at Site 3
10	19 April 2011	216	32	YES	NO	
11	10 May 2011	237	21	YES	YES	
12	25 May 2011	252	15	YES	YES	
13	03 June 2011	261	9	YES	YES	
14	14 June 2011	272	11	YES	YES	
15	04 July 2011	292	20	YES	YES	
16	18 July 2011	306	14	YES	YES	
17	02 August 2011	321	15	YES	YES	
18	16 August 2011	335	14	YES	YES	
19	30 August 2011	349	14	YES	YES	
20	09 September 2011	359	10	YES	YES	
21	27 September 2011	377	18	YES	YES	
22	17 October 2011	397	20	YES	YES	
23	14 November 2011	425	28	YES	YES	
24	05 December 2011	446	21	YES	YES	
25	22 December 2011	463	17	YES	YES	
26	10 January 2012	482	19	YES	YES	
27	24 January 2012	496	14	YES	YES	
28	07 February 2012	510	14	YES	YES	
29	28 February 2012	531	21	YES	YES	
30	19 March 2012	551	20	YES	YES	
31	05 April 2012	568	17	YES	YES	
32	19 April 2012	582	14	YES	YES	
33	14 May 2012	607	25	YES	YES	
34	24 May 2012	617	10	YES	YES	
35	11 June 2012	635	18	YES	YES	
36	21 June 2012	645	10	YES	YES	
37	09 July 2012	663	18	YES	YES	
38	23 July 2012	677	14	YES	YES	
39	31 July 2012	685	8	YES	YES	
40	14 August 2012	699	14	YES	YES	
41	20 August 2012	705	6	YES	YES	
42	27 August 2012	712	7	YES	YES	
43	04 September 2012	720	8	YES	NO	Only at Site 3
44	24 September 2012	740	20	YES	YES	

Chapter 6 COMPARISON OF ERT & EMI RESULTS

6.1 Introduction

The responses of both the ERT and EMI techniques are governed by the electrical conductivity structure of the subsurface. Given that these techniques differ in terms of the nature of their underlying physical principles (i.e., galvanic versus electromagnetic induction measurements) and their sensitivity patterns/effective sampling volumes, one would expect both consistencies and discrepancies when comparing the coinciding data sets. In this chapter, coincident data sets acquired during the two year monitoring period at Sites 3, 4 and 5 are compared. For this comparison, the ERT results have been expressed in term of electrical conductivity instead of electrical resistivity that was used previously in Chapter 4. It will be seen that there is significant qualitative agreement between the coincident data sets; however, a quantitative comparison shows substantial differences.

6.2 Comparison of Coincident EM38-ERT Profiles

Figures 6.1 – 6.6 show examples for each site of tomogram results obtained from the ERT data and the coincident EM38 profiles performed using both dipole orientations during wet (03 June 2011) and dry (14 August 2012) soil moisture conditions. As observed in Chapter 4, the region above a depth of 1.50 meters on the ERT tomograms at these three sites can be viewed as a relatively resistive surface layer with a thickness of approximately 0.25 meters overlying a more conductive layer. This conductivity structure is qualitatively consistent with the EM38 profiles that showed apparent conductivity values obtained using the vertical dipole orientation were persistently larger than apparent conductivity values obtained using the horizontal dipole orientation.

During wet periods (Figures 6.1, 6.3 and 6.5), a significant cyclic lateral variation is present in the EM38 vertical dipole profiles and the conductivity structure of the ERT tomograms above a depth of 1 meter. The Fast Fourier Transform analyses performed in Chapters 4 and 5 showed that both the ERT tomograms and EM38 profiles have a well-defined spatial wave-number with a wavelength of 2.5 meters. While this wavelength is consistent with the trellis spacing, the trellises do not extend across the survey lines (their projected intersection points are indicated on the figures). However, the parallel system of drainage tiles buried at the midpoint between the adjoining trellises do cross beneath the monitoring line at each site at depths between 0.3 to 1.0 meters. In addition, the seasonal variation in the strength of this cyclic component (i.e., stronger during the wetter fall-spring period and weaker during the drier summer period) correlates with the expected timing of drainage tile function.

There are also longer-wavelength lateral variations in both data sets. Since these longer wavelength components are low amplitude, they are better seen during dry summer period (Figures 6.2, 6.4 and 6.6) when the 2.5 meter cyclic component is weak. In general, it can be observed that large-scale lateral pattern of high and low conductivity values in the ERT tomograms is reflected in the EM38 profiles.

6.3 Comparison of EM38-ERT Profile Means

In Chapters 4 & 5, mean quantities were generated for each acquisition date to better examine the temporal evolution in these data sets. For the ERT data, depth profiles of mean conductivity for each depth level were obtained by laterally averaging the tomogram results. In the case of the EM38, a mean value for each profile was determined by averaging the readings along the survey line. For consistency, the averaging was performed over the interval between 9.00 to 15.00 meters along the survey line for both the ERT and EM38 data sets. The resulting time series of profile mean values and gravimetric measurements for Sites 3-5 are presented in Figures 6.7 – 6.9 with the weather observations for the monitoring period.

The ERT mean depth profiles at all three sites clearly show that the uppermost 0.25 – 0.50 meters of the subsurface are persistently less conductive than the underlying material to 1.50 meters depth throughout the monitoring period. As previously noted, this conductivity structure is qualitatively consistent with the persistently larger EM38 mean values obtained using the vertical dipole orientation. In addition, it can be seen that the overall level of the conductivity values obtained from the ERT tomogram results at Site 5 are continually lower than the equivalent values at either Site 3 and 4. This relationship between the three sites is also seen in the EM38 profile means (i.e., Figure 5.12).

Further, the conductivity of uppermost 0.25 – 0.50 meters of the subsurface in the ERT mean depth profiles at all three sites display the same temporal pattern of higher conductivity during fall to spring period and lower conductivity during the summer season. This temporal pattern is also observed in the EM38 profile means. This geophysical response coincides with the temporal pattern in soil moisture measurements obtained from gravimetric sampling over the upper 0.50 meter.

Further, the weather observations indicate that 2012 summer period had significantly less precipitation than the 2011 summer period. The effects of the expected drier summer soil conditions are reflected in the greater conductivity reduction seen with the both geophysical methods during the 2012 summer period relative to 2011 summer period. It should be noted that this annual contrast is not apparent in the gravimetric data and could reflect its inability to properly measure the effects of macropores, such as desiccation cracks.

6.4 Quantitative Comparison of the ERT and EM38 Data Sets

As noted in Section 2.3, there is a mathematical relationship that allows the calculation of the apparent conductivity reading of a ground conductivity meter using an electrical conductivity depth profile for a one-dimensional subsurface. This relationship was used in the following manner to perform a quantitative comparison between the EM38 and ERT data obtained in this study. For each monitoring date, the mean conductivity depth profile obtained from the laterally averaged ERT tomogram results were used to calculate the predicted apparent conductivity reading of the EM38 for both the horizontal and vertical dipole orientations. These predicted values are compared with the corresponding EM38 profile mean attained from the laterally averaged readings along the survey line. These profile mean values for the EM38 and ERT data are the quantities shown in Figures 6.7 – 6.9.

The predicted apparent conductivity values are shown as a time series with the actual EM38 mean values for Sites 3, 4 and 5 in Figures 6.10, 6.11 and 6.12, respectively. It can be clearly seen for all three sites that there is significant divergence between the predicted and observed apparent conductivity values during the drier summer period with the observed values being consistently lower than the predictions. Further, this difference is larger for the horizontal dipole orientation at each site. However, there is much less difference between the predicted and observed apparent conductivity values during the wetter fall-spring period. Similar to the summer, the measured values tend to be lower than the predictions and the horizontal dipole orientation has the larger difference.

There are a number of potential sources for the quantitative discrepancies between the ERT and EM38 data sets in contrast to the significant level of consistency in the spatial and temporal patterns observed in these two data sets. Lavoué et al. (2012) has proposed that these differences are due in part to issues regarding the calibration, acquisition procedure and instrumental drift for the EM38. For this study, a regular calibration and data acquisition procedure was carefully followed to address these issues. Further, the low levels of instrumental drift (i.e., less than 1 mS/m over the course of daily EM38 data acquisition) were encountered during this study should reduce the impact of this factor. It can also be argued that the persistently high conductive conditions at Sites 3, 4 and 5 due to the presence of clay-rich soils improved the accuracy of the recommended EM38 calibration process. Therefore, it is anticipated that these issues have been well controlled in this study.

This comparison is based on the assumption of a one-dimensional conductivity depth profile, ignoring the effects of two/three-dimensional conductivity structure in the subsurface. Since both the ERT and EMI data clearly exhibit lateral variability, such as the 2.5 meter cyclic component, it could be asked whether the lateral averaging process sufficiently compensates for the lateral changes. Interestingly, the divergence between the predicted and observed apparent conductivity values is largest during the drier summer period when the least lateral variability is present and smallest during the wetter fall-spring period when the strongest lateral components occur. Hence, the impact of higher dimensional structure on the one-dimension assumption does not appear to be a major cause of the discrepancy between the predictions and observations.

Differences between the response functions for the electrode arrays used to acquire the ERT and the dipole orientations of the EM38 would contribute to discrepancies between the results obtained from these methods for the same subsurface conductivity structure. Work by Roy and Apparao (1971) and Barker (1989) indicate that the response function of a Wenner electrode array for a one-dimensional conductivity depth profile is similar in form to that of vertical dipole orientation and scaled by the current electrode separation. The nature of the electrode array response function would be reflected in the inversion results obtained from the tomography process, leading to progressive less constraints on the ERT predicted conductivity structure as one approaches the ground surface where the response function of the horizontal dipole is primarily weighted. Hence, it could be expected that there would be significant discrepancies between the ERT predictions and horizontal dipole EM38 data when there are major variations in very shallow conductivity depth profile. The gravimetric moisture content data, as well as the observed occurrence of 0.05 – 0.15 meter deep desiccation cracks, provide strong indirect evidence that such conditions occur during the drier summer period when the largest divergence between the ERT predictions and horizontal dipole EM38 data was found.

A final potential source identified for the quantitative discrepancies is the inherent non-uniqueness of the models generated by inverse techniques, such as the tomography process. This non-uniqueness implies that there is an uncertainty associated with the prediction based on the tomogram values used in this comparison. Quantifying this uncertainty would require characterizing the range of subsurface conductivity structures that can generated from the tomography process and is beyond the scope of this study.

6.5 Conclusions

Coincident ERT and EM38 data sets acquired during the two-year monitoring period at Sites 3, 4 and 5 were compared both qualitatively and quantitatively to assess discrepancies in the results of the two geophysical techniques.

Comparison of the geophysical data shows qualitative agreement between the results of the two geophysical techniques both spatially and temporally. Both ERT and EM38 profiles display similar lateral variations that include a well-defined cyclic component of comparable wave-length thought to be due to drainage tile functioning. In addition, the subsurface electrical structure that can be inferred from the mean EM38 profile values is in agreement with the ERT mean depth profiles. Further, the temporal variations observed in the data from these two methods correlates well with shallow soil moisture conditions as observed by gravimetric sampling and inferred from weather data.

In contrast to the qualitative observations, the quantitative comparison between the actual EM38 data and predictions based on the ERT tomography results revealed significant deviations, particularly for the horizontal dipole orientation during dry summer conditions. A number of potential causes for this divergence were discussed with the most probable being differences in the response functions of the Wenner electrode array and the EMI dipoles in a horizontally-layered subsurface.

Site 3 – 03 June 2011

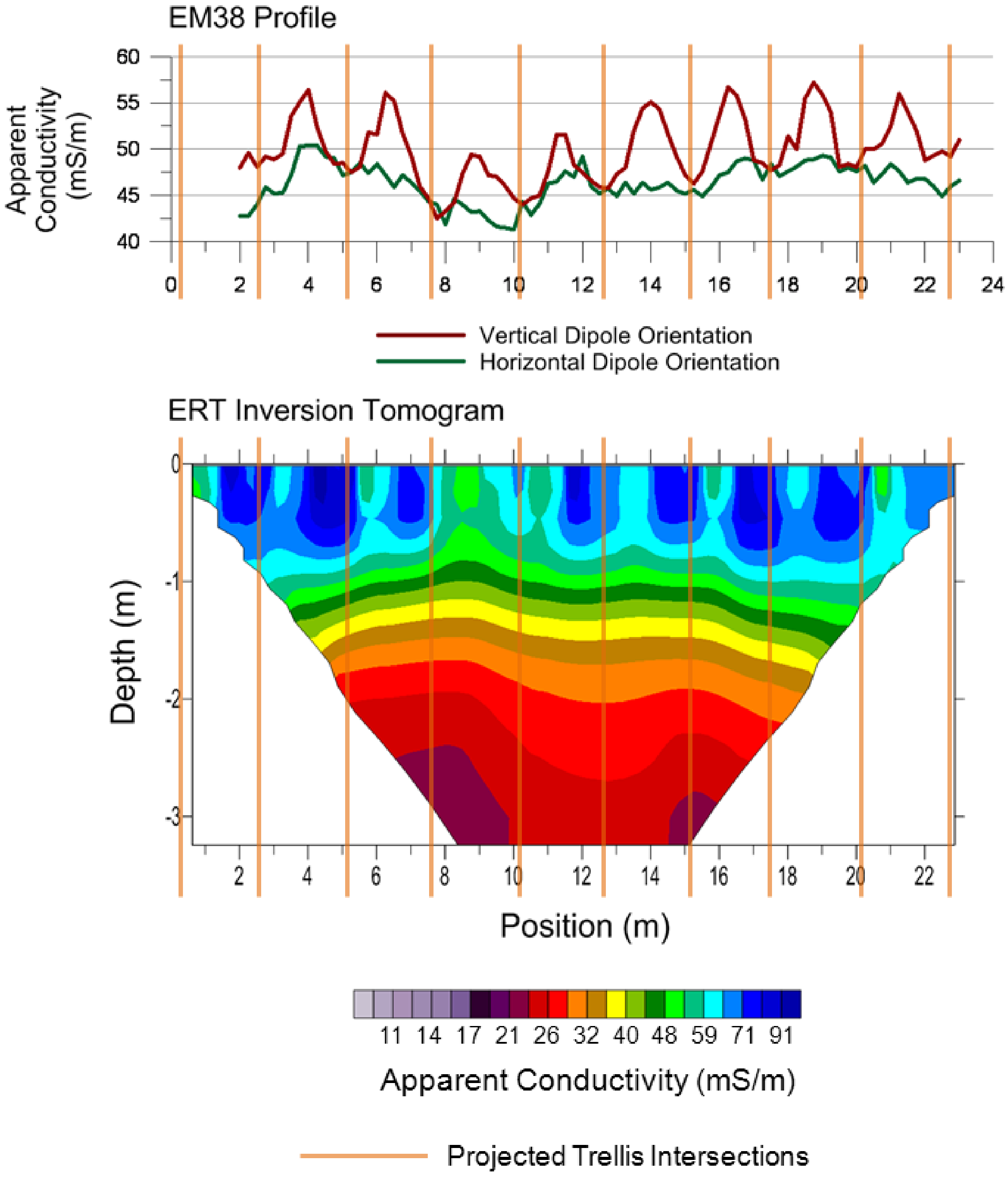

Figure 6.1 –The EM38 profile and the ERT inversion tomogram for Site 3 on 03 June 2011, a day with wet soil conditions and high lateral cyclicity observable. The locations of projected trellis intersections are shown. Drainage tiles exist at the midpoint between projected trellis intersections.

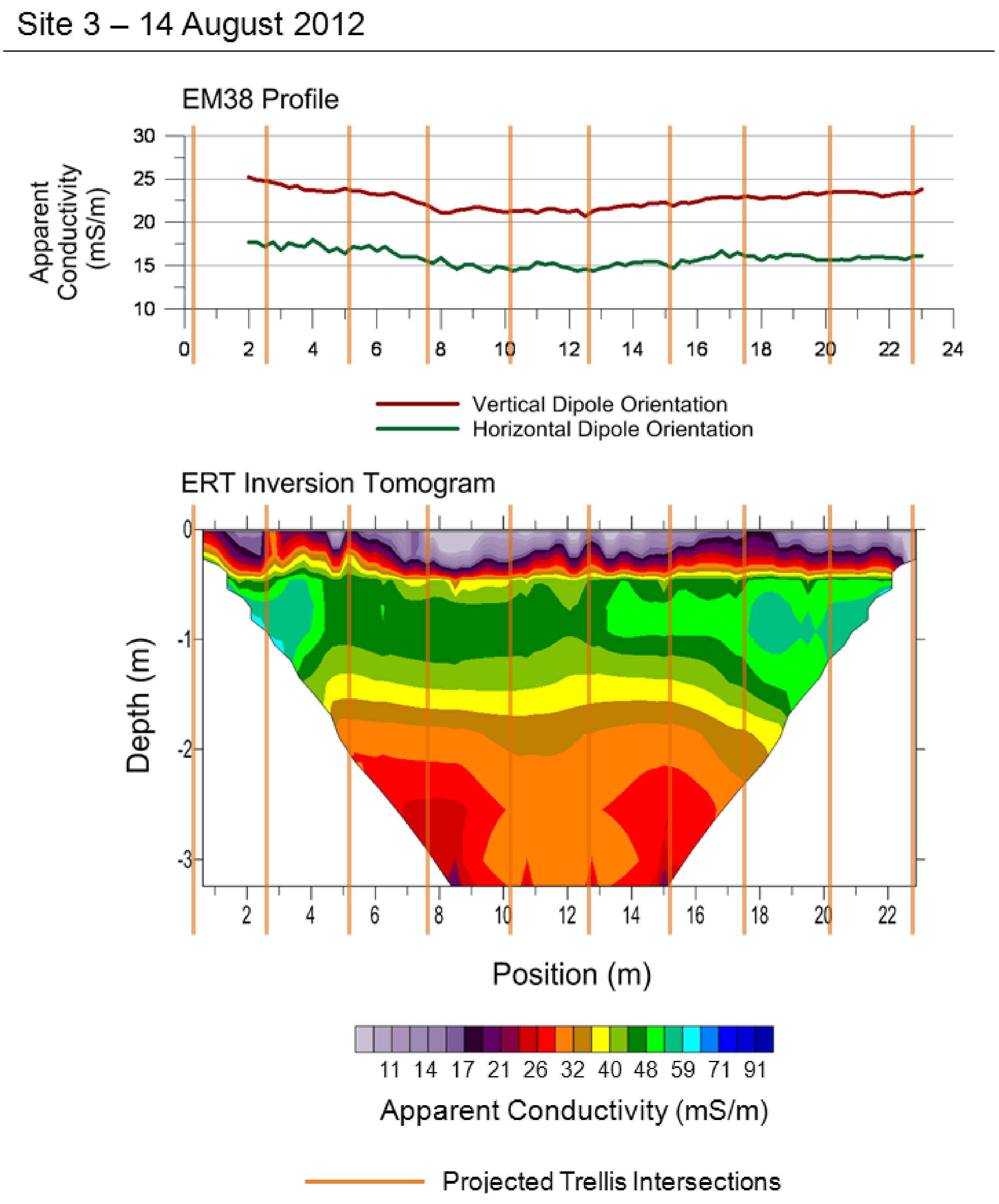

Figure 6.2 –The EM38 profile and the ERT inversion tomogram for Site 3 on 14 August 2012, a day with dry soil conditions and minimal lateral cyclicity observable. The locations of projected trellis intersections are shown. Drainage tiles exist at the midpoint between projected trellis intersections.

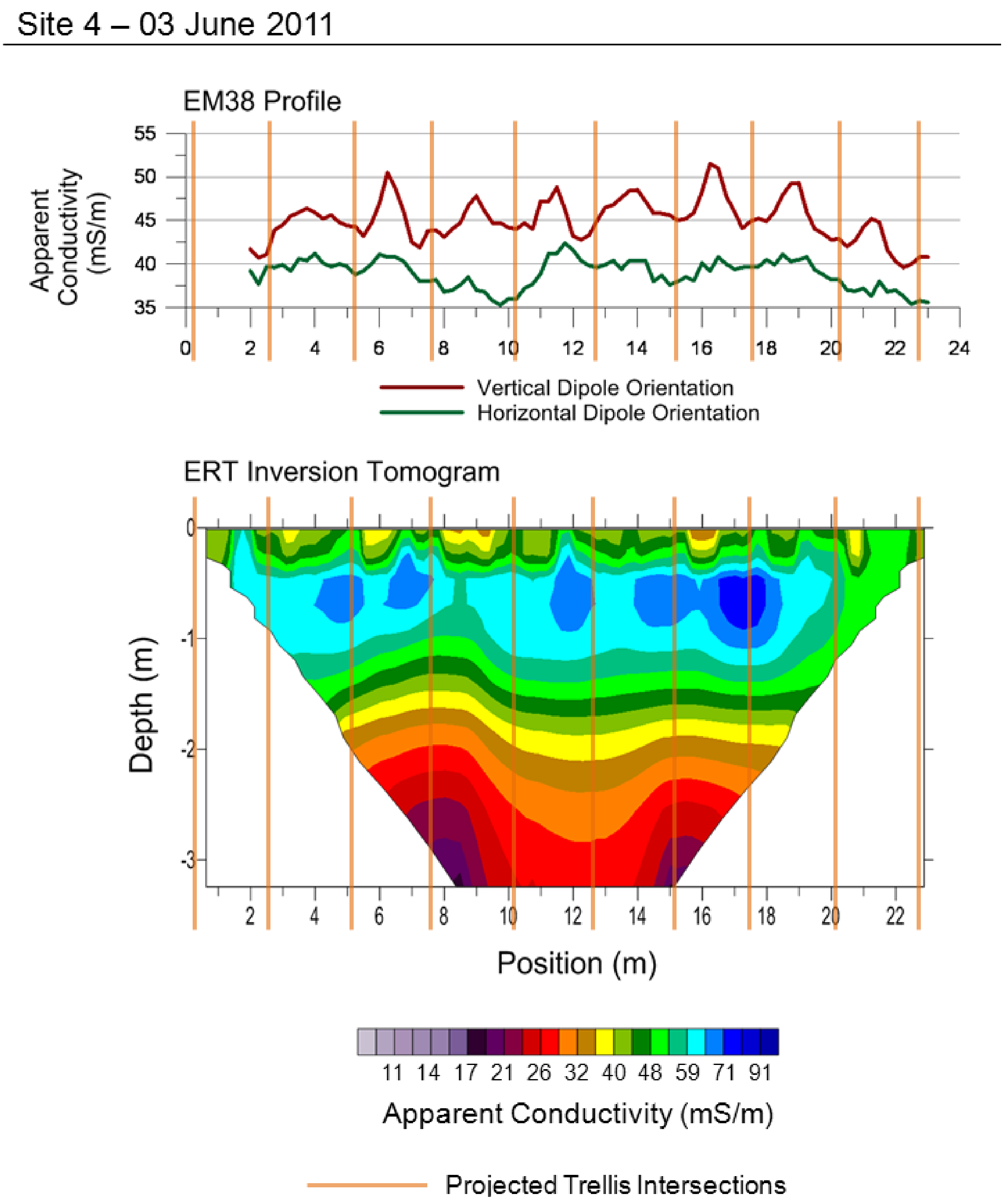

Figure 6.3 –The EM38 profile and the ERT inversion tomogram for Site 4 on 03 June 2011, a day with wet soil conditions and high lateral cyclicity observable. The locations of projected trellis intersections are shown. Drainage tiles exist at the midpoint between projected trellis intersections.

Site 4 – 14 August 2012

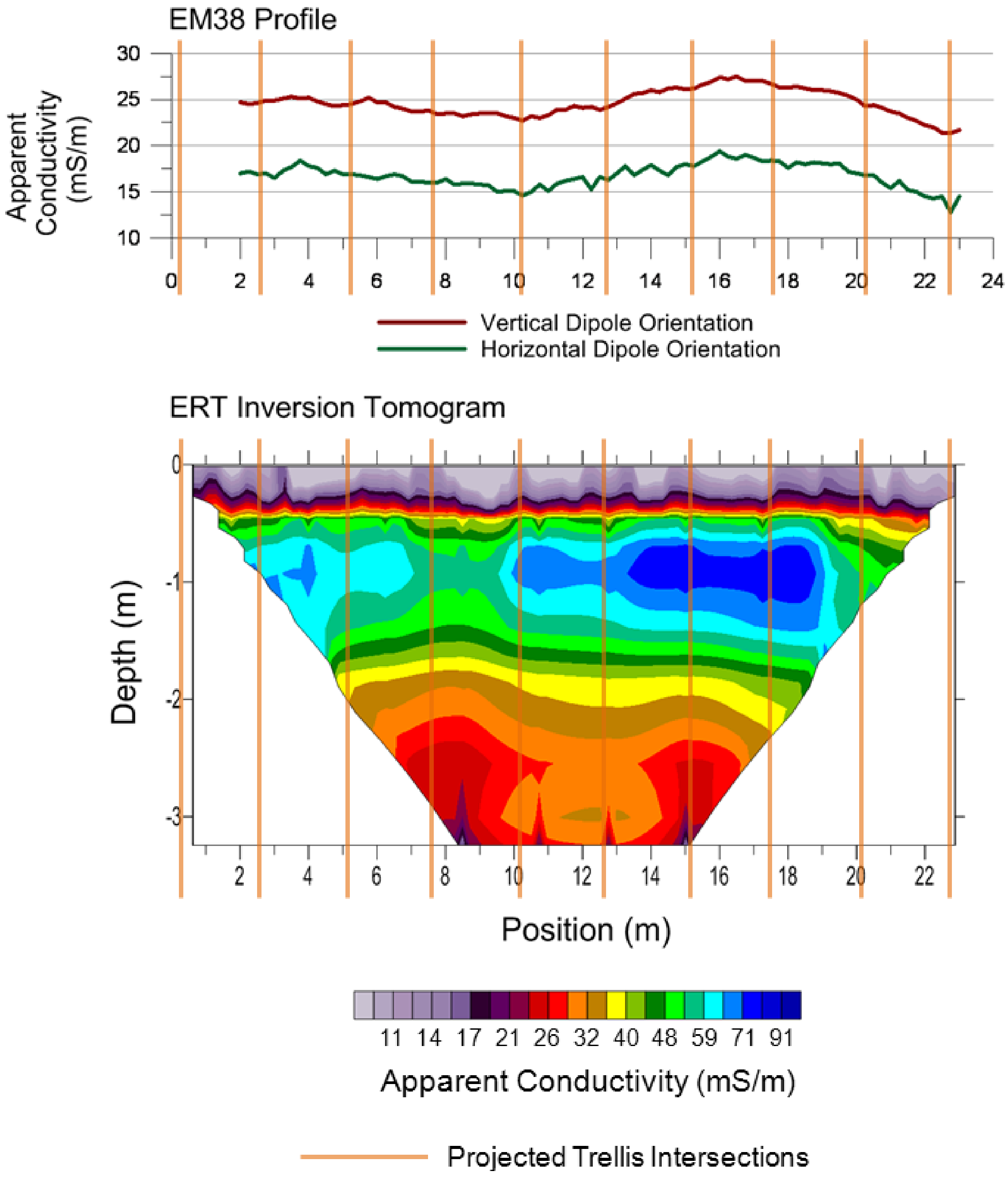

Figure 6.4 –The EM38 and the ERT inversion tomogram for Site 4 on 14 August 2012, a day with dry soil conditions and minimal lateral cyclicity observable. The locations of projected trellis intersections are shown. Drainage tiles exist at the midpoint between projected trellis intersections.

Site 5 – 03 June 2011

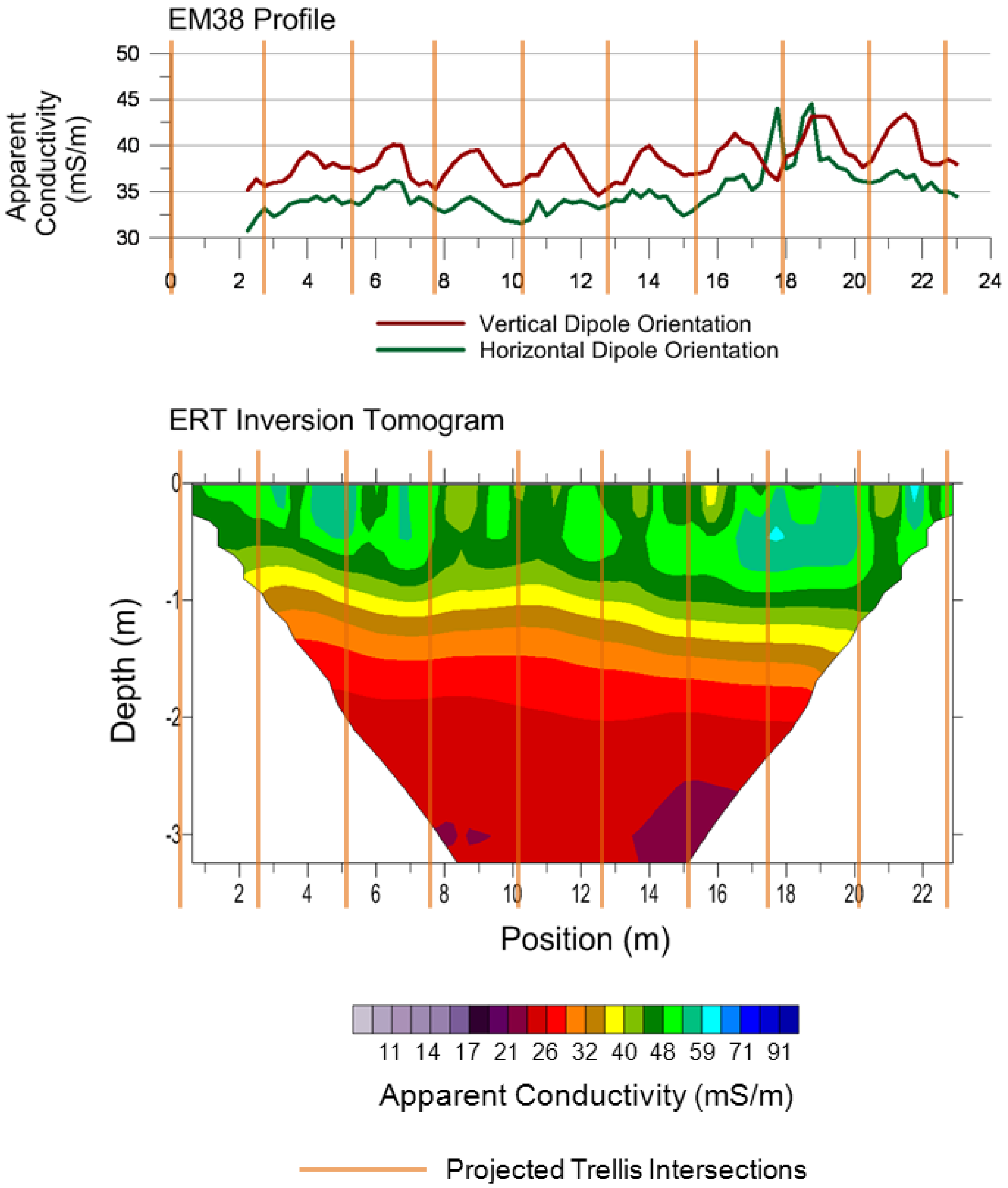

Figure 6.5 –The EM38 profile and the ERT inversion tomogram for Site 5 on 03 June 2011, a day with wet soil conditions and high lateral cyclicity observable. The locations of projected trellis intersections are shown. Drainage tiles exist at the midpoint between projected trellis intersections.

Site 5 – 14 August 2012

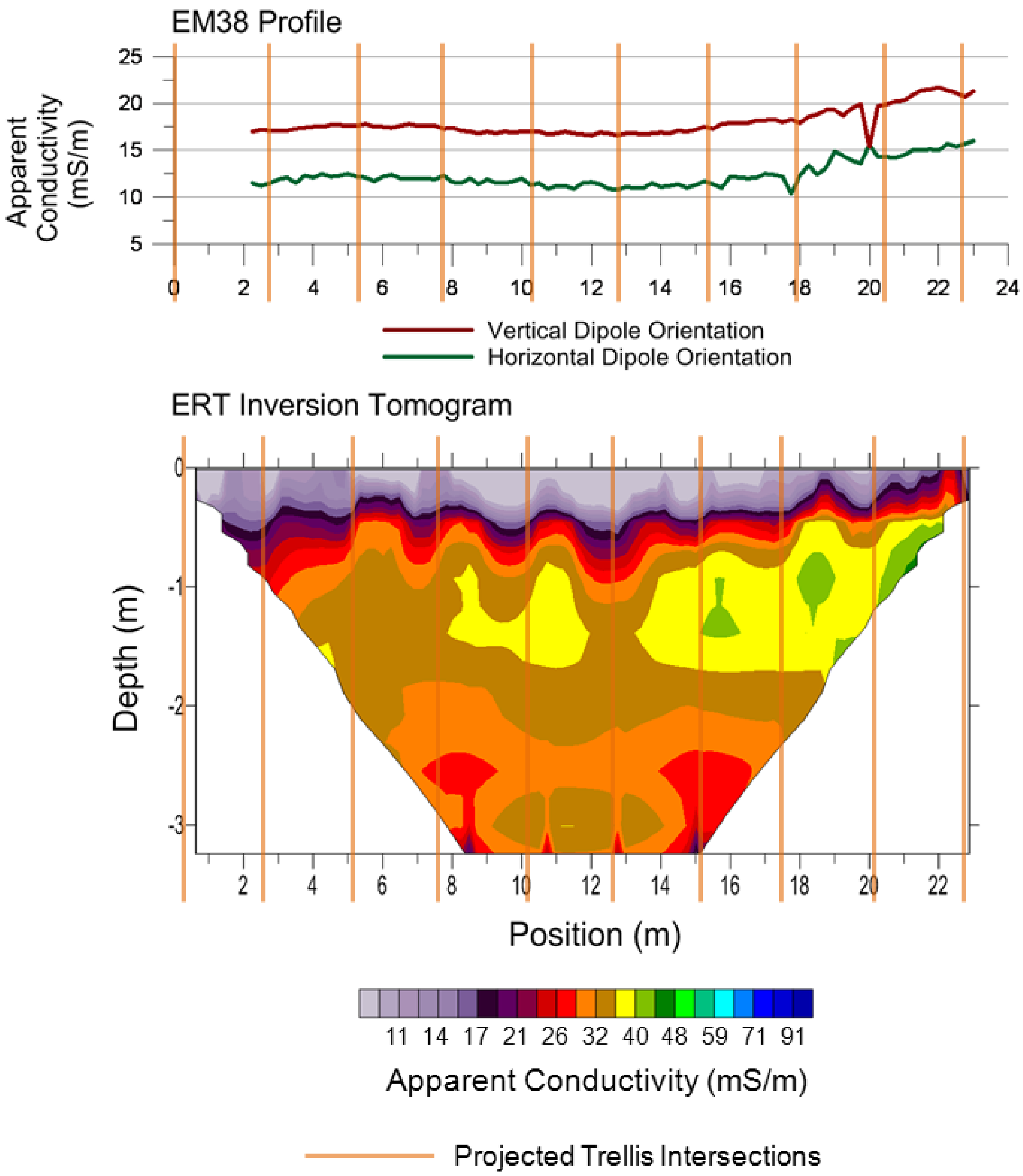

Figure 6.6 –The EM38 and the ERT inversion tomogram for Site 5 on 14 August 2012, a day with dry soil conditions and minimal lateral cyclicity observable. The locations of projected trellis intersections are shown. Drainage tiles exist at the midpoint between projected trellis intersections.

Site 3

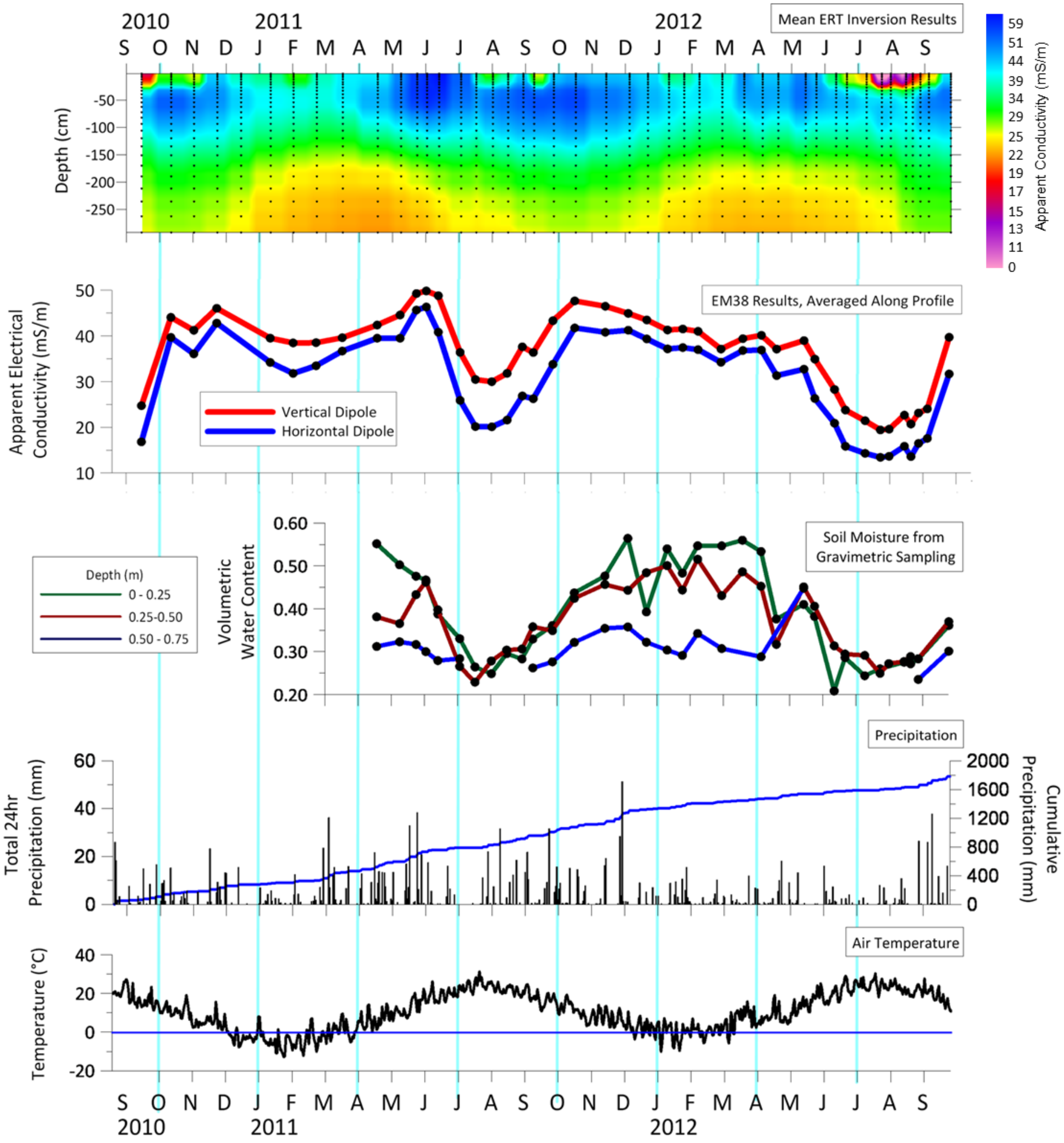

Figure 6.7 – Summarized ERT and EM38 results displayed with weather station data and gravimetric soil measurements for entire study period at Site 3.

Site 4

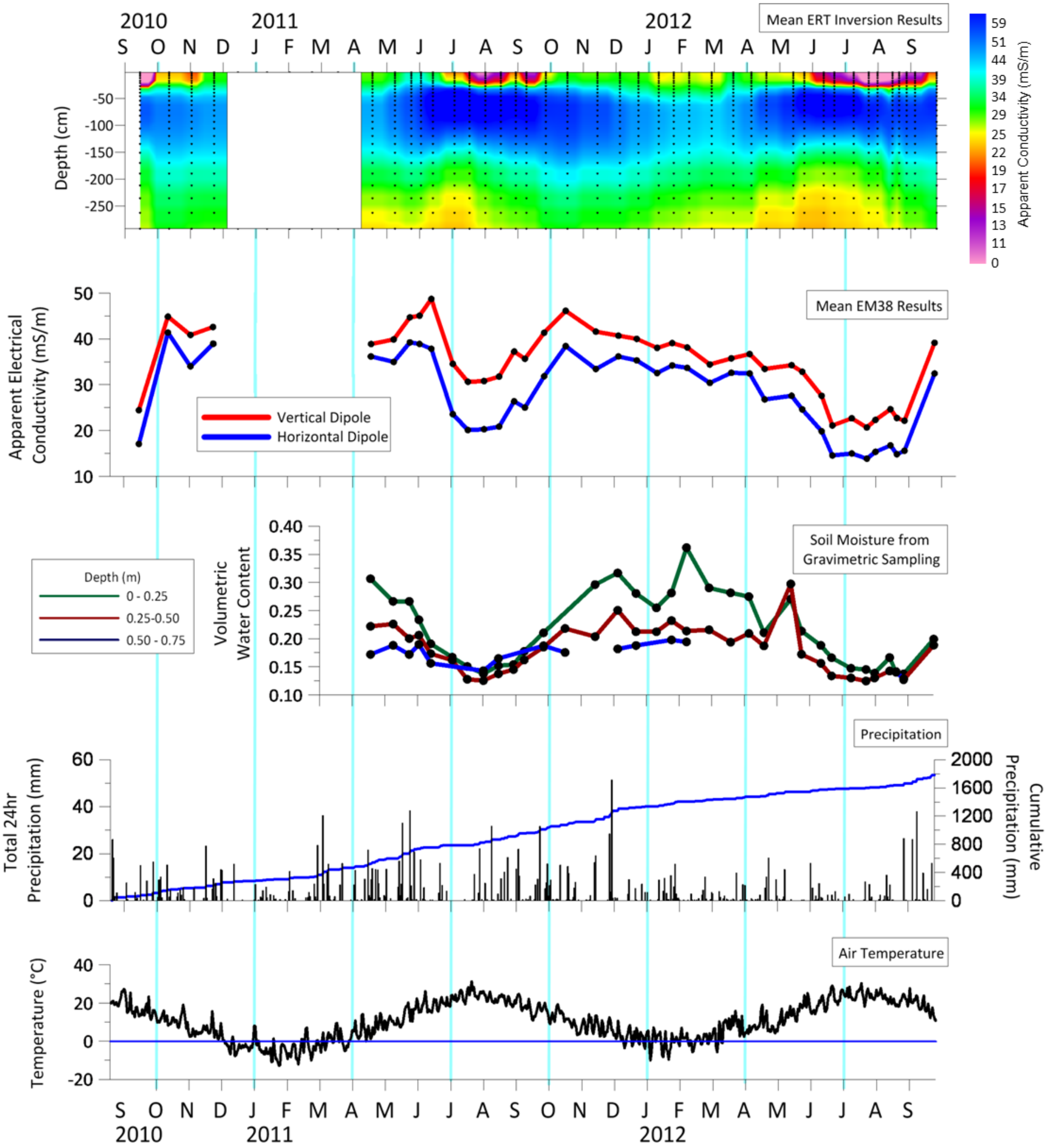

Figure 6.8 – Summarized ERT and EM38 results displayed with weather station data and gravimetric soil measurements for entire study period at Site 4.

Site 5

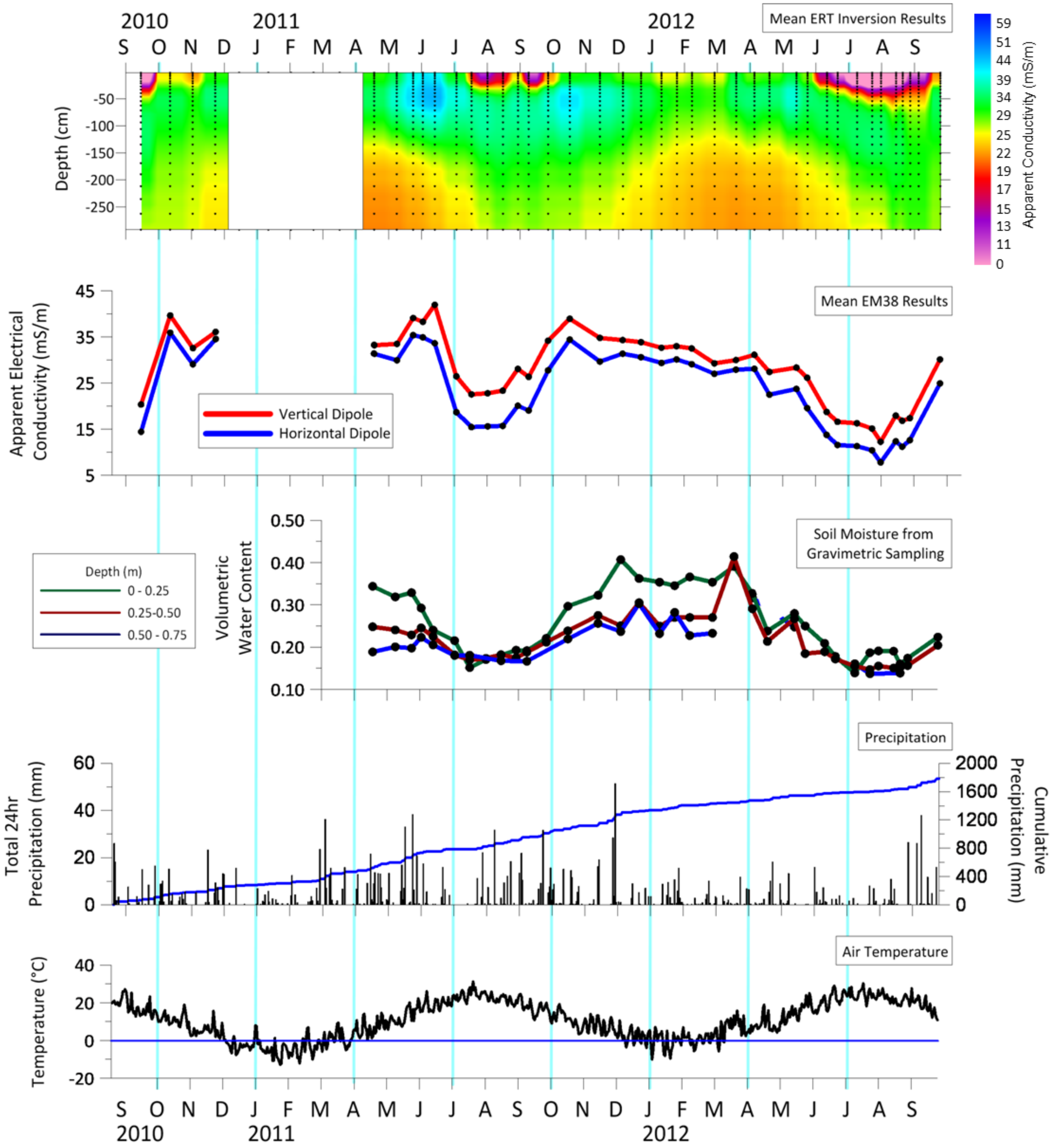

Figure 6.9 – Summarized ERT and EM38 results displayed with weather station data and gravimetric soil measurements for entire study period at Site 4.

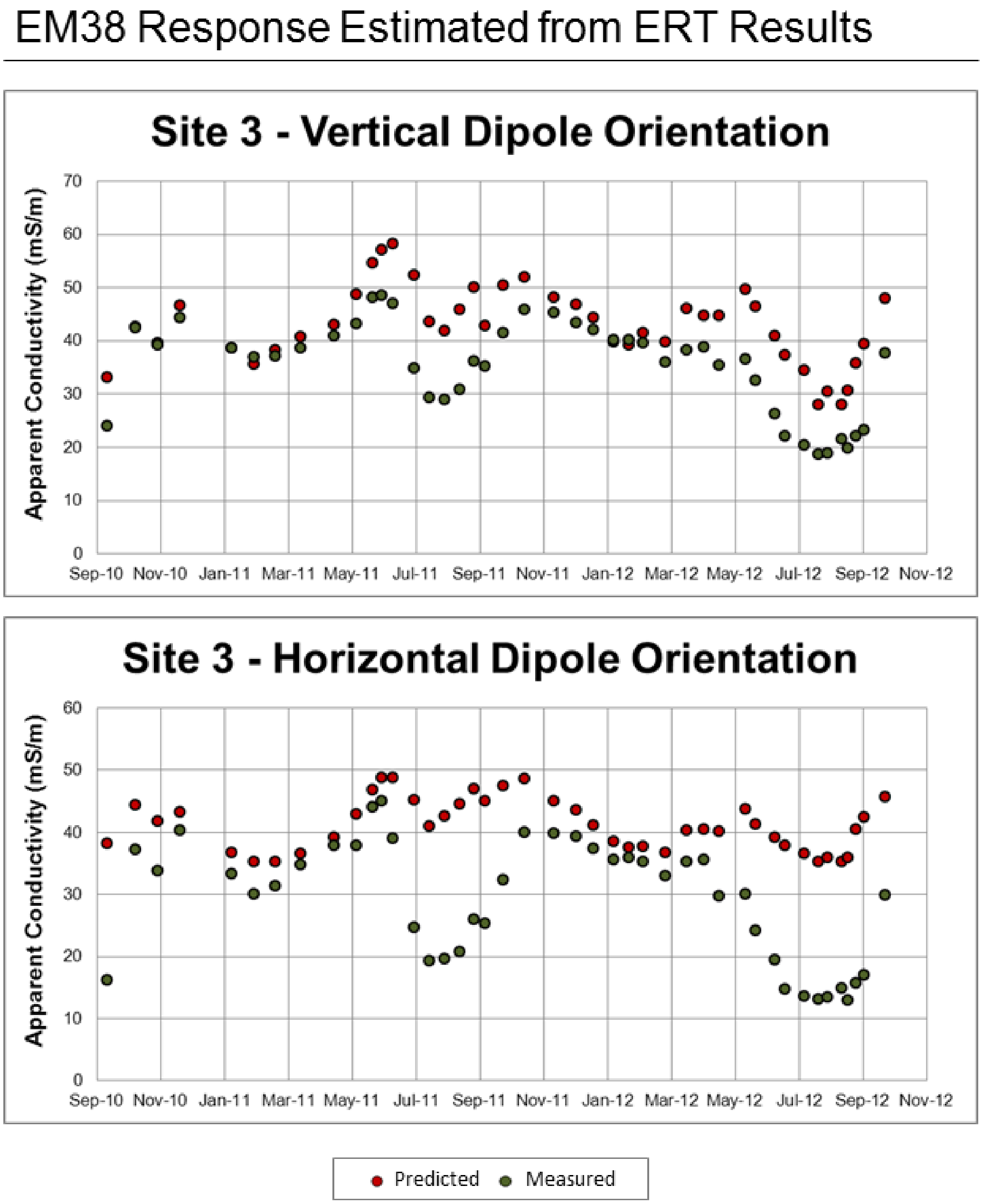

Figure 6.10 – Mean EM38 response predicted from ERT inversions (red) compared to measured EM38 response (green) for each acquisition date at Site 3.

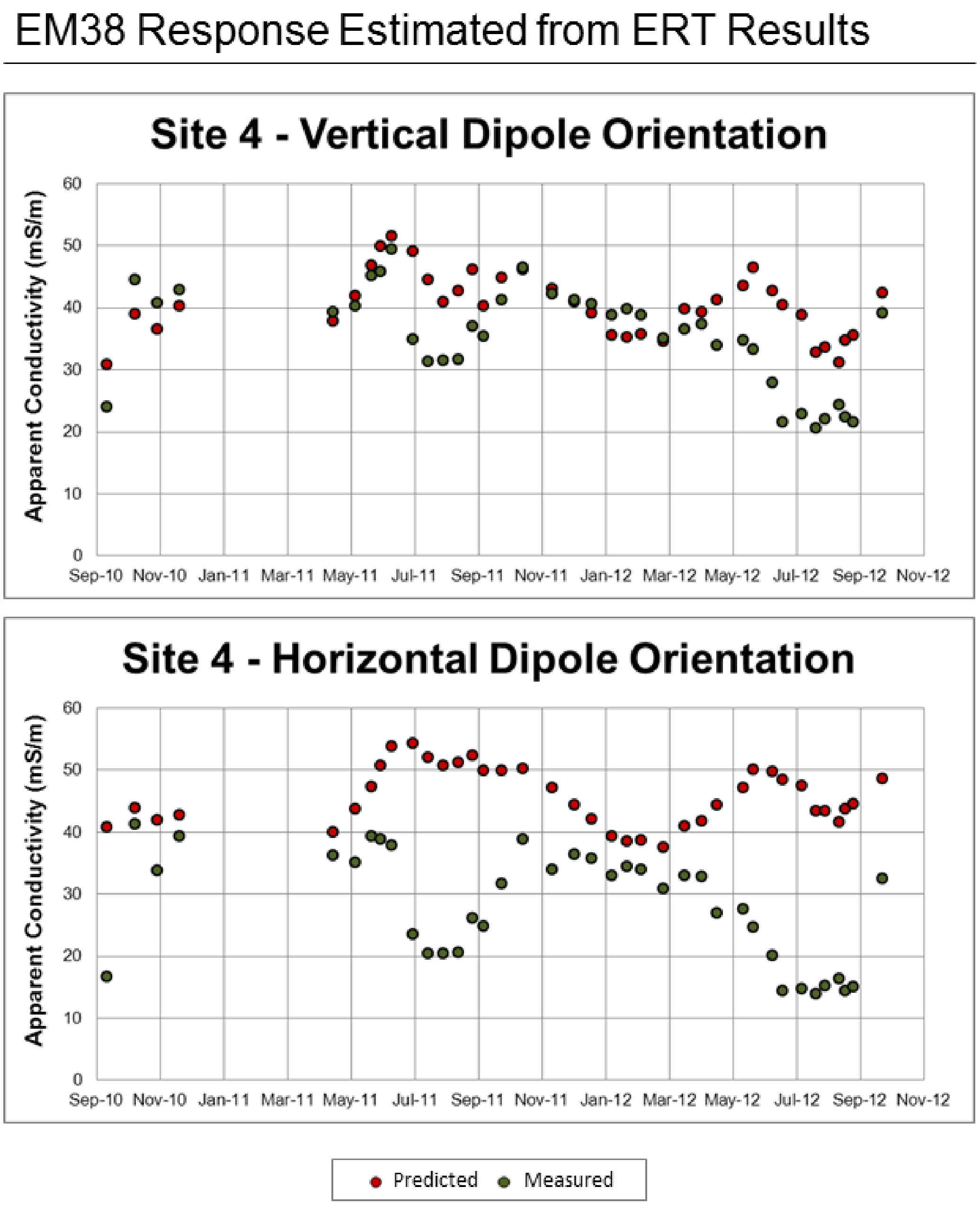

Figure 6.11 – Mean EM38 response predicted from ERT inversions (red) compared to measured EM38 response (green) for each acquisition date at Site 4.

EM38 Response Estimated from ERT Results

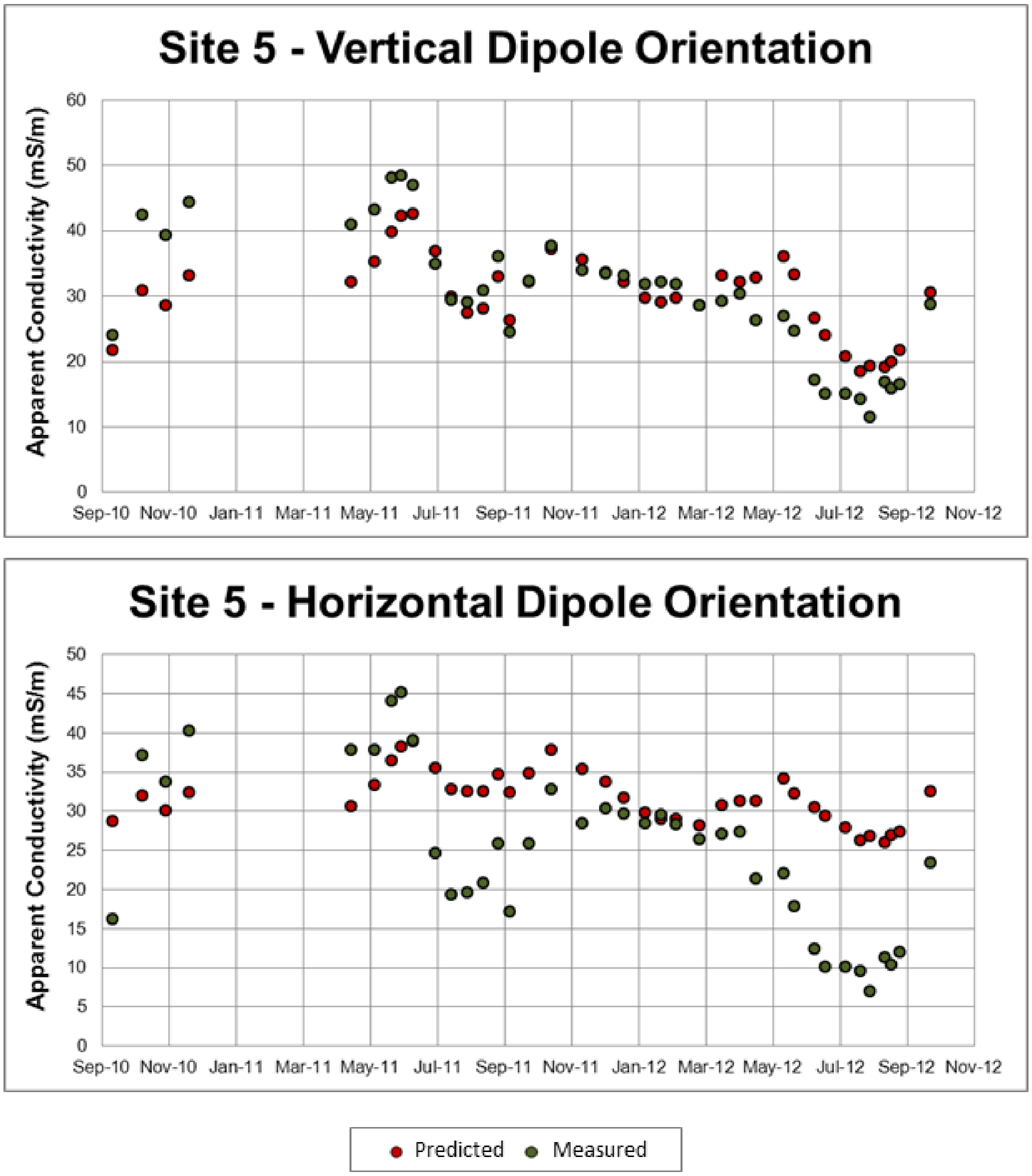

Figure 6.12 – Mean EM38 response predicted from ERT inversions (red) compared to measured EM38 response (green) for each acquisition date at Site 5.

Chapter 7 SUMMARY AND RECOMMENDATIONS

7.1 Summary

This two-year study collected time-lapse electrical geophysical observations at multiple sites within a clayey to loamy vineyard using electrical resistivity tomography and electromagnetic induction techniques. Data was acquired across a wide range of seasonal moisture conditions in 2 – 4 week intervals. Geophysical observations are coupled with soil moisture measurements and weather station data. The combination of techniques applied in this natural setting and the density of data acquired over the two-year period make this data set unique amongst those currently available in the scientific community and will provide the hydrogeophysical community with the data required for many future studies.

Analysis of the geophysical results shows subsurface electrical conductivity variations within the field site that vary spatially within each monitoring site and between monitoring sites and temporally throughout a full range of seasonal conditions. Temporal variations in electrical conductivity measurements made with both techniques are shown to be in very good qualitative agreement with the changes in soil moisture conditions inferred from gravimetric sampling and weather information. Geophysical observations are also observed to vary annually due to the variations between the conditions encountered in the yearly climate cycle. EM38 results were shown to be considerably impacted within a short time of large precipitation events.

At the three monitoring sites where both EMI and ERT measurements were performed, individual analysis of the data from each geophysical method results in similar qualitative characterizations of the subsurface structure of the monitoring sites. To measure the quantitative agreement between the two geophysical methods, predicted EM38 apparent conductivity values were calculated from inverted resistivity tomograms. A comparison of measured and predicted EM38 values reveals that the results of the two geophysical techniques deviate during certain conditions, particularly for the horizontal dipole orientation during dry summer conditions. A discussion of potential causes of this deviation included the uncertainty associated with an inversion process such as the one used in the analysis of ERT data and the differences in the response functions of the Wenner electrode array and the EMI dipoles in a horizontally-layered subsurface.

7.2 Recommendations and Future Studies

7.2.1 Investigation into the Underlying Cause(s) of the Disagreement Between EM38 and ERT Results Observed in this Study

As discussed in this study, a quantitative comparison of the EM38 and ERT results shows that a deviation occurs between the results of the two techniques during certain conditions, particularly for the horizontal dipole orientation during dry summer conditions. It is discussed that previous studies have proposed that the calibration, acquisition procedure and instrumental drift for the EM38 are likely causes for this deviation, but these are unlikely the cause for the deviation observed in this thesis as the study in this thesis has done well to limit those issues. The most probable cause suggested in this thesis is the differences in the sensitivity of the ERT and the EM38 to conductivity changes in the very shallow subsurface, as described by the response functions of the different techniques. The hydrogeophysical community will benefit from future studies that further look into this claim and test it against other potential causes for the results observed in this thesis.

7.2.2 Study of Uncertainty in ERT Inversions

Inversion processes like the one used to analyze ERT data in this thesis produce non-unique results that generate uncertainty in the geophysical interpretation. As discussed in this thesis, it is possible that the deviation between measured and predicted EM38 values arises because the ERT inversion results fit the data but are the improper model for the real world situation. Quantifying the uncertainty both spatially within an ERT tomogram and temporally throughout the ERT data set would assist in identifying this issue. A detailed study that looks into the range of subsurface conductivity structures that can be produced through the inversion of a data set would help the results of this study and be beneficial to the hydrogeophysical community.

7.2.3 Higher Resolution Precipitation Recording and the Impact of Individual Precipitation Events

A small amount of data was collected in this study to look at the effect of individual precipitation events on the geophysical response as measured by the EM38. It was shown that electrical conductivity measurements can change quickly and significantly from single precipitation events.

Precipitation data for this study was taken from a pre-existing third-party weather station which reported precipitation results as one daily value. Based on the results of the EM38 study, it is clear that finer resolution precipitation data would assist in making the best possible analysis of the relation between geophysical observations and soil moisture. It is recommended that future studies consider acquiring on-site precipitation data in 15-minute intervals and keep rigorous notes of the time of acquisition of all geophysical data, especially during days with continual precipitation or multiple precipitation events.

It would also be worthwhile to perform a study where ERT data is collected along a profile line before and after a precipitation event to compare these results with those of the EM38.

7.2.4 Next Step: Use of Data Set for Modeling Study

This thesis has generated a comprehensive set of geophysical observations that have been collected alongside soil moisture and weather station data. This complete data set is exactly what is needed to work towards resolving many topics being studied in the hydrogeophysical community.

A current area of development in hydrogeophysics is the formation of reliable inversion algorithms that decode the relationship between data collected by electrical geophysical methods and the true two-dimensional or three-dimensional electrical conductivity structure of the subsurface where the data was acquired. In terms of two-dimensional inversion, the ERT technique is well advanced (Sasaki, 1992; Loke, 2011) due to the decades-old application of two-dimensional ERT surveys in mineral exploration (Loke et al., 2013). The development of inversion algorithms for data collected with the EMI technique is less advanced and is an active research topic (Monteiro Santos et al., 2010; Triantafilis and Monteiro Santos, 2010; Mester et al., 2011; Sudduth et al., 2013). The profiles monitored in this thesis will provide an extensive real-world data set for the hydrogeophysical community to test advancements of electrical geophysical inversion in two-dimensional environments.

Pedotransfer functions that allow for the correlation between soil moisture content and bulk electrical conductivity amongst known variables such as clay content, bulk density and pH are also important developments still in progress in this field (Hinnell et al., 2010; Hadzick et al., 2011; Siddiqui and Osman, 2013). Wunderlich et al. (2013) is a recent publication that highlights that the choice of proper pedotransfer function is a topic of ongoing deliberation. In their study they offer a model that is tested in a laboratory setting with soils of varying geological parameters. As the work in the field of pedotransfer functions progresses, a comprehensive data set of field data will be valuable to test the relationships in real-world settings. The well-analyzed data set this thesis has produced can easily become the basis of future work in the area.

The next step would be to model the system as observed in this study and to use such results to provide further insight into what can be learned from the geophysical observations. Ultimately, grand questions regarding the use of geophysical techniques for quantifying moisture storage and transport in the subsurface is the goal of many in the hydrogeophysical community, and this data set provides the inputs necessary for a modeling investigation to extensively evaluate these techniques for a large data set acquired in a genuine field environment.

More specific items that could also be investigated through computer modeling with inputs from this thesis' data set include geophysical monitoring of the functioning of drainage tiles on agricultural fields, geophysical detection of the formation of desiccation cracks and the impact of freeze-thaw/winter processes on hydrogeophysical investigations.

References

Amidu, S.A. and J.A. Dunbar, 2007. Geoelectric studies of seasonal wetting and drying of a Texas vertisol. *Vadose Zone Journal* 6, 511-523.

André, F., C. van Leeuwen, S. Saussez, R. Van Durmen, P. Bogaert, D. Moghadas, L. de Rességuier, B. Delvaux, H. Vereecken, and S. Lambot, 2012. High-resolution imaging of a vineyard in south of France using ground-penetrating radar, electromagnetic induction and electrical resistivity tomography. *Journal of Applied Geophysics* 78, 113-122.

Appelo, C.A.J. and D. Postma, 2010. Geochemistry, Groundwater and Pollution. Amsterdam: A.A. Balkema Publishers. Print.

Archie, G.E., 1942. The electrical resistivity log as an aid in determining some reservoir characteristics. *Transactions of the American Institute of Mining and Metallurgical Engineers* 146, 54-61. (Must be actual archie reference and have exponent examples)

Bala, J. and A. Pieta, 2010. Validation of join inversion of direct current and electromagnetic measurements. *Acta Geophysica* 58, 114-125.

Barker, R.D., 1989. Depth of investigation of collinear symmetrical four-electrode arrays. *Geophysics* 64, 1031-1037.

Besson A., I. Cousin, H. Bourennane, B. Nicoullaud, C. Pasquier, G. Richard, A. Dorigny, and D. King, 2010. The spatial and temporal organization of soil water at the field scale as described by electrical resistivity measurements. *European Journal of Soil Science* 61, 120-132.

Binley A., and A. Kemna, 2005. DC resistivity and induced polarization methods, *in* Y. Rubin and S.S. Hubbard, eds., Hydrogeophysics, Water Science and Technology Library, no. 50, 129-156.

Binley, A., G. Cassiani, and R. Deiana, 2010. Hydrogeophysics: opportunities and challenges. *Bollettino di Geofisica Teorica ed Applicata* 51, 267-284.

Calamita, G., L. Brocca, A. Perrone, S. Piscitelli, V. Lapenna, F. Melone, and T. Moramarco, 2012. Electrical resistivity and TDR methods for soil moisture estimation in central Italy test-sites. *Journal of Hydrology* 454, 101-112.

Campbell, R.B, C.A. Bower, and L.A. Richards, 1948. Change of electrical conductivity with temperature and the relation of osmotic pressure to electrical conductivity and ion concentration for soil extracts. *Soil Science Society of America Proceedings* 13, 66-69.

Cassiani, G., V. Bruno, A. Villa, N. Fusi, and A.M. Binley, 2006. A saline trace test monitored via time-lapse surface electrical resistivity tomography. *Journal of Applied Geophysics* 59, 244-259.

Corwin, D.L. and S.M. Lesch, 2005. Apparent soil electrical conductivity measurements in agriculture. *Computers and Electronics in Agriculture* 46, 11-43.

Corwin, D.L. and R.E. Plant, 2005. Applications of apparent soil electrical conductivity in precision agriculture. *Computers and Electronics in Agriculture* 46, 1-10.

Cousin, I., A. Besson, H., Bourennane, C. Pasquier, B. Nicoullaud, D. King, G. Richard, 2009. From spatial-continuous electrical resistivity measurements to the soil hydraulic functioning at the field scale. *Comptes Rendus Geoscience* 341, 859-867.

Dadfar, H., R.J. Heck, G.W. Parkin, and K. Barfoot-Kinsie, 2011. Evaluation of a Geonics EM31-3RT probe to delineate hdrolic regimes in a tile-drained field. *Precision Agriculture* 12, 623-638.

Daily, W., A. Ramirez, D. LaBrecque, and J. Nitao, 1992. Electrical resistivity tomography of vadose water movement. *Water Resources Research* 28, 1429-1442.

Daily, W., A. Ramirez, A. Binley, and D. LaBrecque, 2005. Electrical resistance tomography – theory and practice, *in* D. K. Butler, ed., Near-Surface Geophysics: SEG, Investigations in Geophysics, no.13, 525-550.

Deiana, R., G. Cassiani, A. Kemna, A. Villa, V. Bruno, and A. Bagliani, 2007. An experiment of non-invasive characterization of the vadose zone via water injection and cross-hole time-lapse geophysical monitoring. *Near Surface Geophysics* 5, 183-194.

Edwards, B., 1989. Soils of the Regional Municipality of Niagara [map]. 1:25,000, Sheet 2 Town of Grimsby – Town of Lincoln. Ottawa: Agriculture Canada.

Environment Canada, 2014. Calculation of the 1981 – 2010 climate normals for Canada. Web, 18 July 2014. http://climate.weather.gc.ca/climate_normals/results_e.html?stnID=4703.

Fallah-Safari, M., M.K. Hafizi, and A. Ghalandarzadeh, 2013. The relationship between clay geotechnical data and clay electrical resistivity. *Bollettino di Geofisica Teorica ed Applicata* 54, 23-38.

Fitterman, D.V. and V.F. Labson, 2005. Electromagnetic induction methods for environmental problems, *in* D. K. Butler, ed., Near-Surface Geophysics: SEG, Investigations in Geophysics, no.13, 301-351.

French, H. and A. Binley, 2004. Snowmelt infiltration: monitoring temporal and spatial variability using time-lapse electrical resistivity. *Journal of Hydrology* 297, 174-186.

Frohlich, R.K. and C.D. Parke, 1989. The electrical resistivity of the vadose zone – field survey. *Ground Water* 27, 524-530.

Furman, A., T.P.A. Ferré, and A.W. Warrick, 2003. A sensitivity analysis of electrical resistivity tomograpgy arraytypes using analytical element modeling. *Vadose Zone Journal* 2, 416-423.

Geonics Ltd., 1995. EM31 – MK2 operating manual. Geonics Ltd., Mississauga, Canada.

Geonics Ltd., 2001. EM38 ground conductivity meter operating manual. Geonics Ltd., Mississauga, Canada.

Geotomo Software, 2010. RES2DINV ver. 3.59 manual: Rapid 2-D resistivity & IP inversion using the least-squares method. Web. 03 February 2013. http://www.geoelectrical.com/r2dimanu.zip.

Goyal, V.C., P.K. Gupta, S.M. Seth, and V.N. Singh, 1996. Estimation of temporal changes in soil moisture using resistivity method. *Hydrological Processes* 10, 1147-1154.

Hadzick, Z.Z., A.K. Guber, Y.A. Pachepsky, and R.L. Hill, 2011. Pedotransfer functions in soil electrical resistivity estimation. *Geoderma* 164, 195-202.

Healy, R.W., 2010. Estimating Groundwater Recharge. Cambridge: Cambridge University Press. Print.

Hinnell, A.C., T.P.A. Ferré, J.A. Vrugt, J.A. Huisman, S. Moysey, J. Rings, and M.B. Kowalsky, 2010. Improved extraction of hydrologic information from geophysical data through coupled hydrogeophysical inversion. *Water Resources Research* 46, 1-14.

Hossain, M.B., D.W. Lamb, P.V. Lockwood, and P. Frazier, 2010. EM38 for volumetric soil water content estimation in the root-zone of deep vertosol soils. *Computer and Electronics in Agriculture* 74, 100-109.

Huth, N.I. and P.L. Poulton, 2007. An electromagnetic induction method for monitoring variation in soil moisture in agroforestry systems. *Australian Journal of Soil Research*. 45, 63-72.

Jones, G., M. Zielinski, and P. Sentenac, 2012. Mapping desiccation fissures using 3-D electrical resistivity tomography. *Journal of Applied Geophysics*. 84, 39-51.

Kachanoski, R.G., E. de Jong, and I.J. van Wesenbeeck, 1990. Field Scale patterns of soil-water storage from noncontacting measurements of bulk electrical-conductivity. *Canadian Journal of Soil Science* 70, 537-542.

Kean, W.F., M.J. Waller, and H.R. Layson, 1987. Monitoring Moisture Migration in the Vadose Zone with Resistivity. *Ground Water* 25, 562-571.

Keller, G.V. and F.C. Frischknecht, 1966. Electrical Methods in Geophysical Prospecting, Toronto: Pergamon Press. Print.

Kelly, B.F.J, R.I. Acworth, and A.K. Greve, 2011. Better placement of soil moisture point measurements guided by 2D resistivity tomography for improved irrigation scheduling. *Soil Research* 49, 504-512.

Köhne, J.M., T. Wöhling, V. Pot, P. Benoit, S. Leguédois, Y. le Bissonnais, and J. Simunek, 2011. Coupled simulation of surface runoff and soil water flow using multi-objective parameter estimation. *Journal of Hydrology* 403, 141-156.

Lavoué, F., J. van der Kruk, J. Rings, F. André, D. Moghadas, J.A. Huisman, S. Lambot, L. Weihermüller, J. Vanderborght, and H. Vereecken, 2010. Electromagnetic induction calibration using apparent electrical conductivity modelling based on electrical resistivty tomography. *Near Surface Geophysics* 8, 553-561.

Loke, M.H., 1999. Time-lapse resistivity imaging inversion. *Proceedings of the 5th Meeting of the EEGS European Section*.

Loke, M.H., 2011. Tutorial: 2-D and 3-D electrical imaging surveys. Web. 04 April 2011. http://www.geoelectrical.com/coursenotes.zip.

Loke, M.H., J.E. Chambers, Rucker, D.F., Kuras, O., and P.B. Wilkinson, 2013. Recent development in the direct-current geoelectrical imaging method. *Journal of Applied Geophysics* 95, 135-156.

Lück, E., R. Gebbers, J. Ruehlmann, and U. Spangenberg, 2009. Electrical conductivity mapping for precision farming. *Near Surface Geophysics* 7, 15-25.

Ma, R., A. McBratney, B. Whelan, B. Minasny, and M. Short, 2011. Comparing temperature correction models for soil electrical conductivity measurement. *Precision Agriculture* 12, 55-66.

McNeill, J.D., 1980. Electromagnetic terrain conductivity measurement at low induction numbers. Technical Note TN-6, Geonics Ltd., Mississauga, Canada.

Mester, A., J. van der Kruk, E. Zimmermann, and H. Vereecken, 2011. Quantitative two-layer conductivity inversion of multi-configuration electromagnetic induction measurements. *Vadose Zone Journal* 10, 1-12.

Miller, C.R., P.S. Routh, T.R. Brosten, and J.P. McNamara, 2008. Application of time-lapse ERT imaging to watershed characterization. *Geophysics* 73, G7-G17.

Moffett, K.B., D.A. Robinson, and S. M. Gorelick, 2010. Relationship of salt march vegetation zonation to spatial patterns in soil moisture, salinity, and topography. *Ecosystems* 13, 1287-1302.

Mondal, P. and V.K. Tewari, 2007. Present status of precision farming: a review. *International Journal of Agricultural Research* 2, 1-10.

Monteiro Santos, F.A., J. Triantafilis, R.S. Taylor, S. Holladay, and K.E. Bruzgulis, 2010. Inversion of conductivity profiles from EM using full solution and 1-D laterally constrained algorithm. *Journal of Environmental and Engineering Geophysics*. 15, 163-174.

Newman, B.D., B.P. Wilcox, S.R. Archer, D.D. Breshears, C.N. Dahm, C.J. Duffy, N.G. McDowell, F.M. Phillips, B.R. Scanlon, and E.R. Vivoni, 2006. Ecohydrology of water-limited environments: A scientific vision. *Water Resources Research* 42, 1-15.

Ong, J.B., J.W. Lane Jr., V.A. Zlotnki, T. Halihan, and E.A. White, 2010. Combined use of frequency-domain electromagnetic and electrical resistivity surveys to delinate near-lake groundwater flow in the semi-arid Nebraska Sand Hills, USA. *Hydrogeology Journal* 18, 1539-1545.

Pellicer, X.M., M. Zarroca, and P. Gibson, 2012. Time-lapse resistivity analysis of Quaternary sediments in the Midlands of Ireland. *Journal of Applied Geophysics* 82, 45-58.

Reedy, R.C. and B.R. Scanlon, 2003. Soil water content monitoring using electromagnetic induction. *Journal of Geotechnical and Geoenvironmental Engineering*. 129, 1028-1039.

Revil, A., M. Karaoulis, T. Johnson, and A. Kemna, 2012. Review: Some low-frequency electrical methods for subsurface and monitoring in hydrogeology. *Hydrogeology Journal* 20, 617-658.

Robinson, D.A., I. Lebron, S.M. Lesch, and P. Shouse, 2004. Minimizing drift in electrical conductivity measurements in high temperature environments using the EM-38. *Soil Science Society of America Journal* 68, 339-345.

Robinson, D.A., A. Binley, N. Crook, F.D. Day-Lewis, T.P.A. Ferré, V.J.S Grauch, R. Knight, M. Knoll, V. Lakshmi, R. Miller, J. Nyquist, L. Pellerin, K. Singha, and L. Slater, 2008. Advancing process-based watershed hydrological research using near-surface geophysics: a vision for, and review of, electrical and magnetic geophysical methods. *Hydrological Processes* 22, 3604-3635.

Roy, A., and A. Apparao, 1971. Depth of Investigation in Direct Current Methods, *Geophysics* 39, 943-959.

Russell, E.J.F. and R.D. Barker, 2010. Electrical properties of clay in relation to moisture loss. *Near Surface Geophysics* 8, 173-180.

Samouëlian, A., I. Cousin, A. Tabbagh, A. Bruand, and G. Richard, 2005. Electrical resistivity survey in soil science: a review. *Soil & Tillage Research* 83, 173-193.

Sasaki, Y., 1992. Resolution of resistivity tomography inferred from numerical simulation. *Geophysical Prospecting* 40, 453-463.

Schwartz, B.F., M.E. Schreiber, and T. Yan, 2008. Quantifying field-scale soil moisture using electrical resistivity imaging. *Journal of Hydrology* 362, 234-246.

Schön, J.H., 2011. Physical Properties of Rocks. Oxford: Elsevier. Print.

Seneviratne, S.I., T. Corti, E.L. Davin, M. Hirschi, E.B. Jaeger, I. Lehner, B. Orlowsky, and A.J. Teuling, 2010. Investigating soil moisture-climate interaction in a changing climate: A review. *Earth-Science Reviews* 99, 125-161.

Sentenac, P and M. Zielinski, 2009. Clay fine fissuring monitoring using miniature geo-electrical resistivity arrays. *Environmental Earth Science* 59, 205-214.

Sheets, K.S. and J.M.H. Hendrickx, 1995. Noninvasive soil water content measurement using electromagnetic induction. *Water Resources Research* 31, 2401-2409.

Siddiqui, F.I. and S.B.A.B.S. Osman, 2013. Simple and multiple regression models for relationship between electrical resistivity and various soil properties for soil characterization. *Environmental Earth Sciences* 70, 259-267

Sudduth, K.A., D. B. Myers, N.R. Kitchen, and S.T. Drummond, 2013. Modeling soil electrical conductivity-depth relationships with data from proximal and penetrating EC_a sensors. *Geoderma* 199, 12-21.

Triantafilis, J. and F.A. Monteiro Santos, 2010. Resolving the spatial distribution of the true electrical conductivity with depth using EM38 and EM31 signal data and a laterally constrained inversion model. *Soil Research* 48, 434-446.

Van Genuchten, M.T., 1980. A closed-form equation for predicting the hydraulic conductivity of unsaturaged soils. *Soil Science Society of American Journal* 44, 892-898.

Vereecken, H., J.A. Huisman, H. Bogena, J. Vanderborght, J.A. Vrugt, and J.W. Hopmans, 2008. On the value of soil moisture measurements in vadose zone hydrology: A review. *Water Resources Research* 44, 1-21.

Wilson, R.C., R.S. Freeland, J.B. Wilkerson, and R.E. Yoder, 2003. Inferring subsurface morphology from transient soil moisture patterns using electrical conductivity. *Annual Meeting of the American Society of Agricultural Engineers* 46, 1435-1441.

Wunderlich, T., H. Petersen, S.A. al Hagrey, and W. Rabbel, 2013. Pedophysical models for resistivity and permittivity of partially water-saturated soils. *Vadose Zone Journal* 12, 1-14.

Zonge, K, J. Wynn, and S. Urquhart, 2005. Resistivity, induced polarization and complex resistivity, *in* D. K. Butler, ed., Near-Surface Geophysics: SEG, Investigations in Geophysics, no.13, 265-300.

Appendix A

Data CD

The material contained on this CD includes all field and laboratory data (original and processed) and is available from the Department of Earth and Environmental Sciences, upon request.